UNIVERSITY OF OKLAHOMA

GRADUATE COLLEGE

INTERACTIONS BETWEEN COHERENT STRUCTURES AND THE URBAN CANOPY LAYER

A DISSERTATION

SUBMITTED TO THE GRADUATE FACULTY

in partial fulfillment of the requirements for the

Degree of

DOCTOR OF PHILOSOPHY

By

SEAN CODY ARMS
Norman, Oklahoma
2014

INTERACTIONS BETWEEN COHERENT STRUCTURES AND THE URBAN CANOPY LAYER

A DISSERTATION APPROVED FOR THE SCHOOL OF METEOROLOGY

BY

Dr. Petra Klein, Chair

Dr. Phillip Chilson

Dr. Evgeni Fedorovich

Dr. Alan Shapiro

Dr. Andover Tarhule

Table of Contents

List of Tables

List of Figures

Abstract

The focus of this dissertation research is to gain further insight into the interaction of coherent structures and the urban canopy layer (CS-UCL interactions). There is a growing body of evidence that suggests that periods of strong turbulence transport across the urban canopy layer are associated with larger scale coherent structures, particularly low speed streaks or low momentum regions.

A framework for the analysis of CS-UCL interactions at full-scale is constructed through the interrogation of Direct Numerical Simulation output. A classification scheme based on a new parameter, the low momentum region index (LMR_i), is developed which can identify three types of periods of interaction in the DNS output: CS-UCL interaction, transitional, and non-interaction periods. Based on this CS-UCL interaction classification scheme, depictions of flow behavior and turbulence characteristics are created for the three interaction period types using conditional analysis. These conditional views improve upon the most advanced conceptual model of CS-UCL interactions by including the flow inside the canyon. These conditional views also offer a chance to study how CS-UCL interactions might manifest in full-scale datasets, which leads to a set of characteristic markers of the CS-UCL interaction from the point of view of a stationary observation point.

The most commonly used full-scale techniques for analyzing the impact of coherent structures, the quadrant analysis and wavelet analysis methods, are tested using simulated time series data from the DNS output. It is found that with some

modifications, these techniques can be used to detect when low momentum region driven CS-UCL interactions occur within the modeled environment. The modified techniques are then applied to a dataset collected at the Cross Center, located on the campus of the University of Oklahoma. Conditional profiles are constructed to assess whether the characteristic markers found in the DNS output manifest at full-scale. It is found that both the modified quadrant analysis and modified wavelet analysis techniques pick up on the same phenomena, demonstrating that this is the case. It is suggested that these modified techniques be used in other urban canopy layer studies to see if the same characteristic profiles and flow patterns are present.

Chapter 1

Coherent structures in the literature

According to figures from the United Nations, over half of the world population currently lives in urban areas, and the percentage is projected to increase over the next several decades (United Nations and Social Affairs 2011). The health of those living in urban areas is quite often impacted by harmful chemicals which can be very concentrated at street levels and by increased temperatures found within urban areas. Because of these impacts, it is critical to understand how heat, momentum, and various scalar constituents are transported into and out of the spaces between the structures in urban areas. Much attention has been placed on canopy scale flow structures and their role in the turbulence transport across the urban canopy layer. However, a growing body of evidence suggests that larger scale coherent structures may play a critical role in strong ventilation events, where the transport across the urban canopy layer (UCL) is greatly enhanced.

The goal of this dissertation work is to explore how these larger scale coherent structures interact with the urban canopy layer (coherent structure / urban canopy layer, or CS-UCL, interactions). In this chapter, an overview of coherent structures is presented, with focus on the larger scale coherent structures expected to be found in atmospheric boundary layer (ABL) flows. The review will begin with studies from simple turbulent flows over aerodynamically smooth boundary layers in laboratory settings, where most of the scientific details of

coherent structures have been obtained. The discussion will then focus on atmospheric flows in simplified conditions, including numerical and physical models, before examining studies of canopy flows in more complex conditions (vegetation, scaled outdoor urban models, full-scale urban campaigns, etc.). Finally, an outline of this dissertation work will be constructed based on consideration of the studies reviewed.

1.1 Coherent structures: an introduction

Coherent structures in turbulent flows have been the subject of many papers in the literature throughout the past 50 years. Although there are many ways to define a coherent structure, Robinson (1991) suggests that coherent structures be defined as

> *[A] three-dimensional region of the flow over which at least one fundamental flow variable (velocity component, density, temperature, etc.) exhibits significant correlation with itself or with another variable over a range of space and/or time that is significantly larger than the smallest local scales of the flow.*

Although the idea of structure within a seemingly random field is itself attractive (it is human nature to seek patterns after all - for example, star constellations), the main scientific reason for their study is that coherent structures appear to be associated with the efficient transport of large quantities of heat,

momentum, and scalar constitutes even through they seem to be relatively infrequent events. This study will examine how larger scale coherent structures (those that span the depth of the atmospheric surface layer) interact with the urban canopy layer (UCL), which is "the assemblage of buildings, trees, and other objects composing a town or city and the spaces between them" (Glickman and Society 2000). Research by the United Nations (United Nations and Social Affairs 2011) has shown that over 70% of the population in five of seven geographical areas currently lives in an urban area, and over half of the total world population can be found in urban settings (Fig. 1.1). More-so, the percentage of the population living in urban areas is projected to steadily grow through the year 2050. These figures further drive the need to understand CS-UCL interactions, as these interactions appear to play a role in the health of urban inhabitants by aiding in the removal of street level heat and pollutants.

Most of the knowledge regarding these larger scale coherent structures comes from the engineering literature. In these studies, ideal flows constructed in laboratory settings (specifically, aerodynamically smooth boundary flows), indicate that coherent structures induce motions which dominate the transport of fluid across the viscous sublayer interface. However, in the more complex flow scenarios found in the atmospheric boundary layer (ABL), where the boundary is not aerodynamically smooth, multiple flow structures are found which contribute to the transport of heat and momentum. While most of these structures are a result of the flow interacting directly with roughness elements along the boundary

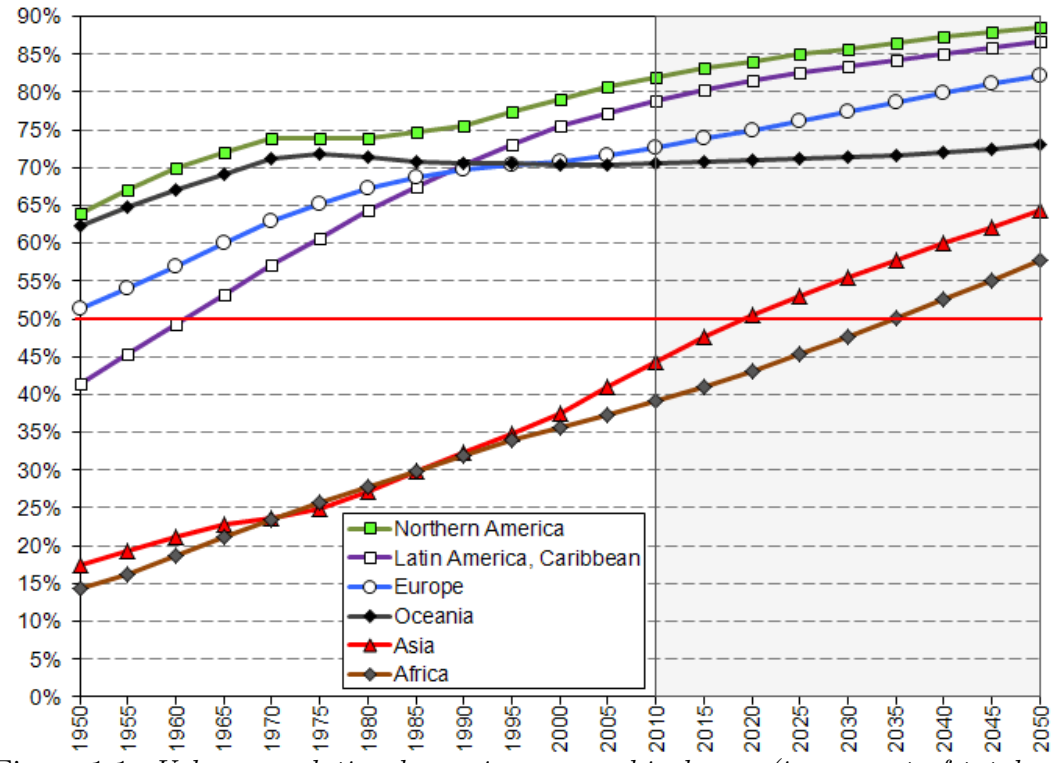

Figure 1.1: *Urban population by major geographical area (in percent of total population) from 1950, projected to 2050. (United Nations and Social Affairs 2011).*

(i.e. trees, buildings, etc.), evidence of larger scale coherent structures, similar to those found in the engineering literature, has been found.

The following sections will focus on providing an overview of the larger scale coherent structures one might expect to find in the atmospheric surface layer. Focus will first be placed on the results found in the engineering literature regarding coherent structures in simple flow settings. Next, consideration will be given to full-scale atmospheric studies that have used similar techniques to those found in the engineering literature, as well as the earliest conceptual model for full-scale atmospheric flows (one built upon results from simple flow studies). Finally, the

discussion will shift to vegetation and urban canopy studies on coherent structures, and how these studies lack in their ability to address the interactions of larger scale coherent structures with the canopy layer flows.

1.2 Coherent structures in (near-)ideal settings

Coherent structures in turbulent flows in ideal settings have been the focus of many studies over the past several decades. Often, focus is given to ejection (transfer of lower momentum away from the boundary) and sweep (transfer of higher momentum toward the boundary) events, which are intermittent and often account for a large fraction of the total momentum transfer.

1.2.1 Laboratory studies in ideal settings

It has been suggested by several authors (Adrian et al. (2000b); Natrajan et al. (2007), to name a few) that hairpin vortices are responsible for much of the heat and momentum transfer over aerodynamically smooth boundary layers using wind tunnel and water channel experimental environments. Hairpin vortices are defined to be quasi-streamwise vortices characterized by an arch giving rise to a hairpin, horseshoe, or cane shape, or slight variation of the theme (Christensen and Adrian 2001), and are qualitatively similar to the horseshoe eddy described by Theodorsen (1952). In order for the ejection event to occur, the motions in the arch of the hairpin vortex must be of sufficient strength (although precise definition of what defines "sufficient" appears to be lacking in the literature).

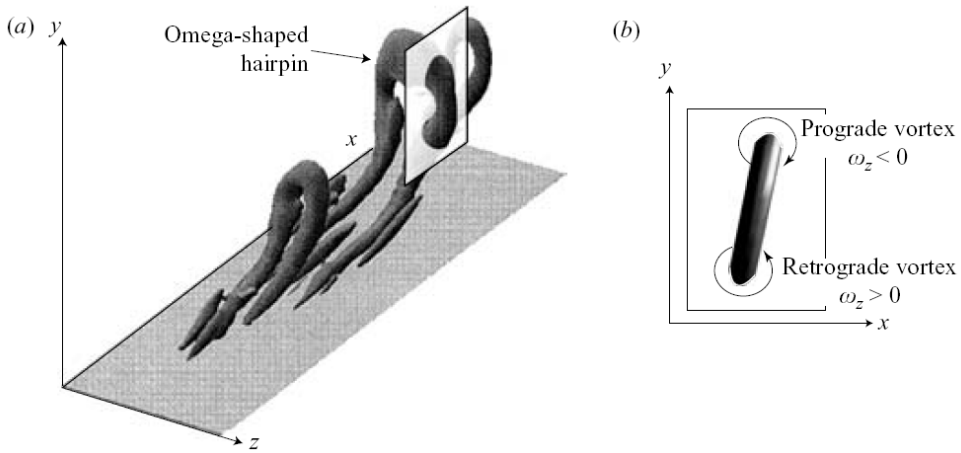

Figure 1.2: *A conceptual diagram of how a vertical slice through a hairpin vortex packet (a) could result in the observation of prograde/retrograde vortex pairs (b) in 2D PIV images. (Natrajan et al. 2007).*

Smith et al. (1991) and Zhou et al. (1999) discuss mechanisms that can cause the regeneration of hairpin vortices, which lead to the formation of several hairpin vortices in close succession. These closely spaced hairpin vortices are referred to as hairpin vortex packets. The height of the individual hairpin vortices in the vortex packet increases in the downstream direction at an angle of inclination between $15° - 20°$ (Head and Bandyopadhyay 1981). When compared to flow outside of the legs of a hairpin vortex, areas of decreased momentum are found between the legs of the hairpin vorticies that make up a vortex packet, and are referred to as low momentum regions (LMRs). While the arch of the hairpin vortex is often associated with a prograde vortex (i.e. vortex rotation in the same manner as the vorticity generated by the mean shear), retrograde vortices have been observed and are generally located in close proximity to prograde vortices. While explanations of the retrograde vortices have been offered, most are tied

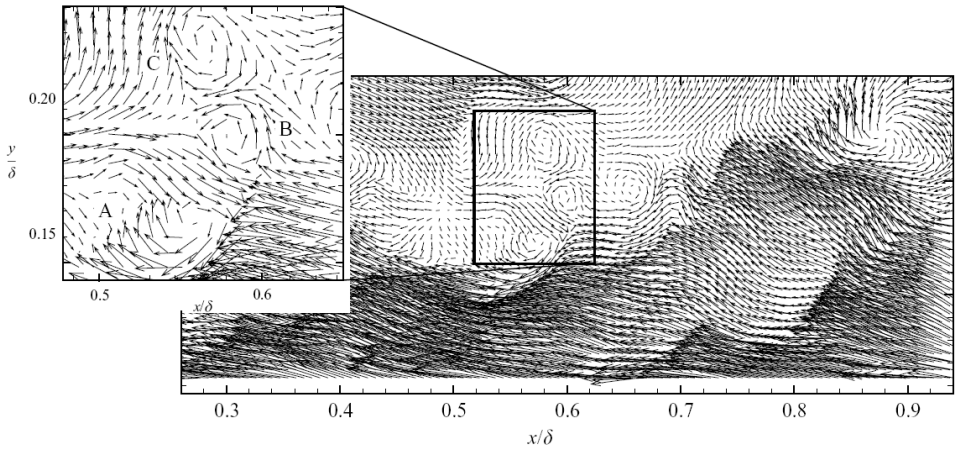

Figure 1.3: *An example of a retrograde vortex (denoted as B in the insert) surrounded by two prograde vortices (A and C) in an instantaneous PIV snapshot.(Natrajan et al. 2007).*

to the omega-shape of the hairpin vortices. Smith et al. (1991) suggests that the legs of individual hairpin vortices can pinch off and reconnect to form ring shaped structures; this is also suggested by Bake et al. (2002). However, a more likely explanation was suggested by Wu and Christensen (2006) and relies on the fact that most studies had utilized 2D particle image velocimetry (PIV) data. Wu and Christensen (2006) suggest that the hairpin vortices have an omega-like shape towards the arch, and a 2D slice in the along-stream direction may result in a prograde/retrograde vortex pair (Fig. 1.2). Using statistical arguments, Wu and Christensen (2006) suggest that it should not be surprising that these prograde/retrograde vortex pairs commonly appear in 2D PIV datasets. Evidence supporting this explanation of the prograde/retrograde vortex pair is given in Natrajan et al. (2007), although some situations, such as a retrograde vortex surrounded by two prograde vortices (Fig. 1.3), can be best explained

by ring-like structures using the hairpin leg pinch-off / rejoin mechanism. Prograde/retrograde vortex pairs have been identified in 3D fields using a holographic PIV technique applied to channel flow in a water tank study (Sheng et al. 2008).

Illuminating the motions associated with coherent structures can be quite tricky, even under simple conditions. Adrian et al. (2000a) compare the ability of the Reynolds (time and space) and Galilean decompositions, as well as homogeneous (i.e. top-hat spatial filter) and inhomogeneous (i.e. Proper Orthogonal Decomposition (POD)) filtering techniques to identify vortices in instantaneous turbulent pipe flow velocity fields as recorded by the use of PIV. It was found that the POD based filter was best for visualizing all of the small scale vortices present in the flow. Principal Component Analysis (PCA), essentially identical (but older) than POD, was employed in an Large Eddy Simulation (LES) study by Rinker and Young (1996) to investigate coherent structures in the convective boundary layer. Rinker and Young (1996) showed the ability of PCA to extract flow patterns induced by gravity waves, as well as inflow and outflow patterns associated with convective plumes. However, these studies have also focused on identification of coherent structures using high (spatial) resolution temporal snapshot data (2D slices from PIV data or 3D volumes from LES), which is very difficult to obtain in full-scale atmospheric studies.

1.2.2 Full-scale studies in near-ideal settings

Full-scale studies of coherent structures in the atmosphere have been conducted over boundaries with simple conditions (homogeneous surfaces with low roughness) using techniques similar to those used in laboratory studies, such as those mentioned in the previous section. Weijers et al. (1995) investigated large scale coherent structures (thermals) in the convective ABL using PCA. Using data from five sonic anemometers in a horizontal grid, simple flow patterns were discerned (convergence/divergence patterns, thermal plume signatures), and it was concluded that PCA can be a useful tool in the examination of the kinematics of observed flows. Studies concerning coherent motions over the ocean were conducted by Mason et al. (2002), who constructed so called plume datasets by filtering the raw datasets using the dominant modes of variation, as determined by PCA, which were highly coherent in phase. The study by Mason et al. (2002) is different to previous studies as they use 110 minute time series data in the PCA, not temporal snapshots as in previous studies. However, the results of Mason et al. (2002) indicate that PCA appears to have picked up on the signal of large scale convective thermals in the ABL and not the smaller scale coherent structures, such as hairpin vortices. These results suggest that attempts to apply the techniques used in ideal laboratory studies are hindered by the very large scale coherent structures encountered in the ABL (e.g. thermal plumes that span the depth of the ABL).

Focusing on the results of previous literature in fluid mechanics, McNaughton (2004) tried to conceptually relate the "horseshoe eddy" of Theodorsen (1952)

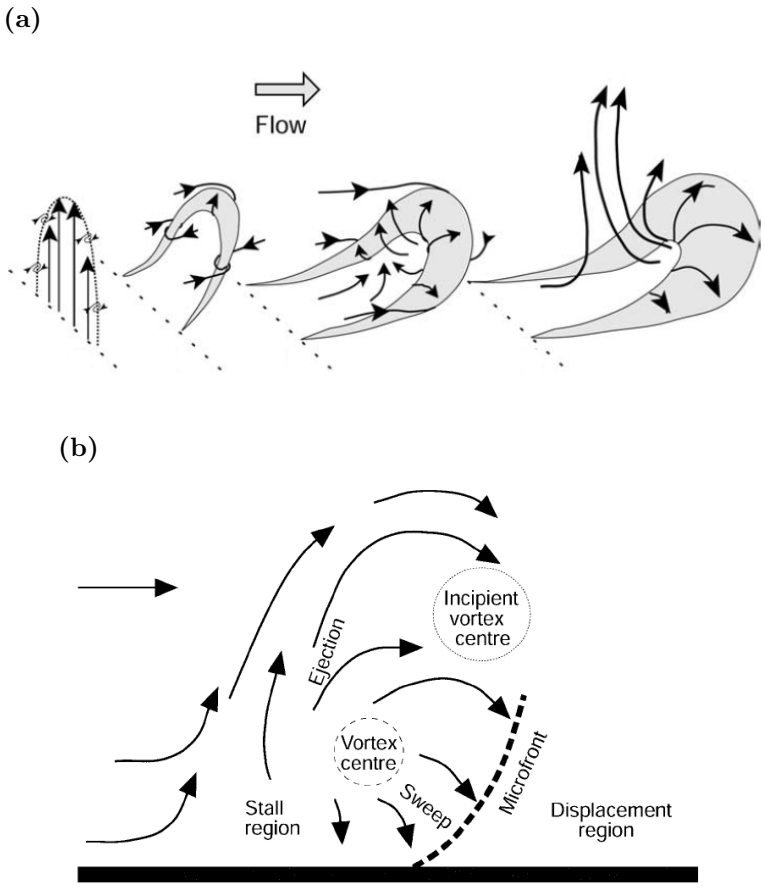

Figure 1.4: *The hypothesized evolution of TEA structures (McNaughton and Blundell 2002) (a), and a detailed conceptual model of a TEA-like (TEAL) structure (b) (McNaughton 2004).*

to coherent structures in the Atmospheric Surface Layer. The horseshoe eddy has been linked to the Theodorsen ejection amplifier (TEA) by McNaughton and Blundell (2002) (Fig. 1.4a). A TEA structure is initiated by an ejection near the wall of a laminar boundary layer flow. The oncoming fluid if then forced to lift, by the ejection, and curl over and around the ejection, to initiate a vortical structure in the shape of a hairpin (McNaughton and Blundell 2002). Although one does not expect to find exact TEA structures in the atmosphere due to surface complexities and non-laminar flow, McNaughton (2004) proposed the idea of TEA-L (TEA-Like) structures and used qualitative features found in previous results from the literature to support arguments on their existence. Although visually similar, the idealized TEA-L model (Fig. 1.4b) provides additions to the hairpin vortex model to account for observed patterns of ejections and sweeps, and their relation to microfronts (a concept found in vegetation canopy studies - for example, see Mahrt and Gibson (1992)). Studies testing the properties of the TEA-L model have not been found in the course of this literature review, likely due to the lack of quantitatively testable details in the conceptual model.

1.3 Full-scale canopy flows

Documented flow studies in vegetative canopies occurred long before those in urban areas. According to a review on turbulence over cities, Roth (2000) cites Shiotani and Yamamoto (1950) as the first reported study of turbulence over a city (in this case, Tokyo). However, the first study of flows in vegetative canopies

was Allee (1926), where horizontal velocity observations were recorded throughout the canopy layer in a tropical rain forest. The reason this is mentioned is that, historically, there has been a temptation to compare flows in vegetative canopies to flows in urban canopies, as flows in vegetative canopies have been studied for a greater length of time. Given that many urban areas can be considered forests by definition - $\geq$ 10% of the land is stocked with trees (Rowntree 1984) - the temptation for comparison should be even less surprising (Oke 1989).

A brief comparison reveals that although somewhat similar at first glance, the differences between the urban and vegetative canopies are striking. Buildings are essentially impermeable and inflexible; vegetation is permeable and flexible, but still has the ability to generate mechanical turbulence. Buildings are mostly opaque (with the exception of windows), have a considerable range of albedo values, large thermal mass (when compared to vegetation), and activities inside the building result in the need to understand many different aspects of internal radiative transfer; vegetation is not opaque, has a relatively narrow range of albedo values, a quite smaller thermal mass (when compared to buildings), and has an internal water supply that can mitigate heat transfer (Oke 1989).

Even with these differences, the studies reviewed by Roth (2000) indicate that integral statistics and spectra from urban areas show large similarity with those from vegetative canopy studies, and it is suggested that the theoretical analysis framework developed in vegetative canopy studies could be applied to urban areas (after being tweaked to include the effects of wake turbulence). Thus, it is generally accepted that the techniques used to study turbulence in urban and

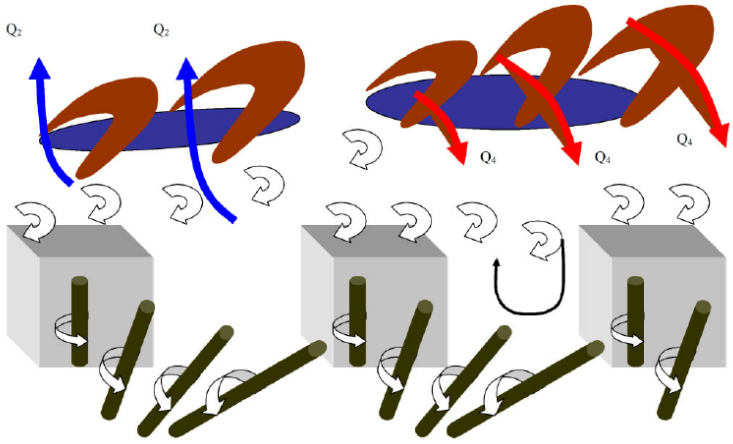

Figure 1.5: *Conceptual model of several types of vortices found in the urban environment. The brown, arch shaped regions depict the hairpin vortices, the blue regions depict the lower momentum core associated with the hairpin vortex packet, and the olive/dark gray columns represent shedding of eddies from the edge of the buildings. The U shaped dark arrow in the right canyon depicts a street canyon vortex, possibly driven by CS-UCL interactions. (Coceal et al. 2007a).*

vegetative canopies are similar and so are the approaches used to study coherent structures.

Much like studies of coherent structures over vegetative canopies, observational studies are ubiquitous in urban areas. There exists a large number of numerical (Large Eddy Simulation (LES) and DNS) and physical modeling (water tank and wind tunnel) studies focused on urban areas, and that number is actively growing.

Physical modeling has revealed several examples of coherent structures in turbulent flows over modeled urban areas. The most widely acknowledged coherent structures within urban areas occur at the street canyon level, and are known

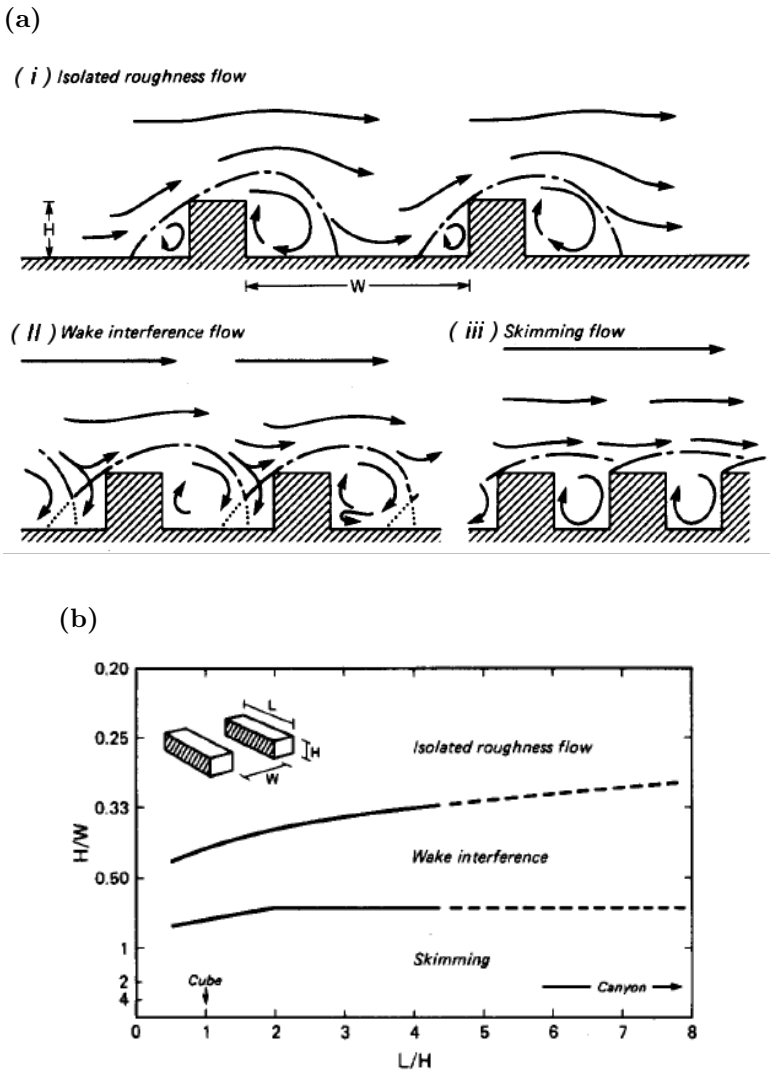

Figure 1.6: *Flow regimes in ideal street canyons as proposed by Oke (1988) for 2D (a) and 3D (b) street canyons. Isolated flow is represented in a(i), wake interference flow in a(ii), and skimming flow in a(iii)*

as street canyon vortices or recirculation vortices. The canyon aspect ratio, the ratio of building height to canyon width (H/W), is often used to predict the characteristics of the street canyon vortex (Fig. 1.6) (Oke 1988; Eliasson et al. 2006; Li et al. 2008). Three types of flow are traditionally discussed - isolated flow, wake interference flow, and skimming flow. In isolated flow, the buildings are sufficiently separated such that their wake vortices do not interact. In skimming flow, the buildings are close enough that the bulk of the flow above the buildings does not interact with flow in the street canyon. The wake interference regime, an intermediate between the isolate flow and skimming flow regimes, is characterized by the interaction of the buildings with the wake vortices generated upstream (Oke 1988). Although the framework introduced by Oke (1988) is simple, it does not appear to do a good job in complex building arrangements (Johnson and Hunter 1999) and it has been shown that other factors, even small details such as the type of roof on the buildings of the canyon (i.e. pitched roofs vs flat roofs), can alter the properties of the resulting flow regimes (Kastner-Klein and Plate 1999). These small details have even been shown to prevent the formation of street canyon vortices all-together (Kastner-Klein et al. 2004). It should also be noted that physical modeling suggests flows within a street canyon appear to be controlled by local geometries and not larger scale changes in surface roughness (Barlow et al. 2004), although the sensitivity of the street canyon flow to local geometry may be less of an issue when the approach flow is in equilibrium with urban surface (Barlow and Belcher 2004).

The three dimensional of the flow also is important to consider when discussing coherent structures in urban areas. As shown in Fig. 1.7, there is a zone directly behind the building known as the cavity zone. Within the cavity, lateral edge vorticies form and shed, interacting with the flow downstream of the building. Fig. 1.7 indicates that the upstream flow consists of a two dimensional log profile. The shear associated with the wind profile generates cross-stream vorticity. This cross-stream vorticity then interacts with the building, where the upstream environmental vortex lines are bent around the building, creating a horseshoe vortex. The horseshoe vortex can then interact with the flow downstream of the building, potentially creating helical motion in the street canyon of a series of buildings. Helical motion has been observed in such situations, and is well documented both historically and in observations by Eliasson et al. (2006).

While these canopy scale coherent structures are perhaps most recognizable, the larger scale hairpin structures may still play a role in the transport of heat and momentum in urban areas and have most recently observed by dual doppler lidar (Newsom et al. 2008)); these structures are even included in a recent conceptual model of flow over urban areas, constructed from Direct Numerical Simulation (DNS) output simulated over a series of regular cubes (Fig. 1.5 (Coceal et al. 2007a)). Coceal et al. (2007a) suggest that the shear layer at the top of the UCL acts as a lid. In the presence of the low momentum region associated with a hairpin vortex packet, Coceal et al. (2007a) suggests the shear layer can lift, allowing for strong canyon ventilation. It is suggested that sweep motions generated by the hairpin vortices near the edge of the low momentum region

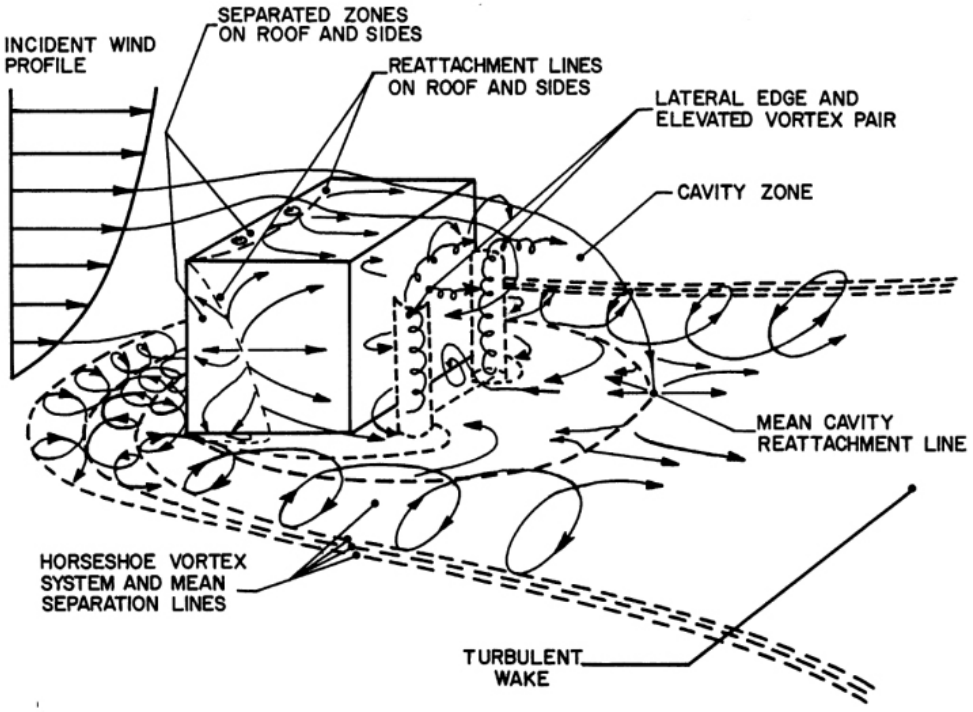

Figure 1.7: *Three dimensional structures associated with flow around a building with sharp edges. Note the horseshoe vortex, which is generated by the upstream environmental cross-stream vorticity, bending around the edges of the building. Image from Arya (2001)*

can suppress the shear layer and lead to the formation of a street canyon scale recirculation. It should be noted that while Coceal et al. (2007a) stress that their conceptual model is incomplete (especially in clearly showing how CS-UCL interaction occur across the entire depth of the modeled UBL), it is perhaps the most complete view of how large scale coherent structures may interact with the canopy shear layer. Results from a wind tunnel study by Savory and Abdelqari (2000) indicate that the shear layer does not lift/close like a lid, as suggested by the conceptual model of Coceal et al. (2007a), but rather changes thickness during the interaction of the shear layer with larger scale vortex structures. It is then proposed that the thickening of the shear layer controls whether or not the shear layer penetrates into the canyon, resulting in a ventilation event. Regardless of the control mechanism, the conceptual models of Savory and Abdelqari (2000) and Coceal et al. (2007a) agree with the observations of Louka et al. (2000), which indicate that the shear layer (and modifications of) is critical in controlling street canyon circulations.

One issue of applying results from DNS and physical modeling studies to full scale flows is that these studies, especially DNS based studies, are often performed on flows with lower Reynolds numbers that those found at full scale. The Reynolds number,

$$Re = \frac{vL}{\nu}, \tag{1.1}$$

is a measure of the strength of inertial forces compared to viscus forces, where v and L are the characteristic velocity and length scales for the flow, respectively,

and ν is the kinematic viscosity. The kinematic viscosity for air is approximately $1.5 \times 10^{-5}\ m^2 s^{-1}$ (Stull 1988). For typical surface layer flows, $L \approx 100\ m$ and $v \approx 10\ ms^{-1}$, which results in a Reynolds number of approximately 1×10^8. In order for flows to be dynamically similar, they need to have equivalence in their Reynolds numbers (Kundu and Cohen 2004). While the Reynolds number of the flows used in the studies of Coceal et al. (2007a) and Savory and Abdelqari (2000) are much lower ($Re \approx 5 \times 10^3$ and $Re \approx 1 \times 10^4$, respectively), they are both above the critical Reynolds number of $\approx 2 \times 10^3$ (Stull 1988), which places them in the turbulent flow regime. Also, the DNS output from Coceal et al. (2007a) has been favorably vetted (Coceal et al. 2006) against turbulence statistics collected from a wind tunnel study Castro et al. (2006) with the same surface roughness element layout but with a Reynolds number of $\approx 1 \times 10^4$. This suggests that some of the turbulence related feature of the flow remain as Re is increased. Additionally, Coceal et al. (2007b) performed a sensitivity study using various values of Re and found that the number of hairpin vortices increased with increasing Re, but the presence of the hairpin induced low momentum region remained intact at all Re tested (Coceal et al. 2007b).

Observational studies have also provided evidence for street canyon vortices. Eliasson et al. (2006) addressed questions regarding street canyon vortices through the use of an array (five vertical levels, three horizontal cross-canyon) of instrumentation within a street canyon. They conclude that for the particular street canyon studied, a street canyon vortex formed consistently for approach flows +/- 60° perpendicular to the major canyon axis. Also observed by Eliasson

et al. (2006) was a secondary recirculation vortex located in the lower portions of the canyon.

However, the study by Eliasson et al. (2006) highlights the inherent limitations of observational studies - given the complex setup of the observational platform utilized in their work (which was necessary to sample variables in a cross section perpendicular to the major canyon axis), only one cross-canyon cross section could be studied. In order to overcome these limitations, one popular approach has been to perform physical model/full-scale hybrid studies. An example of this type of hybrid study can be found in Idczak et al. (2007). In this study, a 1:5 scale model in flat, homogeneous terrain with little vegetation, was used to study the microclimate conditions in a street canyon. Like the study by Eliasson et al. (2006), Idczak et al. (2007) found a somewhat persistent street canyon vortex; however, unlike the previous study, a secondary recirculation was not found. In addition to investigating street canyon vortices, the issue of the impact of radiational heating was addressed by Idczak et al. (2007). Idczak et al. (2007) state that while previous numerical studies indicate radiational heating from the sun is important on the development of street canyon vortices, wind tunnel studies show that it's effect may be marginal, and observational studies indicate that radiational heating has no effect at all. However, in their study, Idczak et al. (2007) report that thermal effects are only significant near the wall, and have negligible effect on the overall structure of the street canyon flow pattern. A more recent study by Takimoto et al. (2011) utilized Particle Image Velocimetry (PIV) measurements to study turbulent flows in an outdoor scaled urban model

as part of the Comprehensive Outdoor Scale MOdel (COSMO) study (Kanda et al. 2006). Takimoto et al. (2011) observed strong, large scale upward motions between the scaled building, both in the outdoor model and in the complimentary wind tunnel study. It was noted in the wind tunnel study that these strong upward motions were correlated with the presence of a low-speed structure over the building array. This finding is in agreement with the larger scale ejection motions associated with the low momentum regions of hairpin vortex packets in the conceptual model of Coceal et al. (2007a). The study by Takimoto et al. (2011) perhaps provides the closest link between larger scale coherent structures impacting the transport of fluid from between buildings in atmospheric boundary layer flows to date.

Given the complexity of urban landscapes, the most effective way to study the urban boundary layer (UBL) at full-scale is through large scale campaigns. Examples of these large scale campaigns are the Vertical Transport and MiXing (VTMX) campaign (Doran et al. 2002) and the concurrent campaign "URBAN 2000" (Allwine et al. 2002), which focused on dispersion in urban areas. More recent campaigns included the general development of the UBL among their many goals. Most notable are the Joint Urban 2003 (Allwine et al. 2004), Urban Boundary Layer ESCOMPTE (a French acronym which roughly translates to a field experiment to constrain the models of pollution emission transport) (Mestayer et al. 2005), and the Basel UrBan Boundary Layer Experiment (BUBBLE) (Rotach et al. 2005). All three experiments have resulted in studies focused on coherent structures in the urban area (Nelson et al. 2007; Salmond et al. 2005;

Christen et al. 2007). The ESCOMPTE (Salmond et al. 2005) and BUBBLE (Christen et al. 2007) studies were focused on the UCL and used wavelets to detect the ramp structure of the microfronts with the UCL; the quadrant hole method has been used on data from Joint Urban 2003 (Nelson et al. 2007). Nelson et al. (2007) found evidence of a wall jet, formed by the downdraft of the impinging wake vortex on a downstream buildings surface. Further results from Nelson et al. (2007) suggest the possibility of a new sublayer near the bottom of the canyon. This hypothesized sublayer appears to be marked by disorganized flow. Salmond et al. (2005) worked with data from the nocturnal UBL in an attempt to study the ventilation of heat and CO_2. It was found that the wavelet detection technique was able to identify coherent structures in the nocturnal UBL. Evidence from the detected events showed that convective plumes continue to be present throughout the night, and it was speculated that this was due to the delayed release of heat stored in street canyon. Christen et al. (2007) greatly added to the knowledge of coherent structures in the UBL. Using observation from near canyon floor to 2.2 times the height of the street canyon, Christen et al. (2007) found that the level at which transport of momentum and heat change from being dominated by sweep events to ejection events is different, thus implying a dissimilarity in the exchange of those quantities within the UCL. Also, Christen et al. (2007) speculate that coherent structures from above the street canyon (i.e. hairpin vortices as suggested by Coceal et al. (2007a), or K-H instabilities) may penetrate the street canyon and be detected by the wavelet analysis. While these

studies all suggest the importance of larger scale coherent structures in the exchange of heat, momentum, and other scalar consultants, none of them actually make a direct link to these larger scale structures in their observations, therefore leaving a gap in knowledge on how the larger scale structures interact with the UCL.

1.4 Proposed study

The focus of this dissertation research is to gain further insight into CS-UCL interactions. As presented in this chapter, there is a growing body of evidence that suggests larger scale coherent structures, particularly low speed streaks or low momentum regions, are associated with periods of strong turbulence transport across the UCL. Unfortunately, strong evidence for these interactions has been lacking in full-scale observational studies; it is suggested that this is perhaps a reflection of the fact that traditional methods of analysis found in the engineering literature for simplified flows (like PCA or POD) are not readily applicable to full-scale studies. To further compound the issues at hand, the techniques used to study these ventilation events are based on techniques developed in vegetation canopy studies and may not, on their own, be directly transferable to UCL studies. Therefore, a two pronged approach will be used in this study to address CS-UCL interactions: numerical model output and in-situ observations.

First, CS-UCL will be investigated using the DNS output used by Coceal et al. (2007a). As described in the literature review, the most complete conceptual model of CS-UCL interactions is found in the paper by Coceal et al. (2007a).

It should be noted that the DNS used in that study has been thoroughly evaluated against wind tunnel data, and was found to be in very good agreement (Coceal et al. 2007c). While the larger scale coherent structures (in this case, low momentum regions surrounded by hairpin vortices) are well documented features in the DNS output (Coceal et al. 2007a,c,b), details regarding how the structures interact with the underlying canopy layer flow are lacking and need to be clarified before testing against data from full-scale canopy layer flows. The clarification of the conceptual model is the focus of Chapter 2.

Second, the current methods used to study coherent structures from observational data will be tested to assess their ability to detect periods of CS-UCL interactions. Again, given the high quality of the output from the DNS used in the studies by Coceal et al., the same dataset will be used to assess current observational techniques. Assessment and adjustment of the two most widely used observational techniques will be the subject of Chapter 3.

Finally, data from the "Innovative Laboratory for Research and Education in Urban Meteorology" (ILREUM) study will be used to investigate CS-UCL interactions in urban canopy flows. Analysis of the data is based on results from Chapter 3, and the characteristics of CS-UCL interactions in the DNS output from Chapter 2 will be tested at full-scale.

Chapter 2

Coherent structure / urban canopy layer interactions

The general background regarding coherent structures has been presented in Chapter 1, with specific information regarding Coherent Structure/Urban Canopy Layer (CS-UCL) interactions in urban areas found in section 1.3. As discussed at the end of Chapter 1, limitations of these conceptual views with respect to full-scale applications will now be examined. This chapter focuses on the clarification of the conceptual views presented in Chapter 1 in preparation to study these interactions using full-scale observational data.

2.1 CS-UCL interaction studies : limitations

The conceptual views of how CS interact with the canopy shear layer were presented in the previous chapter. The first view considered came from a full-scale observational study by Louka et al. (2000) in which the flapping of the shear layer, speculated to be driven by Kelvin-Helmholtz (K-H) instabilities (the CS in this case), resulted in an unsteady, turbulent recirculation in the street canyon; it is this unsteady recirculation that is hypothesized to control the exchange of scalars and momentum across the canopy shear layer. The second view discussed comes

from a wind tunnel study by Savory and Abdelqari (2000) in which artificially generated horizontal vortices were shown to 'thicken' the shear layer, resulting in a modification of the reattachment length of the shear layer; when these interactions occurred, the reattachment length was shortened and the shear layer penetrated into the canyon. The third view considered comes from a numerical study by Coceal et al. (2007a) in which hairpin vortex packets from above the canopy layer generate sweep and ejection motions that impinge upon the canopy shear layer, resulting in an unsteady flapping. The three views are not mutually exclusive, and can actually be viewed as complementary. For example, the artificially generated vortices in the Savory and Abdelqari (2000) could be similar to the hairpin vortex structures in the Coceal et al. (2007a) study, and the unsteady flapping due to the hairpin packet sweep/ejection motions could explain the shear layer flapping found in Louka et al. (2000). In light of this compatibility, focus will be put on the model by Coceal et al. (2007a), as it is most complete.

While the Coceal et al. (2007a) model is indeed the most complete, it does lack in key areas for the purpose of framing full-scale studies of CS-UCL interactions. For example, the kinematic structure of a hairpin vortex packet is inferred from a few instantaneous visualizations and a basic conditional analysis; the main issue found here is that the conditional analysis only takes into account motions above the canopy, which do not represent the full UCL. Also, the very general approach of the conditional analysis in Coceal et al. (2007a) does not take into account the proximity of the vortices with respect to the roughness elements. While the results of Coceal et al. (2007a) suggest that the canopy shear layer may be

lifted/suppressed like a lid by ejection/sweep motions associated with hairpin vortex packets, strong evidence of such specific interactions is lacking. Therefore, to build a framework to detect and analyze these interactions at full-scale, the conceptual model must be revisited and clarified to explicitly detail how such interactions impact the entire UCL. The data used to revisit the conceptual model is the same used in the original study by Coceal et al. (2007a). A description of the dataset is presented in the next section.

2.2 DNS dataset description

The dynamical core of the DNS used in this analysis is described in Yao et al. (2001). Details regarding the setup of the particular simulation which produced the output used in this analysis, as well as its verification against wind tunnel data, can be found in Coceal et al. (2007b). The paper by Coceal et al. (2007b) also contains a detailed spatial analysis (instantaneous and conditional) of the CS present in the output.

For clarity, a brief description of the model parameters will now be discussed. The model is based on a discretized version of the Navier-Stokes equations, using a second-order central finite difference scheme in space and a second-order Adams-Bashforth scheme in time, employing the pressure correction method (see Yao et al. 2001). The domain size is $16h \times 12h \times 8h$, where h is the length dimension of the cubic roughness elements. The model employs a uniform grid spacing $\Delta = h/32$, in which the first grid point is $\Delta/2$ inside the domain boundaries. For clarity purposes, heights will be described as the distance above the first grid

point; this convention is used because the various subsets of data used in this study are available with a vertical spacing of $\Delta z = h/4$. A height denoted as $z = 1.5h$ in this study is actually $z = 1.5h + h/64 = 97h/64$ above the lower boundary of the domain. The model is integrated with a time step $\delta t = \tau/400$, where τ is the eddy turnover time $\tau = h/u_\tau$; note that the total wall shear stress, u_τ, is determined by the height independent pressure gradient used to drive the flow in the DNS (the pressure gradient is proportional to ${u_\tau}^2/H$, with H being the total height of the domain). The model output was collected over a period of 100τ after running for an initial period of about 100τ. A description of the output used in this study is presented in Table A.1.

2.3 Classification of CS-UCL interactions

The method of analysis used to clarify the conceptual model of Coceal et al. (2007a) must be carefully considered. The reason for revisiting the conceptual model is essentially due to the simple approach used in determining the location of the conditional analysis subdomain. Coceal et al. (2007a) set a conditional trigger when the persistence of the local along stream velocity at a grid point was less than 75% of the local time averaged mean. This criterion was applied to all grid points along the horizontal slice at $z = 1.5h$, which is above the array of cubes, and any subdomain associated with a grid point that met the criterion was used in the conditional analysis; however, the subdomain used in the conditional analysis did not extend below the level of $z = h$, and thus the canopy sublayer is missing. In the analysis of Coceal et al. (2007a), all subdomains

which resulted from the conditional analysis were used without considering the underlying array of cubes. This generic approach does not allow one to consider the proximity of the structure to an underlying roughness element as an important factor. In order to determine the impact of location with respect to distance from a roughness element, subdomains with the same spatial location (with respect to underlying roughness elements) are considered separately in this study (i.e. all $h \times h$ blocks directly over a cube are conditionally averaged, all $h \times h$ blocks directly downstream are conditionally averaged, etc.).

It should be mentioned that two spatial features of the CS described by Coceal et al. (2007a) could be used to highlight time periods of interest: hairpin vortices and low momentum regions. Low momentum regions (LMR) were detected by Coceal et al. (2007a) as described in the previous paragraph. Hairpin vorticies can be identified by connected regions where the second eigenvalue of the symmetric part of the acceleration gradient (excluding the unsteady irrotational straining term and viscous effects) is negative – this is the λ_2 criteria of Jeong and Hussain (1995). In effect, the λ_2 criteria highlights areas where a pressure minima is present due to vortical motion. For example, this would exclude areas where vorticity solely exists due to shear effects. However, the λ_2 analysis tends to be quite noisy and, in initial efforts, was difficult to use for identifying the presence of CS. The second feature, a LMR, was much easier to use to identify CS. The process of LMR identification will now be discussed.

2.3.1 Identification of LMRs

Following Tomkins and Adrian (2003) and Coceal et al. (2007b), an LMR can be identified at the location where the local along stream component of velocity, u, is less than 75% of the local time mean along-stream velocity. This 75% or less threshold will be referred to as the LMR criterion. While the LMR criterion could be directly applied to the block time series data from the DNS, the spatial nature of the LMR may not be fully captured. Thus, a new variable, the Low Momentum Region Index (LMR_i) is used. The LMR_i is defined as the fraction of grid points on a 2D slice within an $h \times h$ block (1024 grid points) where the LMR criterion is satisfied. An $LMR_i = 0$ would indicate no grid point within the $h \times h$ block met the LMR criterion (i.e. no LMR is present); an $LMR_i = 1$ would indicate that all grid points within an $h \times h$ block satisfy the LMR criterion (an assumed indication that an LMR is present).

An example horizontal and vertical distribution of LMR_i is shown in Fig. 2.1. The contours shown in Fig. 2.1 enclose areas where the LMR criterion is met. A comparison of the location of the contours and the LMR_i values indicates that the LMR_i parameter is capable of highlighting the location of an LMR. An instantaneous picture of an LMR can be seen on the $z = 1.5h$ horizontal slice shown in Fig. 2.1a, at the location $4h \leq x \leq 11h$ and $4h \leq y \leq 6h$, and on the vertical slice (Fig. 2.1b) by $4h \leq x \leq 11h$ and $h \leq z \leq 4h$. Using the XY slice in Fig. 2.1a, the aspect ratio of the LMR along the line y=5.5 is approximately 3.5, which is in agreement with the findings in Coceal et al. (2007b). This lends confidence to the ability of LMR_i to detect areas where LMR are present.

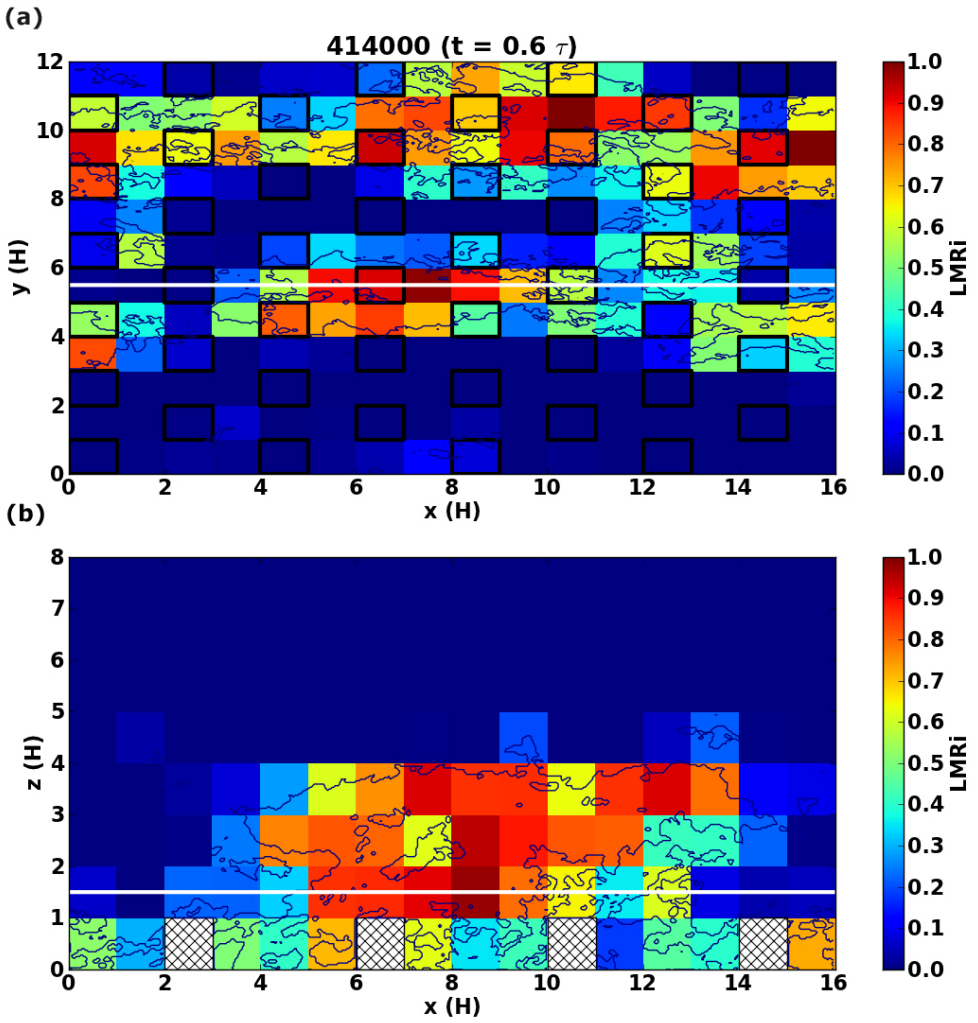

Figure 2.1: *The spatial distribution of LMR_i for a horizontal (a) and vertical (b) slice. The white horizontal lines ($y = 5.5h$ (a), $z = 1.5h$ (b)) indicate where the slices are located with respect to each other. The contoured regions in the figures indicate the bounds where the LMR criterion is met.*

In the following section, the LMR_i is used to classify CS-UCL activity to clarify the Coceal et al. (2007a) conceptual model, as well as to initially assess

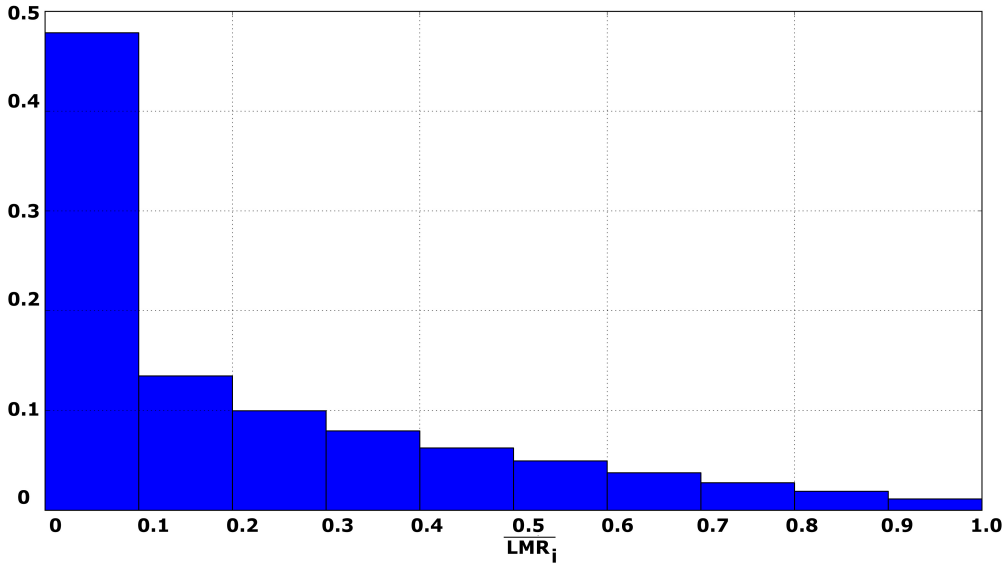

Figure 2.2: *Frequency plot of all LMR_i values computed at $z = 1.5h$.*

the importance of CS in the transport of momentum across the urban canopy layer interface.

2.3.2 Interaction classification

As shown in the previous section, LMR_i is capable of qualitatively determining the presence of an LMR. A frequency plot of all values of LMR_i on the horizontal slice located at $z = 1.5h$ is shown in Fig. 2.2 (180,480 values of LMR_i total). Based on Coceal et al. (2007a), the level $z = 1.5h$ is chosen for analysis, as this is the level at which hairpin vortex packets are expected to be found. Overall, less than 15% of LMR_i values are above 0.5, and less than 10% are above 0.6.

Fig. 2.2 seems to suggests that LMRs are not present a majority of the time *in any given part of the domain*. However, animations of maps of LMR_i suggest that LMRs are a persistent feature *in localized parts of the domain*. Therefore,

Fig. 2.2 should not be misinterpreted as suggesting that LMR are rare, but rather LMRs are persistent features that do not cover a significant amount of the spatial domain at any given time.

As an example, by using a window size of $\Delta t_w = 10\tau$, a quick visual inspection of the distributions of LMR_i at single grid point locations over the first window (i.e. first 100 XY slices) reveals that the distributions from individual blocks can be generally classified into three types: a distribution heavily weighted towards low values of LMR_i, a distribution weighted towards large values of LMR_i, and a relatively flat distribution of LMR_i. The first type, a distribution heavily weighted towards low values of LMR_i, would be indicative of a non-LMR period (i.e. the block is not associated with an LMR, Fig. 2.3). The second type, a distribution weighted towards high values of LMR_i, would indicate a period of LMR activity (Fig. 2.4). The third type, a flat distribution of LMR_i would be classified as a transition case between LMR and non-LMR periods (Fig. 2.5).

In a general sense, the discussion above would lead one to expect certain statistical properties of LMR_i over a given window size, $\Delta t_w = 10\tau$. It would be expected that a non-LMR period would be marked by a small average value of LMR_i ($\overline{LMR_i}$), a positive value for the skewness of LMR_i, $Skew_{LMR_i}$, and a positive value for kurtosis of LMR_i, $Kurt_{LMR_i}$; qualitatively, this would suggest a distribution with a sharp peak at a small value of LMR_i, with an extended tail towards higher values of LMR_i (Fig 2.3), although the values in the tail are hard to see in the figure.

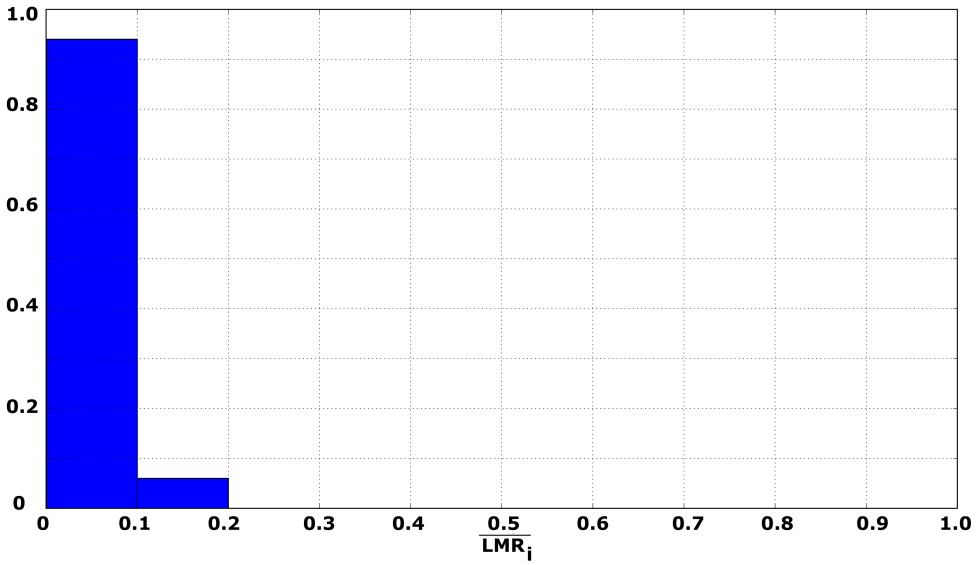

Figure 2.3: *An example of distribution of LMR_i for a non-LMR case, from grid point 24.*

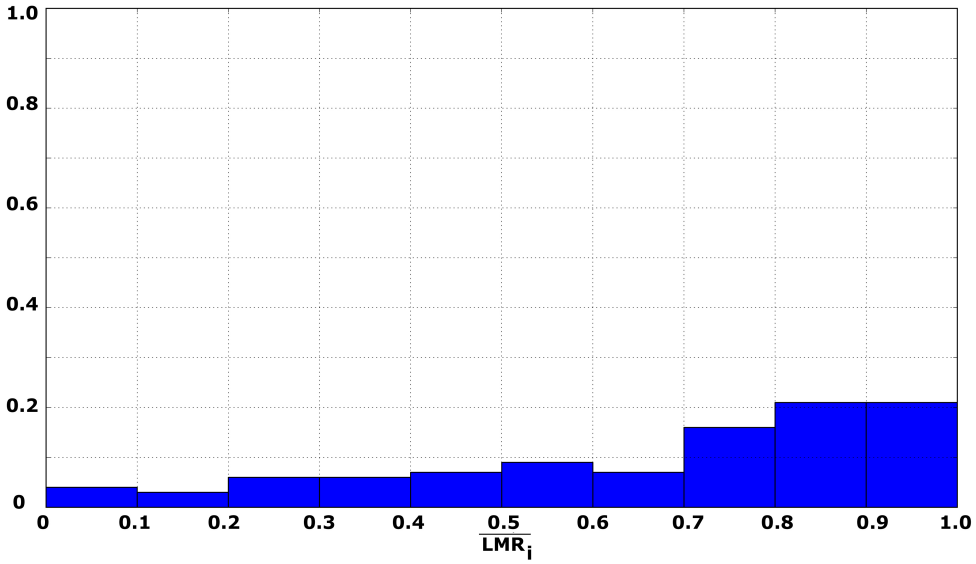

Figure 2.4: *An example of a distribution of LMR_i for a LMR case, from grid point 70.*

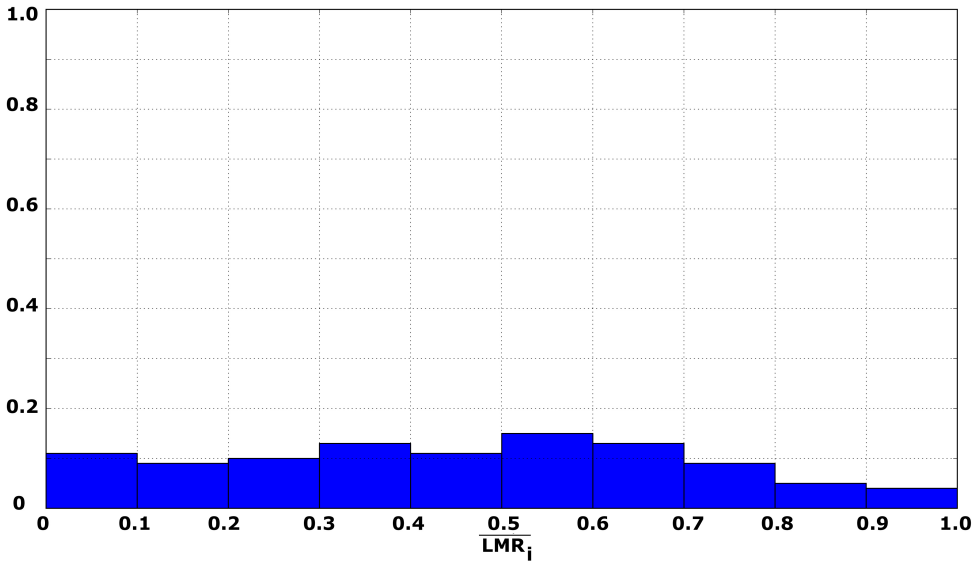

Figure 2.5: *An example of a distribution of LMR_i for an transition case, from grid point 80.*

Similarly, it would be expected that an LMR period would be marked by a large average value for $\overline{LMR_i}$, and a negative value for $Skew_{LMR_i}$ (there are no clear expectations for $Kurt_{LMR_i}$) (Fig 2.4). Transition periods would be expected to have most values around the mid-range of LMR_i, which is contained between 0 and 1, a negative value of $Kurt_{LMR_i}$ (a flat distribution), with no clear expectations for $Skew_{LMR_i}$ (Fig 2.5).

At this point, two things are not clear - how large should the analysis window size be to appropriately capture the behavior of LMRs, and what values constitute "large" and "small" values of $\overline{LMR_i}$. The answer to the former question will now be discussed in light of the expected statistical properties for the three periods (LMR, non-LMR, and transition), and will be used to answer the latter.

2.3.2.1 Analysis window size

While a window size of $\Delta t_w = 10\tau$ was used as an example in the previous section, it is unclear how this relates to LMRs (if at all): is a window size of $\Delta t_w = 10\tau$ more representative of single LMR, or more representative of the persistence time of a series of LMR? What are the appropriate window sizes to use to identify single/multiple LMR interactions with the UCL? The persistence time of a series of LMR is the quantity of interest, as this would be representative of the total interaction period between the LMR and UCL.

Through the use of the approximate length of the LMR in Fig. 2.1 ($L_{x,LMR} \approx 7h$) in combination with the estimate of the convection velocity ($U_c \approx 10h/\tau$, as estimated from visual inspection), an estimate of the time scale associated with an individual LMRs would be on the order of τ; this value is used as the smallest window considered in this study. The largest window considered will be 97.4 τ, which is the entire length of the dataset. A window between τ and 97.4 τ, representative of the persistence time of a series of LMRs, will now be determined.

The determination of the window size representative of the persistence time of a series of LMRs is based upon the behavior of statistics of LMR_i, specifically skewness and kurtosis, as a function of LMR_i averaged over a given window ($\overline{LMR_i}$). The window size, Δt_w, over which the average LMR_i ($\overline{LMR_i}$) is computed, is systematically changed until certain expected characteristics are seen in the overall statistics of $\overline{LMR_i}$; the point at which this happens will be selected as the appropriate window size that represents the persistence time of a series of LMR.

Two things of which the reader should be aware: the windows are applied as blocks (i.e. they are not moving windows in time), and the number of samples used to compute the statistics of LMR_i, N_s, will change for each window size (as shown in A.2). For example, the largest window size considered for statistical computations is $\Delta t_w = 97.4\tau$, which corresponds to the entire length of the data set of LMR_i values associated with one $h \times h$ block. In this case, $N_s = 192$ samples of each statistic are available for analysis (one sample of LMR_i from each $h \times h$ block in the domain). Also note that statistics of $LMRi$ from incomplete windows are not considered. For example, a $\Delta t_w = 10\tau$ would result in $N_w = 97$, each with $N_s = 10$, with a partial window comprising four data points being discarded.

As discussed in the previous section, an LMR period would be marked by a large average value for $\overline{LMR_i}$, and a negative value for $Skew_{LMR_i}$. Windows on the order of 10τ and smaller exhibit this behavior, as seen in Figs. 2.6(e,f,g,h,i). This would indicate an appropriate window size which represents the persistence time of a series of LMR would be 10τ (assuming large average value for $\overline{LMR_i}$ would be greater than 0.5).

A non-LMR period is expected to be marked by a "small" average value of $\overline{LMR_i}$, a $Skew_{LMR_i} > 0$, and a $Kurt_{LMR_i} < 0$. The criterion of $Skew_{LMR_i} > 0$ for "small" values of $\overline{LMR_i}$ manifests most clearly for window sizes on the order of 10τ or larger (Figs. 2.6(e,d,c,b,a)). The criteria of $Kurt_{LMR_i} < 0$ for "small" values of $\overline{LMR_i}$ are met for window sizes smaller than 10τ (Fig. 2.7).

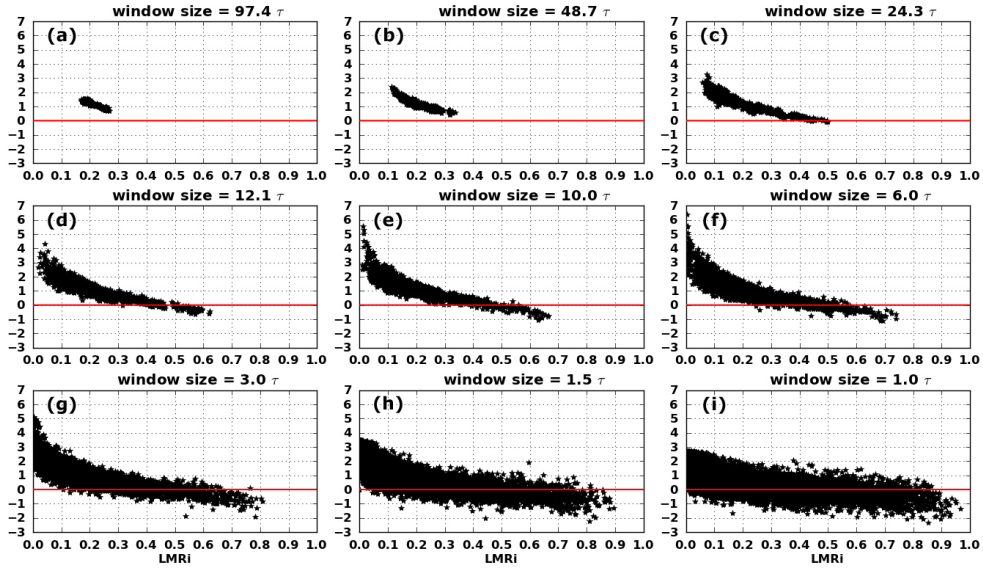

Figure 2.6: *Skewness of* $\overline{LMR_i}$ *as a function of* $\overline{LMR_i}$ *for various window sizes.*

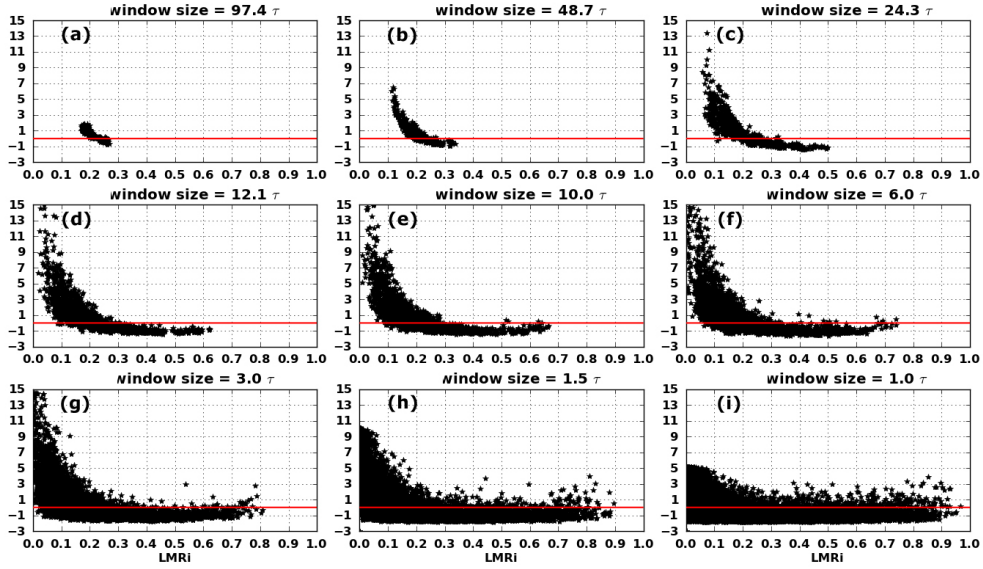

Figure 2.7: *Kurtosis of* $\overline{LMR_i}$ *as a function of* $\overline{LMR_i}$ *for various window sizes.*

Consideration of the expected behavior of $Skew_{LMR_i}$ and $Kurt_{LMR_i}$ for LMR and non-LMR periods indicates that a time window on the order of 10τ is representative of a series of LMR.

2.3.2.2 Detection bounds using $\overline{LMR_i}$

Now that a window size representative of the persistence time of a series of LMR has been found, the bounds of $\overline{LMR_i}$ associated with LMR, non-LMR, and transition periods can be determined.

A close examination $Skew_{LMR_i}$ as a function of $\overline{LMR_i}$ for a time window of 10τ (Fig. 2.6(e)) shows that the non-LMR criterion ($Skew_{LMR_i} > 0$ for small values of $\overline{LMR_i}$) begins to fail for values of $\overline{LMR_i}$ larger than 0.3; the non-LMR criterion for $Kurt_{LMR_i}$ ($Kurt_{LMR_i} < 0$ for "small" values of $\overline{LMR_i}$) begins to manifest for values of $\overline{LMR_i}$ larger than 0.1. Based on these two observations, [0, 0.2] will be the bounds of $\overline{LMR_i}$ used to determine non-LMR periods. A value of $\overline{LMR_i} = 0.3$ will be used as the lower limit for transition periods. The range of LMR_i between 0.2 and 0.3 will not be used, as it is not clear to which category those values should be classified.

If Figs. 2.6(e) and 2.7(e) are again considered, the LMR criterion ($Skew_{LMR_i} < 0$ for large values of $\overline{LMR_i}$) for a window of 10τ begins to manifest at a value of $\overline{LMR_i}$ of 0.5. Based on this observation, the bounds of $\overline{LMR_i}$ used to determine LMR periods is [0.5, 1]. A value of $\overline{LMR_i} = 0.5$ will be used as the upper limit for transition periods.

The criteria to determine LMR, non-LMR, and transition periods based on LMR_i values over a $\Delta t_w = 10\tau$ window have now been determined and are summarized in Table 2.1.

Table 2.1: Classification of time period based on statistics of $\overline{LMR_i}$

Classification	$\overline{LMR_i}$	$Skew_{LMR_i}$	$Kurt_{LMR_i}$
Periods with CS-UCL Interactions	> 0.5	< 0	$*^a$
Periods without CS-UCL Interactions	< 0.2	> 0	> 0
Transition Periods for CS-UCL Interactions	$[0.3, 0.5]$	$*^a$	< 0

[a] Statistic not used for classification purposes.

2.3.3 Summary: CS-UCL interaction classification

At this point, a classification scheme that can identify active and non-active periods of CS-UCL interactions, as well as transitional cases, has been determined and is summarized in Table 2.1. The bounds of $\overline{LMR_i}$ in Table 2.1 can be used to construct conditionally averaged views of both the canyon and canopy layer to extend and clarify the conceptual model of Coceal et al. (2007a). Note that cases which do not meet all of the criteria in Table 2.1 are dismissed from the conditional analysis. These conditional views will then be used to identify patterns in the vertical profiles of turbulence quantities; This is the subject final section of this chapter.

2.4 Clarification and extension of conceptual view

The subject of the final section of this chapter is to clarify and extend the conceptual model of Coceal et al. (2007a) to include details of the entire UCL. The criteria found in Table 2.1 are used to construct conditionally averaged views of the canyon and canopy layer during CS-UCL interactions, when CS-UCL interaction are not occurring, and CS-UCL interaction transition periods. A window size of $\Delta t_w = 10\tau$ is used to apply the criteria of the classification scheme (Table 2.1), as this window best represented the overall persistence time of LMRs. The conditional views will provide the backdrop for identification of characteristic markers of CS-UCL activity that can be obtained from very limited spatial data.

2.4.1 Conditional analysis

Conditionally averaged cross sections were constructed using vertical slice data along the line $y = 5.5h$; this location is chosen as it contained both active and non-active periods of CS-UCL interactions, as well as transitional periods, as described by Coceal et al. (2007a). An example of one such vertical slice is show in Fig. 2.1 (b). The first step in the conditional average is to apply the CS-UCL activity classification scheme outlined in Table 2.1. Statistics of $\overline{LMR_i}$ are computed over a window size $\Delta t_w = 10\tau$ for each $h \times h$ block along the vertical cross section at $y = 5.5h$ at a height of $z = 1.5h$. In addition to application of the CS-UCL interaction classification scheme, each vertical column ($h \times h$)

block, with a height of $8h$) is classified based on spatial proximity to a roughness element at the surface: directly above, one $h \times h$ block upstream, one $h \times h$ block downstream, and directly in-between two roughness elements. Vertical columns are then gathered based on common CS-UCL interaction classification and proximity to roughness elements and averaged to produce the conditional analysis. The end result is four $h \times h \times 8h$ conditionally averaged columns for each CS-UCL interaction classification along $y = 5.5h$; this allows for a full, canyon wide, UCL deep spatial view of the flow and turbulence quantities during the three CS-UCL interaction periods.

The first conditionally averaged slice is shown in Fig. 2.8 and represents a canyon wide, UCL deep view of periods without CS-UCL interactions. The figures present perturbation vectors (local time-mean removed) overlaying colored fields of Turbulence Kinetic Energy (TKE),

$$TKE = 0.5\sqrt{\overline{u'^2} + \overline{v'^2} + \overline{w'^2}}, \tag{2.1}$$

normalized by u_*^2, (2.8a), where u_* is defined as

$$u_* = \left(\overline{u'w'}^2 + \overline{v'w'}^2\right)^{1/4}, \tag{2.2}$$

and along-stream vertical kinematic momentum flux, $\overline{u'w'}$, normalized by u_* (2.8b) on vertical cross sections, and average w', also normalized by u_* on a vertical cross section (2.8d) and a horizontal slice (at z = 1.5h) (2.8d). The

canopy shear layer is clearly seen as the region of large normalized TKE values between $h \leq z \leq 2h$. Flow vectors indicate that the flow in the canopy shear layer descends into the space between roughness elements, and that along stream momentum flux is negative near the downstream wall, and very slightly positive-to-zero values near the upstream wall. Normalized vertical (perturbation) motion at z=1.5 is largely negative during periods without CS-UCL interactions. The overall downward motion, combined with the negative values of along stream momentum flux, suggests that faster flow from aloft is being transported into the canyon during these periods.

Conditionally averaged cross sections for periods of CS-UCL interactions is presented in Fig. 2.9. The relatively thin layer of large values of TKE that mark the canopy shear layer in the non-interactive periods have nearly tripled in thickness during periods of CS-UCL interactions (2.9a). A deep layer of negative perturbation vectors exists above the canopy, and the flow vectors indicate that this region of lower momentum is being fed by sub-canopy fluid. Prograde vortices can be seen atop the area of large TKE values shown in the vertical cross sections of Fig. 2.9(a,b,c), and rotational motions can be seen on either side of areas of rising motion in the horizontal cross section (Fig. 2.9d). This is strikingly consistent with the conceptual model and hypotheses made in Coceal et al. (2007a), even though sub-canopy motions were not analyzed in the conditional sense in that study. The conditional views of cases classified as transitional (Fig. 2.10) nicely fill the gap between the conditional views of periods with and without

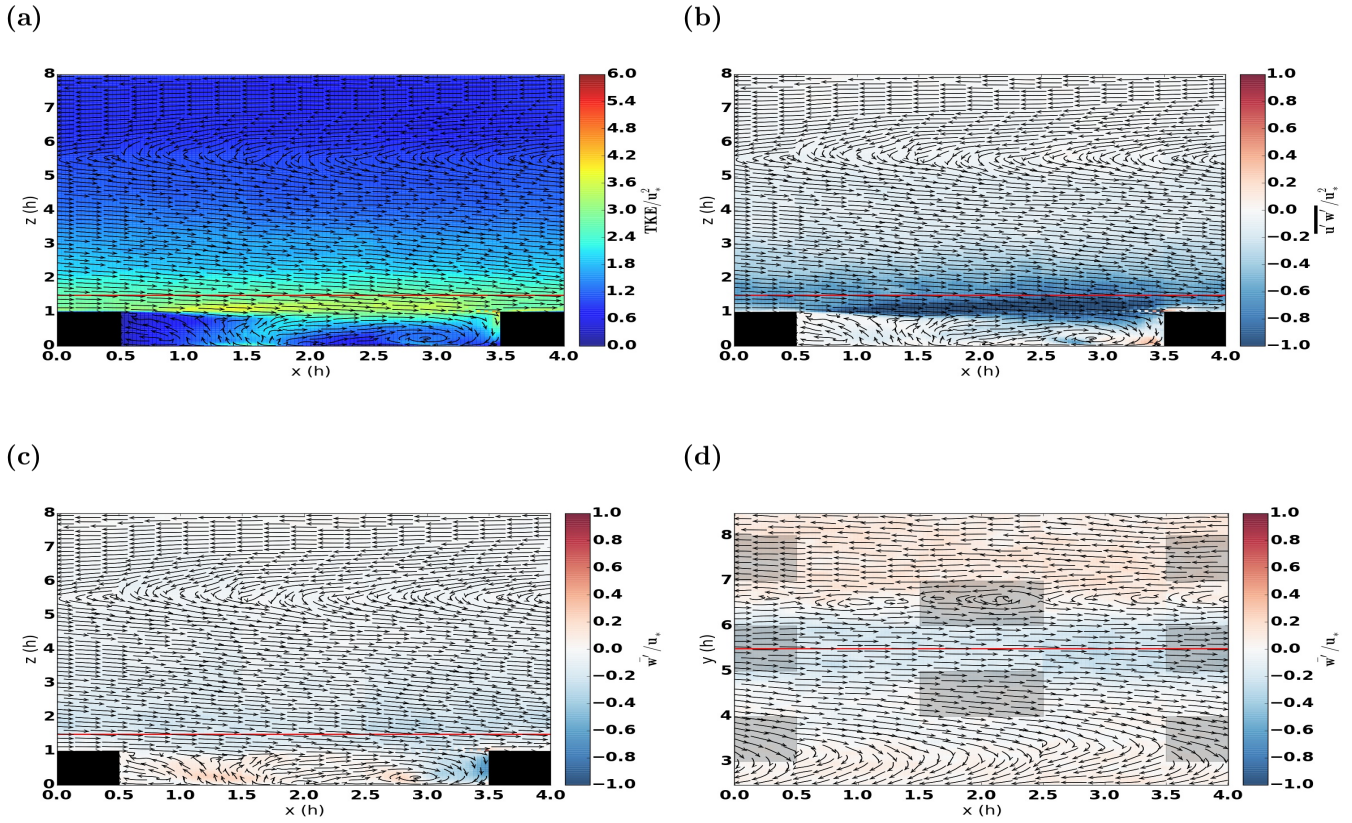

Figure 2.8: *Conditional cross sections for periods without CS-UCL interactions. Shown are perturbation vectors (local time-mean removed) overlaying colored fields of normalized TKE (a), and along-stream vertical momentum flux (b) on vertical cross sections, and average* $\overline{w'}$ *on a vertical cross section (c) and a horizontal slice (at* $z = 1.5h$*) (d).*

CS-UCL interactions, although they more closely resemble periods of CS-UCL interactions.

2.4.2 Characteristic markers

The goal of the final section of this chapter is to explore the characteristic markers of the three types of CS-UCL interaction periods as seen through vertical profiles of turbulence quantities. These markers are considered in anticipation of the full-scale study of CS-UCL interactions, where the detail of spatial information used to determine the presence of CS, as done throughout this chapter, is lacking.

Profiles are generated for each interaction period type (no CS-UCL interactions, CS-UCL interactions, and transition periods) based on spatial proximity to roughness elements: directly over an element (square markers), one $h \times h$ block upstream (circle markers), one $h \times h$ block downstream (triangle markers), and directly in-between roughness elements (dashed lines). All profiles for each $h \times h$ block type have been averaged together to produce a single profile. In general, the shape of the profiles will be discussed rather than actual values seen in the profiles, as it is not clear if the actual values, or ratios thereof, would translate into markers which could be found in full-scale observations due to differences in the Reynolds numbers of the flows. However, it is assumed that general characteristics of the shape of these profiles could be seen at full-scale.

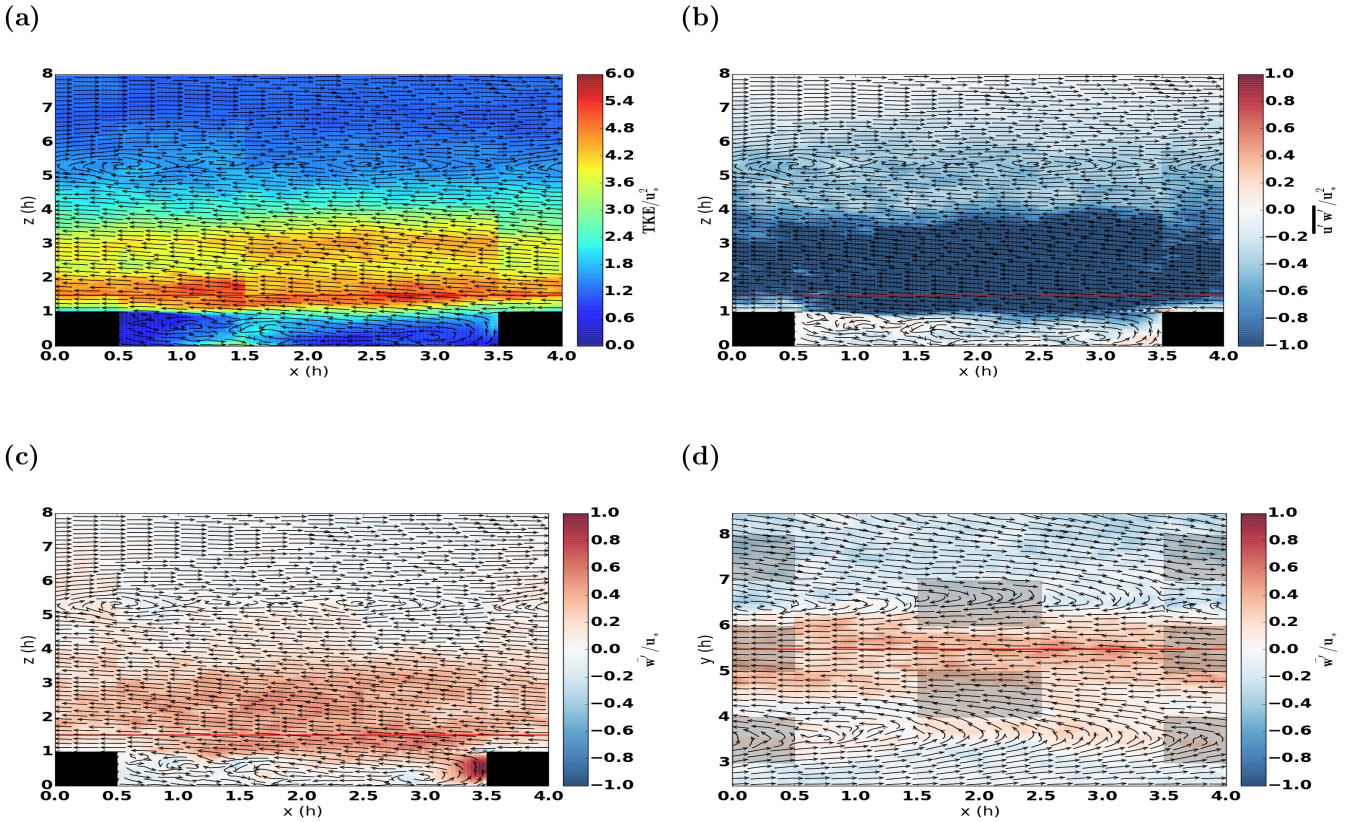

Figure 2.9: *Same as 2.8, but for periods with CS-UCL interactions.*

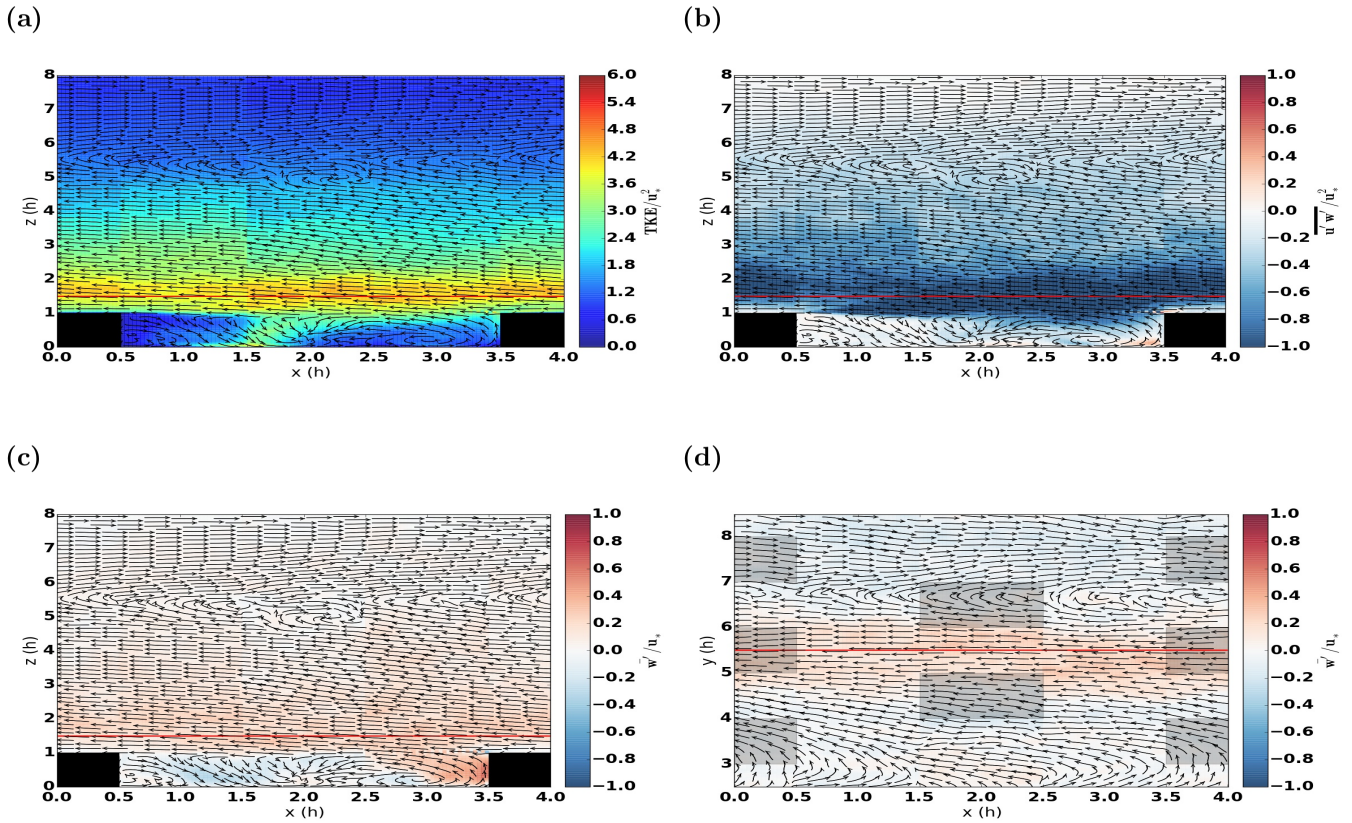

Figure 2.10: *Same as 2.8, but for transitional periods of CS-UCL interactions.*

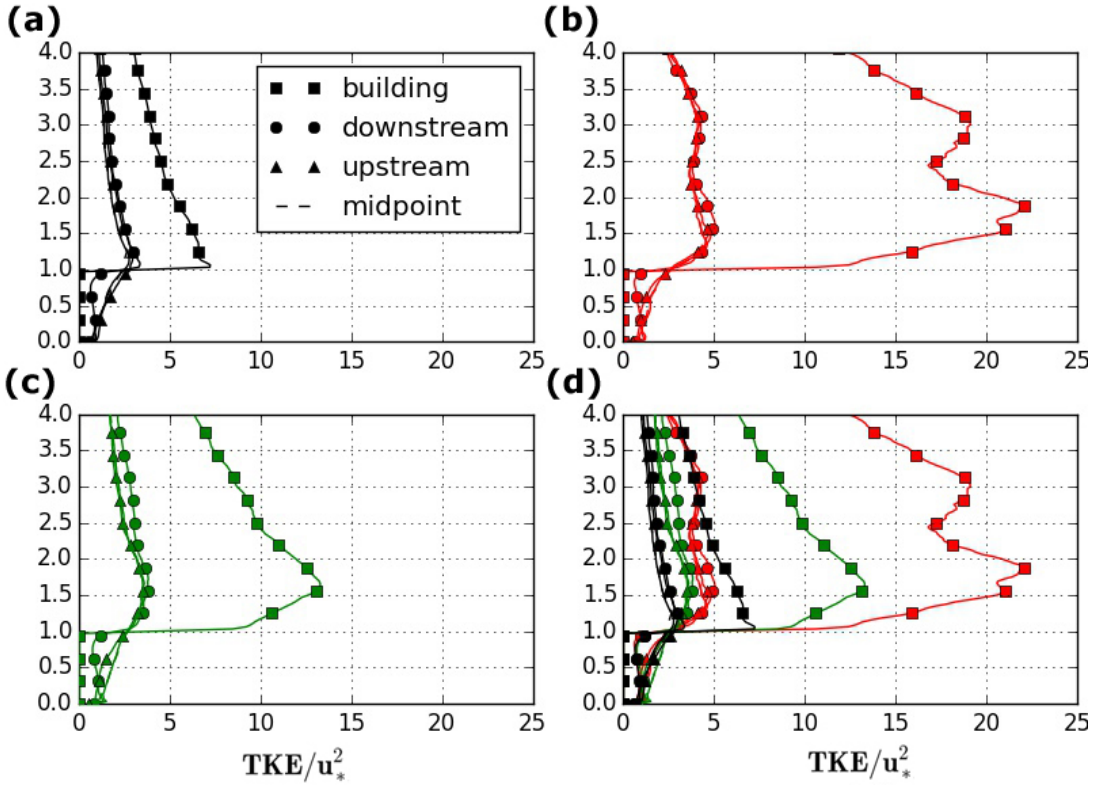

Figure 2.11: *Characteristic markers in the vertical profile of TKE for non CS-UCL interaction periods (a), CS-UCL interaction periods (b), and transitions periods (c). All three period types are presented in panel (d). There are four lines per $h \times h$ block type used to construct an average profile (one from each of the upstream, downstream, midpoint, and directly over a building block types).*

2.4.2.1 Markers in TKE profiles

The first type of profile to be considered is that of TKE, normalized by the square of the friction velocity at building height, ${u_*}^2$. Shown in Fig. 2.11 are the TKE profiles for the three CS-UCL interaction Period Types, no CS-UCL interaction (Fig. 2.11a), CS-UCL interactions (Fig. 2.11b), and transitional interactions (Fig. 2.11c), as well as a composite of all three (Fig. 2.11d).

The first thing to note regarding vertical profiles of TKE is that there appears to be no distinction between the three CS-UCL periods within the canyon. As expected, all profiles of TKE show low values inside the UCL ($z < h$) but exhibit a sharp increase near the canopy top ($z = h$). However, above the canyon, differences in the vertical profiles of TKE are seen. For non-CS-UCL interaction periods, TKE peaks near $z = h$, and decreases with height for nearly all block types; the exception in the profile from directly over a roughness element, which appears to have a thin layer of nearly uniform TKE with height between $h < z < 1.5h$, but otherwise shows a decrease with height of TKE for $z > 1.5h$. For transition and CS-UCL interaction periods, the profile of TKE exhibits a maximum above the canopy height, found closer to $z = 1.5h$, which is $0.5h$ higher than that of the non-CS-UCL interaction periods. Also in difference to non-CL-UCL periods, the profile of TKE consistently *increases* with height from $z \approx 1.75h$ before decreasing with height.

Also note the presence of a curious double peak in the vertical profile of TKE for CS-UCL interaction periods. The upper peak, located around $z = 3h$ could be indicative of the upper limit of the LMRs. The lower peak, located a $z = 2h$ over roughness elements, and $z = 1.5h$ for other block types, is likely associated with the shear layer. The behavior of this lower peak, as compared to the peak found in non-CS-UCL interaction periods, seems to suggest that the layer is both lifted (displaced vertically) as well as thickened (supporting both Coceal et al. (2007a) and Savory and Abdelqari (2000)). A summary of these markers is presented in Table 2.2.

Table 2.2: Summary of Characteristic Markers found in the verical profile of TKE

CS-UCL Period Type	Marker
Non-interaction	TKE decrease with height above $z = h$
Transition, Interaction	TKE increase with height between $z < h < 1.75h$
Interaction	Double peak in TKE profile around $1.5h < z < 2h$ and $z = 3h$

2.4.2.2 Markers in $\overline{u'w'}$ profiles

The shape of the profiles of the along-stream kinematic momentum flux, $\overline{u'w'}$, are all very similar for each of the three interaction period classifications (Fig. 2.12). All $\overline{u'w'}$ values are less than zero. The values become most negative around a height of $z = 1.5h$, although the peak is reached at slightly higher levels for CS-UCL interaction and transitional periods. The one characteristic that stands out is the presence of a double peak in $\overline{u'w'}$ for CS-UCL interaction periods; these peaks occur near $z = 1.75h$ and $z = 2.75h$. While these profiles offer visually appealing characteristics, (for example, a deeper layer of larger magnitudes of along-stream kinematic momentum flux for CS-UCL interaction periods), any characteristic markers would be difficult to identify at full-scale, as observations are typically not available at the level at which even the lowest peak is observed in the profiles.

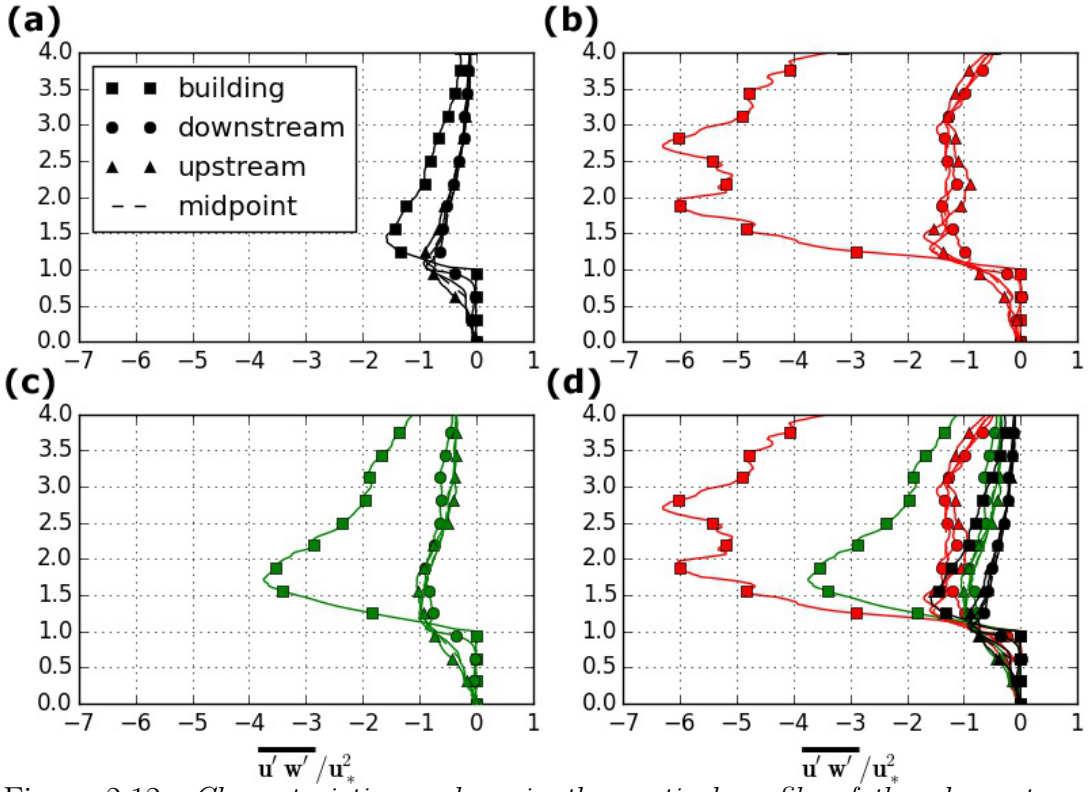

Figure 2.12: *Characteristic markers in the vertical profile of the along-stream kinematic momentum flux for non CS-UCL interaction periods (a), CS-UCL interaction periods (b), and transitions periods (c). All three period types are presented in panel (d). Profiles are constructed as described in Fig. 2.11*

2.4.2.3 Markers in $\overline{w'}$ vertical profiles

The final type of profile to be considered is that of the vertical component of perturbation velocity, $\overline{w'}$, normalized by the friction velocity at building height, ${u_*}^2$. Shown in Fig. 2.13 are the $\overline{w'}$ profiles for the three CS-UCL interaction period types, no CS-UCL interaction (2.13a), CS-UCL interactions (2.13b), and transitional interactions (2.13c), as well as a composite of all three (2.13d).

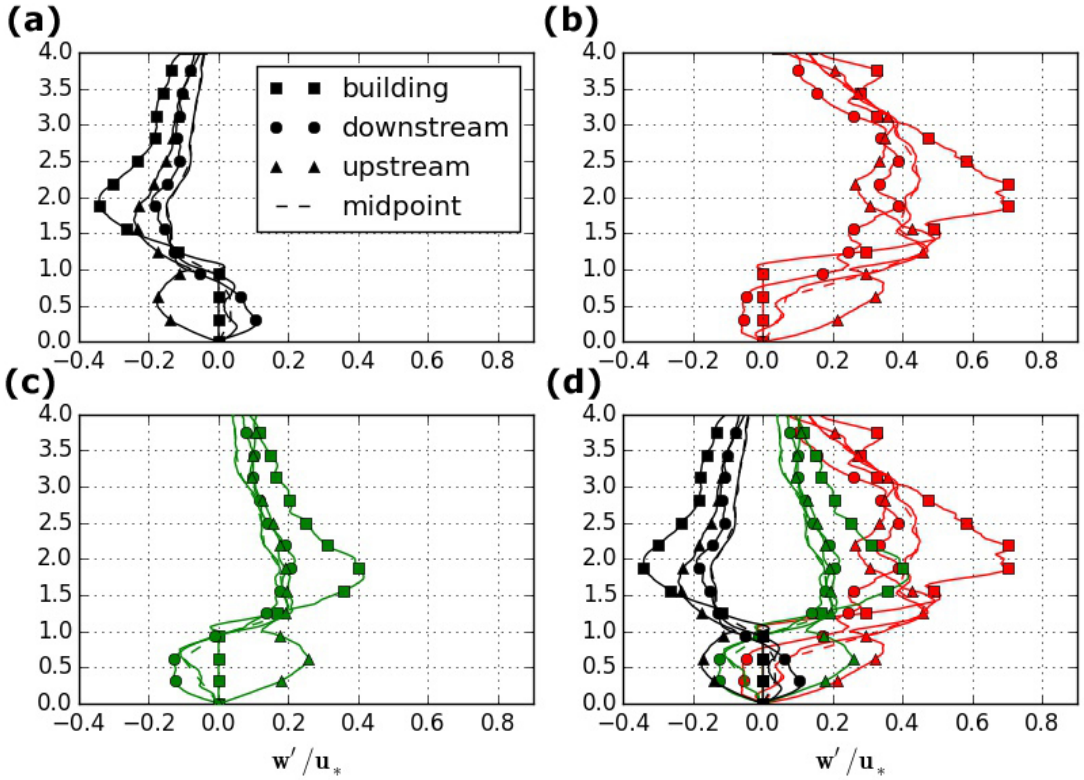

Figure 2.13: *Characteristic markers in the vertical profile of the vertical perturbation velocity for non CS-UCL interaction periods (a), CS-UCL interaction periods (b), and transitions periods (c). All three period types are presented in panel (d). Profiles are constructed as described in Fig. 2.11*

Unlike the previous profiles (TKE and along-stream momentum flux), profiles of $\overline{w'}$ exhibit both in-canyon and above canyon differences for each interaction type. Also different is that the spatial proximity to a roughness element becomes a critical factor for the markers, even for the same interaction type. Therefore, markers from the $\overline{w'}$ profiles will be discussed based on spatial proximity to a roughness element. Note than in all cases, the distinguishing factor in the profiles (both in- and above) is the sign $(+/-)$ of $\overline{w'}$.

Table 2.3: Summary of Characteristic Markers found in the verical profile of $\overline{w'}$ located one block downstream of a roughness element

CS-UCL Period Type	Inside Canyon Marker	Above Canyon Marker
Non-interaction	+	−
Transition	−	+
Interaction	− $(0 < z < 0.75h)$ + $(0.75h < z < h)$	+

One $h \times h$ block downstream from roughness element

Profiles of the vertical component of perturbation velocity one $h \times h$ block downstream from a roughness element exhibit clear differences between the three interaction period types, both inside and above the canyon.

Inside the canyon, $\overline{w'} > 0$ for non-interaction periods, while $\overline{w'} < 0$ for transition and CS-UCL interaction periods. The positive $\overline{w'}$ values associated with the non-interaction period are indicative of a downstream re-circulation, as depicted in Fig. 1.6 for isolated roughness flows ($\frac{L}{H} = 1$, $\frac{H}{W} = \frac{1}{3}$). The negative $\overline{w'}$ values associated with the transition and interaction periods may be a reflection of the disruption of the in-canyon flow caused by the withdrawal of low momentum fluid by CS. This disruption can be seen through comparison of the perturbation vector fields of the vertical conditional cross section for non-interaction periods (Fig. 2.8a) and CS-UCL interaction periods (Fig. 2.9a). For non-interaction periods, the perturbation vectors form an in-canyon rotor in which higher momentum fluid is brought into the canyon on the farthest end; in contrast, the in-canyon rotor

Table 2.4: Summary of Characteristic Markers found in the $\overline{w'}$ verical profiles located one block upstream of a roughness element

CS-UCL Period Type	Inside Canyon Marker	Above Canyon Marker
Non-interaction	$-$ (local minima at $z = 0.5h$)	$-$
Transition	$+$ (local maxima at $z = 0.5h$)	$+$
Interaction	$+$ (local maxima at $z = 0.75h$)	$+$ (local maxima at $z = 1.5h$ and $z = 3h$)

for CS-UCL interaction periods is directly opposite, in which lower momentum fluid is removed from the canyon into the canopy layer.

Outside of the canyon, the opposite is observed; $\overline{w'} < 0$ for non-interaction periods, while $\overline{w'} > 0$ for transition and CS-UCL interaction periods. The negative values of $\overline{w'}$ during non-interactive periods indicates a general sinking of the flow into the canyon on the downstream side of the roughness elements. The positive values of $\overline{w'}$ during transitional and interactive periods is a reflection of the withdrawal of lower momentum fluid from inside the canyon into the low momentum region of the CS found above the canyon.

One $h \times h$ block upstream from roughness element

Profiles of $\overline{w'}$ located inside the canyon, one $h \times h$ block upstream of a roughness element, behave opposite of those from one $h \times h$ block downstream; $\overline{w'} < 0$ for non-interaction periods, and $\overline{w'} > 0$ for transition and CS-UCL interaction periods. However, unlike profiles from one $h \times h$ block downstream of a roughness

elements, these profiles have a consistent sign $(+/-)$ for in- and above canyon flow.

As with the values of $\overline{w'}$ above the canyon in the case for one $h \times h$ block downstream from a roughness element, the negative values of $\overline{w'}$ during non-interactive periods indicates a general sinking of the flow into the canyon. Similarly, the positive values of $\overline{w'}$ found during transitional and interaction periods indicates the withdrawal of lower momentum fluid from inside the canyon into the low momentum region of the CS found above the canyon.

As with the TKE profile, the profile of $\overline{w'}$ during CS-UCL interaction periods shows a double peak around $z = 1.5h$ and $z = 3h$. Also interesting is the presence of a double peak (in the negative sense) in the $\overline{u'w'}$ profile during CS-UCL interaction periods around $z = 1.75h$ and $z = 2.75h$. The location of the peaks in $\overline{u'w'}$ relative to the peaks in TKE and $\overline{w'}$ suggests that fluid with lower momentum, originating from inside the canyon, is being transported upward throughout the layer between $z = 1.5h$ and $z = 3h$.

The $h \times h$ block between roughness elements

Profiles of $\overline{w'}$ observed in the $h \times h$ block between roughness elements behave similarly to those obtained from one $h \times h$ block downstream from a roughness element. For non-interaction and transition periods, the sign of the value of $\overline{w'}$ changes between the in-canyon portion of the profile and the above canyon portion. However, unlike the one $h \times h$ block downstream profile during CS-UCL interaction periods, the profile of $\overline{w'}$ is positive both inside and above the canyon.

Table 2.5: Summary of Characteristic Markers found in the verical profile of $\overline{w'}$ located in the block between roughness elements

CS-UCL Period Type	Inside Canyon Marker	Above Canyon Marker
Non-interaction	+	−
Transition	−	+
Interaction	+	+ (local maxima at $z = 1.5h$ and $z = 3h$)

Table 2.6: Summary of Characteristic Markers found in the verical profile of $\overline{w'}$ located directly over a roughness element

CS-UCL Period Type	Above Canyon Marker (sign)
Non-interaction	−
Transition	+ (maximum at $z = 1.75h$)
Interaction	+ (local maxima at $z = 2h$ and $z = 3.5h$)

Also evident in the interaction period is the double peak feature observed in the CS-UCL interaction profiles from the one $h \times h$ upstream case (the local maxima are located at roughly the same height). This indicates that the transport of lower momentum out of the canyon occurs over a wide portion of the canyon.

Directly over a roughness element

Directly over the roughness elements, $\overline{w'}$ is negative for non-interactive periods and positive for interactive and transitional periods. This again agrees with a general sinking of the flow near the downstream side of a roughness element (seen

also in the non-interactive period profile for one $h \times h$ block downstream). The profiles for CS-UCL interaction and transitional periods show $\overline{w'} > 0$; interestingly, the CS-UCL interaction period profile shows a double peak (just as the one $h \times h$ block upstream and the $h \times h$ block in-between roughness element profiles show), although these peaks are located slightly higher ($z = 2h$ and $z = 3.5h$). This indicates that the lower momentum fluid from the canyon is being withdrawn from the downstream end of the canyon, and lifted upward throughout a depth of $\approx 3h$ over the length of the entire canyon during CS-UCL interaction periods.

2.5 Summary of spatial DNS analysis

A framework for the analysis of CS-UCL interaction is constructed in this chapter. A classification scheme, based on a new quantity LMR_i, is developed which can identify three types of periods of interaction: CS-UCL interaction, transitional, and non-interaction periods (Table A.2).

Based on the CS-UCL interaction classification scheme, depictions of flow behavior and properties (TKE, $\overline{u'w'}$, and $\overline{w'}$) are analyzed for each of the three interaction period types using conditional analysis. These conditional views improve upon the conceptual model of Coceal et al. (2007a) by including the flow inside the canyon, as well as directly analyzing the interactions between the canyon and canopy layer flows.

It is clear from the conditional views presented in Figs. 2.8, 2.9, and 2.10, that TKE, $\overline{u'w'}$ and $\overline{w'}$ change drastically both inside and outside of the canyon,

between periods with and without CS-UCL interactions. In fact, these quantities change so drastically that they result in characteristic markers in the vertical profiles of those quantities (Figs. 2.4.2.1, 2.4.2.2, and 2.4.2.3). A summary of these characteristic markers is found in Tables 2.2, 2.3, 2.4, 2.5. and 2.6. The consistency of these differences with previous studies and hypotheses from the literature indicate that LMR_i, and the statistical properties thereof, are capable of classifying CS-UCL interaction and non-interaction periods.

Now that CS-UCL interaction and non-interaction periods can be identified using the classification scheme found in Table A.2, traditional time series analysis procedures long thought to identify periods of CS-UCL interactions are tested using time series data from the DNS output. If the time series analysis procedures are successful at capturing CS-UCL interaction periods, then they will be applied at full-scale; average profiles obtained from the periods where CS-UCL interactions are detected at full-scale are computed to see if the features in the characteristic profiles described in this section manifest at full-scale.

Chapter 3

Coherent structures in simulated time series data

A new CS-UCL interaction classification scheme was developed in Chapter 2. In this chapter, this scheme is used to measure the actual impact of CS-UCL interactions as manifested in time series data from individual grid points in the DNS dataset. The actual impact of CS-UCL interactions is then compared to the impact as determined using the two most widely used conditional sampling techniques employed in full-scale time series analysis: the Quadrant Hole method and the Wavelet Analysis method. Finally, conditional cross sections created using the conditional samples, as determined by each full-scale techniques, are compared to the "true" cross sections of CS-UCL interactions, which were developed in Chapter 2.

3.1 Time series analysis techniques

Conditional sampling is a term used to define a process where data are selected through the use of special criteria; essentially, conditional sampling of turbulence data along with the modification of the eddy covariance method can be used to estimate impact of coherent structures on turbulence transport. Subramanian

et al. (1982) provides an overview of several techniques based around the concept of conditional sampling. The critical issue surrounding conditional sampling is the criterion or criteria used in the selection of the sub-sample. The following sections will address two of the most commonly used techniques in the analysis of coherent structures in atmospheric surface layer flows.

Conditional cross sections created using the conditional samples, as determined by each full-scale technique, will be compared to the "true" cross sections of CS-UCL interactions, which were developed in Chapter 2. In addition, the fractional flux,

$$F_{coh} = \frac{\sum_{i=1}^{numCS} \left(\overline{u'w'}_i * t_i\right)}{\overline{u'w'} * t_{total}}, \tag{3.1}$$

where $numCS$ is the individual number of coherent structures detected and t_{total} is the total length of the time series being analyzed, and Transport Efficiency,

$$TE = \frac{F_{coh}}{TC}, \tag{3.2}$$

where TC, the time coverage of the coherent structures, computed as

$$TC = \frac{\sum_{i=1}^{numCS} t_i}{t_{total}}, \tag{3.3}$$

are computed for periods where the method detects an interaction, periods where interactions are missed by the method, and periods where the method detects

an interaction but an actual interaction was not occurring (false positives). This allows for the evaluation of how well each method is able to detect the interaction periods, and what impact false positive and missed interaction periods have on the overall computation of fractional flux and transport efficiencies.

3.1.1 Quadrant analysis

3.1.1.1 Method background

Quadrant analysis is commonly used to analyze the importance of motions associated with coherent structures, and to study how those motions contribute to the overall flux. For example, quadrant analysis has been used to determine the importance of contributions of ejection and sweep motions to the total flux over vegetation (Finnigan 1979; Shaw et al. 1983), in urban areas (Nelson et al. 2007; Christen et al. 2007), and in many physical modeling studies. In a quadrant analysis, the variables associated with the flux of choice (i.e. u' and w' for the kinematic momentum flux) are presented as a scatter plot (in the case of momentum flux, w' vs. u'). The quadrants of the scatter plot would be associated with specific event types (Shaw et al. 1983):

Quadrant 1 ($u' > 0, w' > 0$): Outward interaction

Quadrant 2 ($u' < 0, w' > 0$): Burst or ejection

Quadrant 3 ($u' < 0, w' < 0$): Inward interaction

Quadrant 4 ($u' > 0, w' < 0$): Sweep or gust

A threshold condition (i.e. hole) can be applied to the data such that arbitrarily small values of $u'w'$ can be excluded from the analysis, thus separating the events into small and large types (Fig. 3.1). The values of $u'w'$ that exceed the threshold condition, H

$$H = |u'w'|/|\overline{u'w'}|, \tag{3.4}$$

can then be used to determine a flux value using only the points outside of the hole, or limited to specific quadrants.

Results from vegetative canopy studies indicate that the major contributor to momentum transfer within and just above the canopy are sweep motions (quadrant 2), representing the penetration of the canopy by fast, downward moving gusts ($u' > 0; w' < 0$); the next most important motions are ejections (quadrant 4, $u' < 0; w' > 0$) (Finnigan 2000); similar results have been obtained in urban street canyon studies (Nelson et al. 2007; Christen et al. 2007).

Quadrant hole analysis has also been used to estimate the contribution of coherent structures to the total flux (Thomas and Foken 2007b; Christen et al. 2007, for example) by applying the quadrant hole analysis to identify periods when coherent structures are present. Values of $u'w'$ above the threshold are used to compute a covariance that is then associated with the transport of momentum by coherent structures. It is importance to note that the quadrant hole analysis only separates large events from small, and does not guarantee the separation of coherent motions. Gao et al. (1989) note further limitations in the use of quadrant hole analysis, specifically that it *(i)* depends on the definition of threshold values

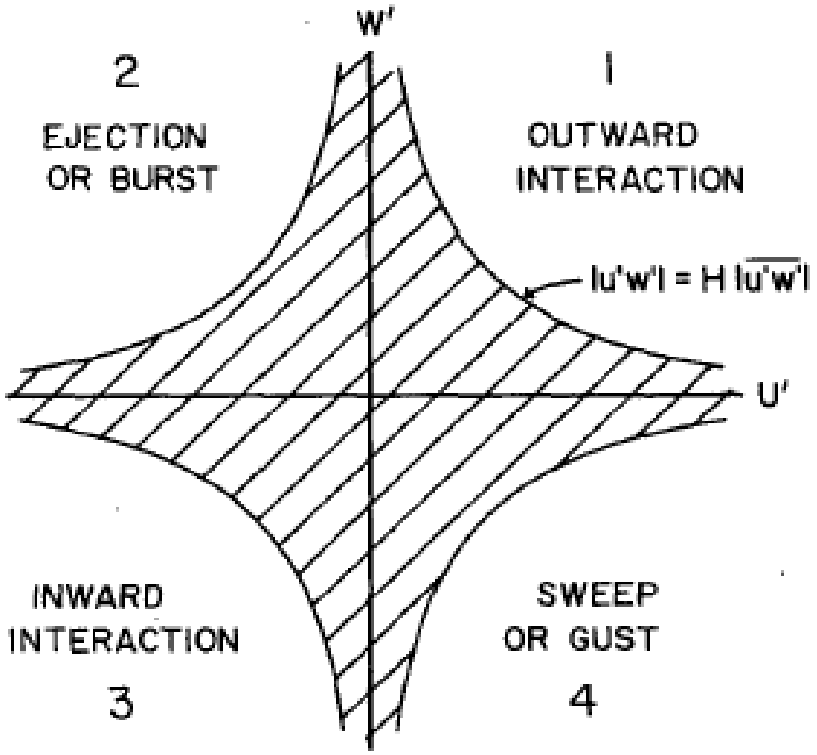

Figure 3.1: *In quadrant analysis, each quadrant is associated with a particular type of motion. A hyperbolic region (hole, indicated in the stippled region) is defined using a threshold criteria to exclude events with arbitrarily small values of $u'w'$. Fluxes are then computed for each quadrant, excluding events within the hole. (Shaw et al. 1983).*

which may introduce subjectivity to a certain degree, and *(ii)* systematically underestimates the flux contribution of ejections. For vegetative canopies, the latter has been attributed to the fact that sweep and ejection phases tend to be asymmetric events, as the sweep phase consists of fewer strong events, in contrast to the ejection phase which is characterized by more frequent moderate events (Thomas and Foken 2007b). However, in the urban environment, Christen et al.

(2007) found periods where the asymmetry changed from sweep dominant to ones in which ejections were dominant.

3.1.1.2 Quadrant analysis of simulated time series

In this section, results from using the quadrant-hole method are compared to those obtained using the LMR_i classification method developed in Chapter 2; note that results computed from the LMR_i method will be treated as "truth" as to whether or not an LMR was present when evaluating the quadrant-hole methods detection ability. The LMR_i method, as used in this section, utilized LMR_i values computed on a horizontal plane located at a height of $z = 1.5h$, the statistics of which were computed over a $\Delta t_w = 10\tau$ time window.

The way in which the quadrant-hole method was applied to the simulated time series is slightly different than what is typically used in the field, and will now be described. Simulated time series of u and w are obtained from grid points at a height of $z = 1.5h$, located at the center of a horizontal $h \times h$ block, as depicted in Fig. 2.1. Perturbation values of u (w) are calculated by removing the mean value $\overline{u}$ ($\overline{w}$); the mean value is computed over the entire length of the simulated time series. Typically, the covariance of the time series would be computed at this step using all u, w points from the time series outside of the "hole". However, in a departure from what is typically used in the field, kinematic momentum flux values, $\overline{u'w'}$, are computed over each of the 98 $\Delta t_w = 10\tau$ wide time windows; these values (98 in total) are then compared to the kinematic momentum flux computed over the entire simulated time series. If $\overline{u'w'}_{window}$ is greater than

$H * \overline{u'w'}$, then the window is marked as a CS-UCL interaction period, otherwise, the period is marked as a non-interaction period.

The periods of potential CS-UCL iterations, as detected by the quadrant-hole method, are compared against the periods where LMR are present to see how well the method is able to represent the LMR impacts.

First, conditional cross sections created using quadrant hole classification are compared to the conditional cross sections created by using the LMR_i based classification scheme of Chapter 2. As shown in Fig. 3.2, the conditional cross section computed using actual LMR periods (Fig. 3.23.2a) appears much different than the conditional cross sections created using the quadrant-hole method with hole sizes of 0.25 (Fig. 3.2b), 0.5 (Fig. 3.2c), and 0.75 (Fig. 3.2d). Note that Raupach et al. (1986) defined a hole size H = 1/2 as the threshold above which half of the flux density occurs; this was later interpreted as the intensity (size) of structures dominating (half of) the flux Christen et al. (2007), and has been used to determine the impact of coherent structures.

For all hole sizes presented in Fig. 3.2, the perturbation flow above the buildings does not represent a clear case of a low momentum region, and the flow in the canyon between $x = 3h$ and $x = 3.5h$ is completely opposite of that which is found in the actual LMR cross section. Interestingly enough, the flow between $x = 0.5h$ and $x = 1.5h$ isn't much different, indicating that the flow in the $h \times h$ block immediately downstream of the roughness element is dominated by the presence of the roughness element itself.

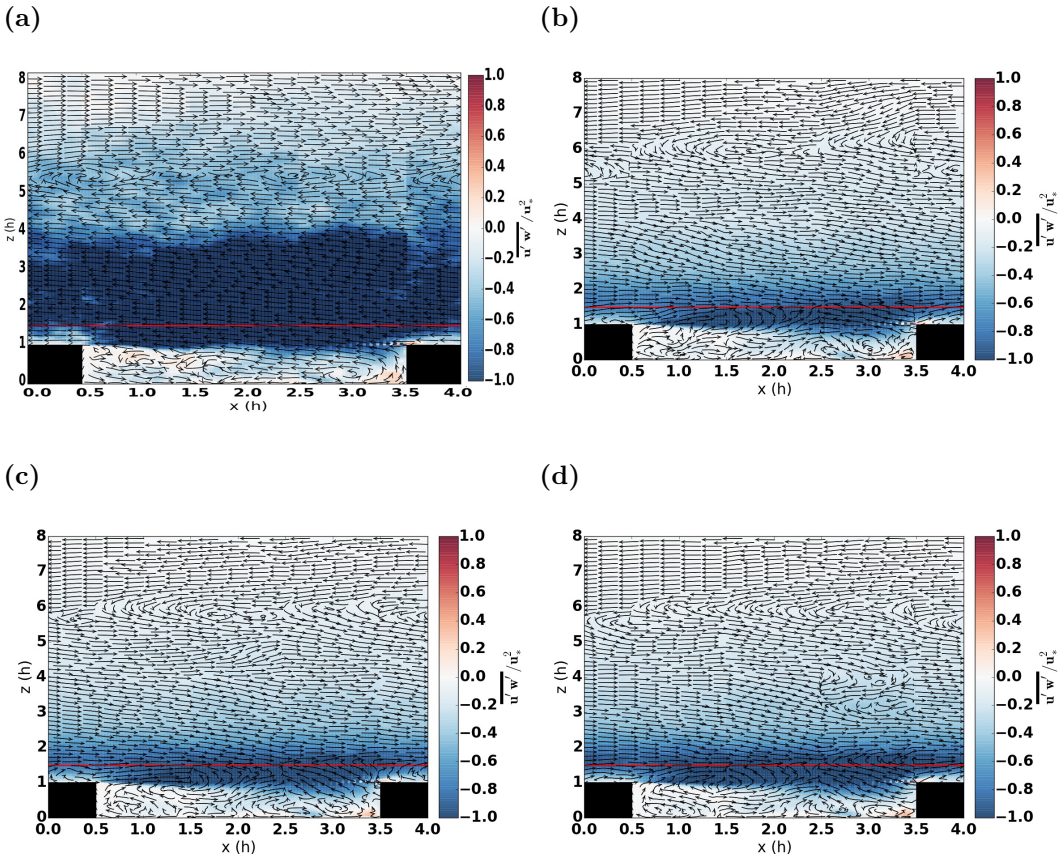

Figure 3.2: *Conditional cross sections of CS-UCL interactions (a) compared to the conditional cross sections using the quadrant analysis detection method with a hole size of 0.25 (b), 0.5 (c), and 0.75 (d).*

To further clarify the ability of the quadrant-hole method's ability to assess CS-UCL interactions, method detection statistics are computed. Table 3.1 shows the number of actual CS-UCL interaction periods, the average total number of quadrant hole detected interaction periods (by hole size), and a break down of method detected period by, on average, how many periods are successfully detected, how many are false positives, and how many interaction periods are missed by the method. Results are stratified by $h \times h$ block type and hole size.

The results in Table 3.1 show that the quadrant-hole method successfully detects nearly all CS-UCL interaction periods, although the detection ability tends to decrease with increasing hole size. While a high rate-of-detection is good, the total number of periods the method detects is more than an order of magnitude greater than the number of actual interactions. The large number of false positives is likely why the conditional cross sections in Fig. 3.2 do not compare well with the actual cross sections of CS-UCL interactions.

To get a better understanding of the impact of the large number of false positive detection, the quantities of fractional flux and Transport Efficiency are calculated for each detection type (successful, missed, and false positive). These values are shown in Table 3.2, along with a summary of the percentage of detection, which is based on Table 3.1. The percentage of successful detection is based on how many of the actual interaction periods are detected by the quadrant-hole method; the percentage of missed, or Not Detected, is the percentage of the number of actual interaction periods that are missed; the percentage of false detections are based on how many of the total periods detected by the quadrant-hole

Table 3.1: The average total number of quadrant-hole detected interaction periods (by hole size - 0.25, 0.5, and 0.75), and a break down by, on average, how many periods were successfully detected, how many were false positives, and how many interaction periods were missed by the quadrant hole detection method, as a function of spatial proximity to a roughness element. Also included is the number of actual CS-UCL interaction periods as determined using the $\overline{LMR_i}$ classification scheme from Chapter 2.

	Midpoint	Upstream	Building	Downstream
Average Number of CS-UCL Interaction Periods				
CS-UCL Interaction Periods	6.0	5.5	4.2	3.8
Total Number of Detected Periods	(28.2, 22.0, 19.0)	(23.0, 21.0, 16.8)	(27.0, 23.5, 17.8)	(22.8, 19.8, 15.5)
Successfully Detected	(5.5, 4.8, 4.0)	(5.5, 5.5, 5.0)	(3.8, 3.8, 2.5)	(3.5, 3.0, 2.8)
Missed CS-UCL Interactions	(0.5, 1.2, 2.0)	(0.0, 0.0, 0.5)	(0.5, 0.5, 1.8)	(0.2, 0.8, 1.0)
False Positives	(22.8, 17.2, 15.0)	(17.5, 15.5, 11.8)	(23.2, 19.8, 15.2)	(19.2, 16.8, 12.8)

method are false positives. It is clear that many of the periods where the quadrant hole detected interactions are actually false positives (around 80%). The fractional flux (fraction of the total time series flux) from the periods detected by the quadrant-hole method are quite high (greater than 0.9 in most cases), while the actual fractional flux computed for CS-UCL interaction periods is much smaller (between 0.16 and 0.31). These results indicate that the quadrant-hole method, without modification, is not a good method for assessing the impact of LMRs, as it will overestimate the impacts of LMRs.

A simple modification can be made to the quadrant-hole method if the conceptual model of Coceal et al. (2007a) is considered. Recall that, as shown in Fig. 1.5, areas located below an LMR are expected to have Q_2, or ejection, events. If the quadrant-hole method as applied above is further restricted to only include periods where ejection events are predominant, then the detection ability is dramatically improved (see Tables 3.3 and 3.4). While the percentage of the successfully Detected interaction periods is high, and the percentage of undetected periods are low, the percentage of false positives is still greater than 20% of the total number of detected interactions (Table 3.3). The fractional flux, however, indicates that the false positive periods account for less than 8% of the total flux for the mid-canyon $h \times h$ block, as well as the $h \times h$ block immediately upstream from a roughness element. The fractional flux for the quadrant hole detected interactions is still a bit high compared to what is expected, with values 5% greater than the actual values for most hole sizes, with the exception being

Table 3.2: Percentages of detection, fractional flux values, and transport efficiencies, broken down by successful, missed, and false positive detections as determined by using the quadrant-hole detection method with hole values of 0.25, 0.5, and 0.75.

	Midpoint	Upstream	Building	Downstream
Percentages of Detection (%)				
Successfully Detected	(92.3, 81.5, 68.2)	(100.0, 100.0, 88.1)	(90.0, 90.0, 57.5)	(93.8, 80.4, 75.4)
Not Detected	(7.7, 18.5, 31.8)	(0.0, 0.0, 11.9)	(10.0, 10.0, 42.5)	(6.2, 19.6, 24.6)
Method False Detection	(80.5, 78.4, 79.1)	(76.4, 74.4, 71.0)	(85.9, 83.8, 85.6)	(83.2, 83.4, 80.1)
Fraction of total kinematic momentum flux				
CS-UCL Interaction	0.25	0.31	0.16	0.17
Method Detected	(0.99, 0.93, 0.88)	(0.99, 0.97, 0.89)	(1.0, 0.95, 0.87)	(0.99, 0.94, 0.85)
Method Missed	(0.0, 0.01, 0.03)	(0.0, 0.0, 0.02)	(0.0, 0.0, 0.02)	(0.0, 0.01, 0.02)
Method False Detection	(0.74, 0.69, 0.65)	(0.69, 0.67, 0.6)	(0.84, 0.8, 0.73)	(0.82, 0.78, 0.7)
Transport Efficiency				
CS-UCL Interaction	1.41	1.49	1.14	1.16
Method Detected	(1.12, 1.36, 1.48)	(1.15, 1.23, 1.41)	(1.08, 1.19, 1.44)	(1.16, 1.28, 1.52)
Method Missed	(0.1, 0.27, 0.41)	(0.0, 0.0, 0.53)	(0.04, 0.04, 0.36)	(0.02, 0.19, 0.24)
Method False Detection	(1.05, 1.28, 1.39)	(1.04, 1.14, 1.34)	(1.06, 1.18, 1.41)	(1.17, 1.28, 1.57)

for the $h \times h$ block directly upstream from a roughness element ($\approx 2\%$). In general, the ability of the modified quadrant-hole method to characterize CS-UCL interactions is better at smaller hole sizes, and is overall quite good.

Although not shown, the fractional fluxes associated with Q4 (sweep) motions nearly make up the difference between the fractional fluxes associated with Q2 (ejection) events and the fractional fluxes determined using the unmodified quadrant hole technique. This suggests that the unmodified technique is picking up on both Q2 and Q4 events, although only the Q2 events seem to be representative of the actual CS-UCL interactions.

Finally, consideration of the conditional cross section created using the modified quadrant-hole method (Fig 3.3) shows a marked improvement over the comparison based on the unmodified quadrant-hole method derived cross sections. The reverse flow in the perturbation flow vector field is now clearly shown, and the in-canyon flow closely matches what is found in the actual CS-UCL cross sections (i.e. a clear rotor one block upstream of the roughness element). The biggest difference in the cross sections is thickness of the normalized along-stream kinematic momentum flux layer (dark blue layer between $z = h$ and $z = 4h$). The actual CS-UCL interaction periods conditional cross section along-stream kinematic momentum flux layer (Fig. 3.3a) is thicker than in the modified quadrant-hole method cross sections. This is potentially due to the number of false positives still attributed to the modified quadrant-hole method.

Overall, the modified quadrant-hole method shows a dramatic improvement over the standard quadrant-hole method. Special care should be taken that the

Table 3.3: The same as Table 3.1, but for the modified quadrant hole detection method (i.e. ejection events only).

	Midpoint	Upstream	Building	Downstream
Percentages of Detection				
CS-UCL Interaction Periods	6.0	5.5	4.2	3.8
Total Number of Detected Periods	(8.0, 6.8, 5.8)	(7.5, 7.5, 6.2)	(6.2, 5.8, 4.2)	(6.2, 5.2, 4.2)
Successfully Detected	(5.5, 4.8, 4.0)	(5.5, 5.5, 5.0)	(3.5, 3.5, 2.5)	(3.2, 2.8, 2.5)
Missed CS-UCL Interactions	(0.5, 1.2, 2.0)	(0.0, 0.0, 0.5)	(0.8, 0.8, 1.8)	(0.5, 1.0, 1.2)
False Positives	(2.5, 2.0, 1.8)	(2.0, 2.0, 1.2)	(2.8, 2.2, 1.8)	(3.0, 2.5, 1.8)

Table 3.4: The same as Table 3.2, but for the modified quadrant hole detection method (i.e. ejection events only).

	Midpoint	Upstream	Building	Downstream
Percentages of Detection (%)				
Successfully Detected	(92.3, 81.5, 68.2)	(100.0, 100.0, 88.1)	(85.0, 85.0, 57.5)	(87.5, 74.2, 69.2)
Not Detected	(7.7, 18.5, 31.8)	(0.0, 0.0, 11.9)	(15.0, 15.0, 42.5)	(12.5, 25.8, 30.8)
Method False Detection	(28.8, 27.4, 30.1)	(20.4, 20.4, 11.4)	(39.9, 37.8, 42.5)	(46.5, 46.7, 41.2)
Fraction of total kinematic momentum flux				
CS-UCL Interaction	0.25	0.31	0.16	0.17
Method Detected	(0.33, 0.31, 0.29)	(0.36, 0.36, 0.33)	(0.25, 0.24, 0.22)	(0.3, 0.28, 0.26)
Method Missed	(0.0, 0.01, 0.03)	(0.0, 0.0, 0.02)	(0.01, 0.01, 0.02)	(0.07, 0.02, 0.01)
Method False Detection	(0.08, 0.07, 0.07)	(0.07, 0.07, 0.15)	(0.09, 0.08, 0.07)	(0.11, 0.1, 0.09)
Transport Efficiency				
CS-UCL Interaction	1.41	1.49	1.14	1.16
Method Detected	(1.41, 1.54, 1.66)	(1.33, 1.33, 1.56)	(1.21, 1.27, 1.47)	(1.24, 1.39, 1.57)
Method Missed	(0.1, 0.27, 0.41)	(0.0, 0.0, 0.53)	(0.06, 0.06, 0.36)	(0.88, 0.09, 0.04)
Method False Detection	(1.01, 1.16, 1.2)	(0.62, 0.62, 0.9)	(1.12, 1.18, 1.28)	(1.11, 1.18, 1.29)

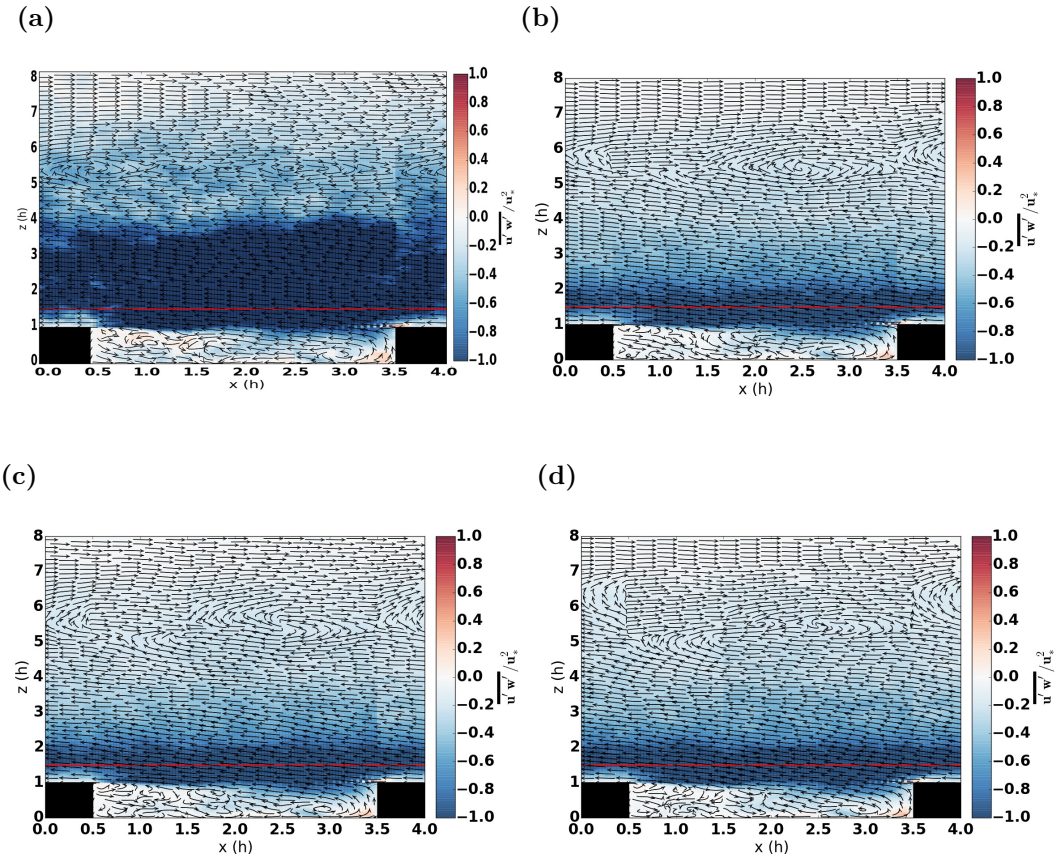

Figure 3.3: *CS-UCL interaction conditional cross section (a) compared to the conditional cross sections using modified quadrant-hole detection method (i.e. limited to ejection events), with a hole size of 0.25 (b), 0.5 (c), and 0.75 (d).*

method is not applied in locations directly downstream from roughness elements, as the results suggest that these regions are dominated by wake effects.

3.1.2 Wavelet analysis

3.1.2.1 Method background

The main operation involved in Fourier analysis is the change of basis from the standard to a set of complex exponentials, which results in a transformation from the time domain to the frequency domain. This change of basis process results in the delocalization of information in the time series - that is, local information (such as the temporal location of spikes and ramps) is spread across the frequency spectrum. In wavelet analysis, the delocalization problem is addressed by using a set of mother wavelets, $g_{\alpha,\beta,p}$, in place of the complex exponentials used in the Fourier transform. Unlike the complex exponentials used in Fourier analysis, the mother wavelets used in wavelet analysis are finite waveforms.

The wavelet transform of a 1D time series, $x(t)$, is given by

$$W_p(\alpha, \beta, p) = \int_{-\infty}^{\infty} x(t) g_{\alpha,\beta,p}(t) dt, \tag{3.5}$$

where the parameters α, β, and p refer to the dilation (stretching, shrinking of the wavelet along the time axis), translation (movement of the center of the wavelet along the time axis), and amplification parameters of the mother wavelet. Typically, the amplification factor, p, is set to 1, and is often not mentioned.

As shown shortly, it is through the dilation and translation parameters that information regarding the scale of the features in the time series can be extracted.

The most commonly used mother wavelets in turbulence studies are the Haar (Collineau and Brunet 1993),

$$g(t) = \begin{cases} 1, & \text{if } -0.5 <= t < 0; \\ -1, & \text{if } 0 < t <= 0.5; \\ 0, & \text{otherwise.} \end{cases} \tag{3.6}$$

Morlet (Torrence and Compo 1998),

$$\begin{aligned} g(t) &= \pi^{-1/4} e^{i\omega_0 t} e^{t^2/2} \\ \omega_0 &= \text{constant} \end{aligned} \tag{3.7}$$

and Mexican Hat or the Second Derivative of a Gaussian (SDG) (Collineau and Brunet 1993),

$$g(t) = (1 - t^2) e^{-t^2/2} \tag{3.8}$$

Note that the three mother wavelets above are written as a function of time. In order to incorporate these mother wavelets into a wavelet analysis, the dilation and translation parameters must be included. As an example, the SDG mother wavelet can be rewritten to incorporate the dilation (α) and translation (β) parameters as

$$g(t) = \left(1 - \frac{(t-\beta)^2}{\alpha}\right) e^{-\frac{(t-\beta)^2}{2\alpha}}. \tag{3.9}$$

The behavior of these common mother wavelets in both the time and frequency domains can be seen in Fig. 3.4.

Note the behavior of the SDG wavelet in the time and frequency domains as α changes; a smaller width in the time domain results in a larger width in the frequency domain. This relationship can be characterized through the use of Heisenberg boxes in the time-frequency domain. The Heisenberg boxes for the Morlet mother wavelet are shown in Fig. 3.5. The area of the Heisenberg box is preserved for a given wavelet, and an inverse relationship between localization in the time and frequency domains is forced.

Often of importance is the global wavelet spectrum, defined as

$$\overline{W(\alpha)} = \int_{-\infty}^{\infty} \|W(\alpha,\beta)\|^2 d\beta \tag{3.10}$$

which is an estimate of the power spectrum of the time series. Peaks in the global wavelet power spectrum have been used to determine the scale at which coherent structures are likely to exist.

Detection Algorithm The choice of mother wavelet depends on the application, as each has different localization properties in the time and frequency domain. For example, the SDG wavelet is moderately well localized in the time and frequency domains and is able to detect the ramp-like features associated

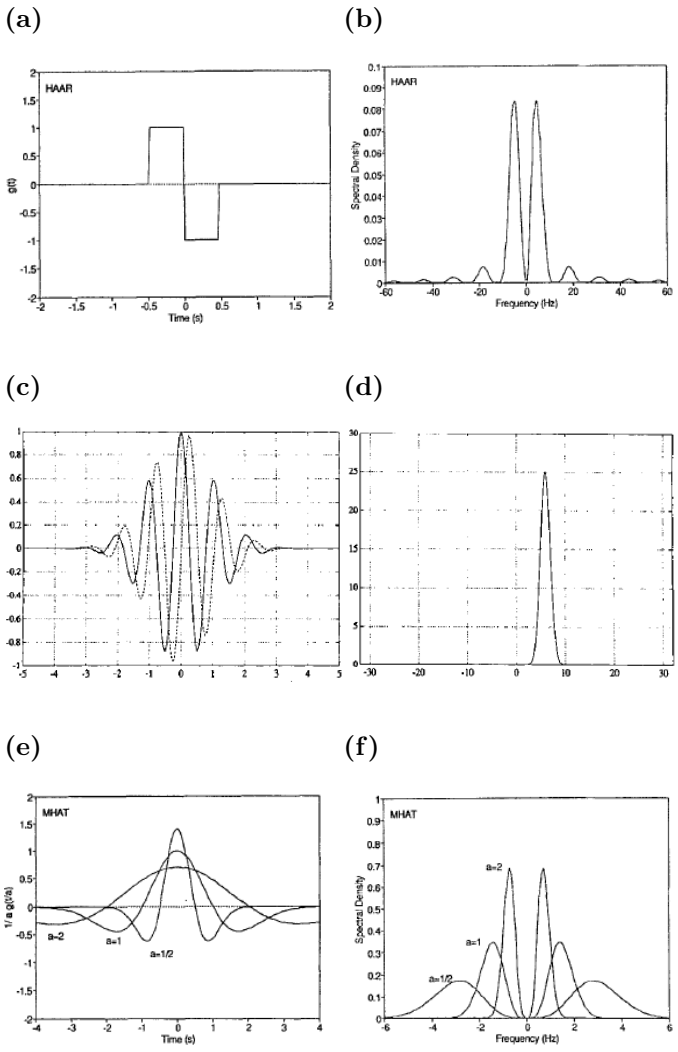

Figure 3.4: *The most common mother wavelets for the analysis of turbulence (left), and their associated Fourier spectrum (right): Haar (a,b), Morlet (c,d; dotted line represents complex component), and Mexican Hat or Second Derivative of a Gaussian (e,f). (a),(b),(e) and (f) are from Collineau and Brunet (1993), and (b) and (c) from Farge (1992). The effect of dilation is shown for the SDG wavelet in both the time and frequency domains.*

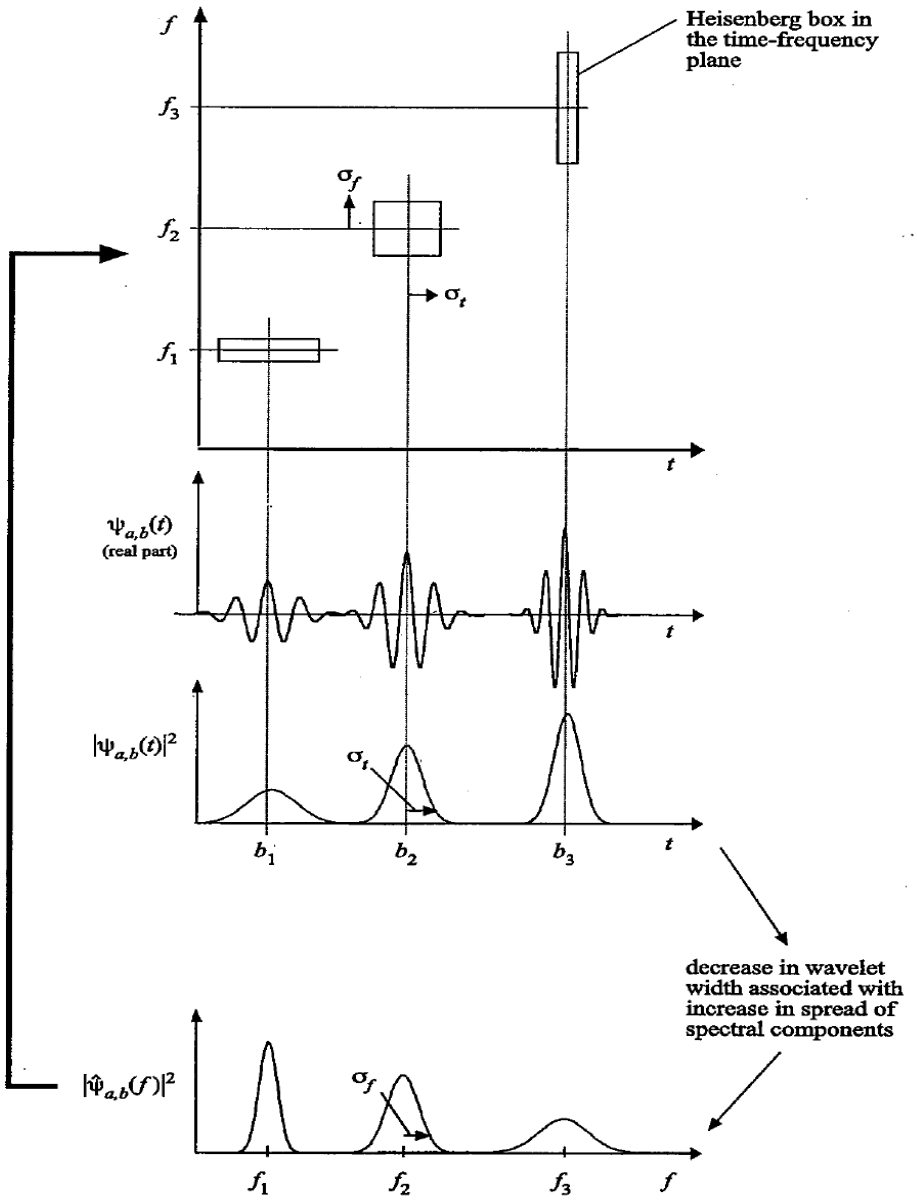

Figure 3.5: *Three Heisenberg boxes (top) associated with three Morlet mother wavelets with differing dilation values (middle), and their associated frequency spectra (bottom). Note how a more compact waveform in the time domain is associated with a broader spectrum in the frequency domain, and how the Heisenberg box reflects this behavior (Addison 2002).*

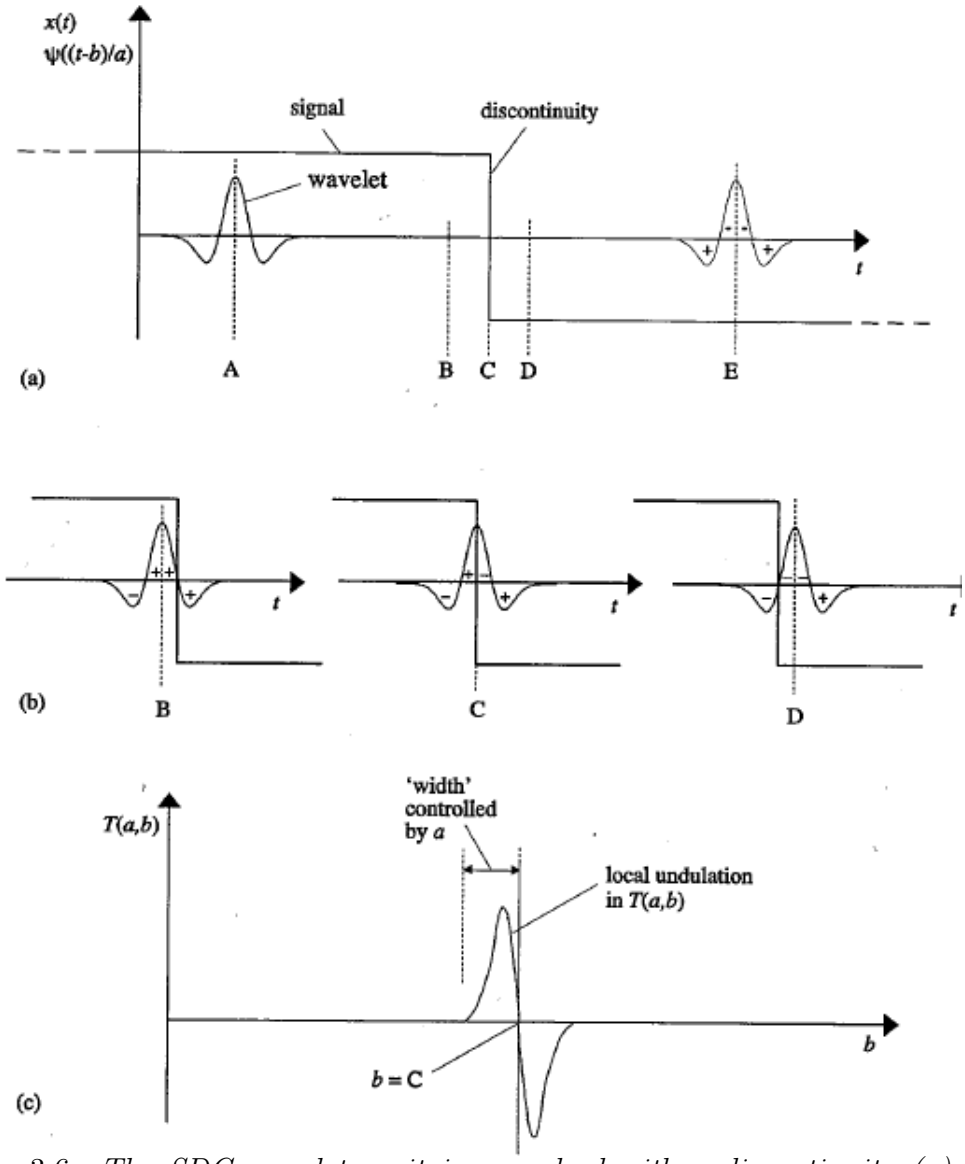

Figure 3.6: *The SDG wavelet as it is convolved with a discontinuity (a). As the wavelet approaches the discontinuity (b,B), the wavelet coefficient is mostly positive due to the positive correlation between the wavelet and the signal. At the discontinuity, the wavelet coefficient is equal to 0 (b,C). Shortly after the discontinuity, the wavelet coefficient is negative. A trace of the wavelet coefficient as the wavelet passes over the discontinuity is shown in (c). (Addison 2002)*

with coherent structures (Thomas and Foken 2007a) while the Morlet wavelet is localized in the frequency domain and is thus more suited to extract the spectral peaks associated with coherent structures (Thomas and Foken 2005). Due to its localization in time, the SDG mother wavelet has been repeatedly shown to be the best suited mother wavelet to detect the sharp jump in the perturbation temperature time series (Collineau and Brunet 1993) (Feigenwinter and Vogt 2005), which Thomas and Foken (2007a) associate with the passing of a micro-front Mahrt (1991). Fig. 3.6 illustrates how the SDG mother wavelet is able to detect the sharp jump associated with coherent structures.

Recently, Barthlott et al. (2007) successfully used the SDG wavelet to isolate coherent structures from small scale turbulence. Barthlott et al. (2007) found that zero crossings in the time series of the SDG wavelet coefficients along the scale associated with the peak in the wavelet power spectrum were a good detector of coherent structures within the canopy layer flow (Fig. 3.7).

The first step in the detection of coherent structures is to linearly detrend the time series; while Barthlott et al. (2007) used a temperature time series, any time series with ramp-like features (sharp jumps) can be used. Removing any linear trend in the time series is crucial as this particular detection method relies on the identification of peaks in the global wavelet spectrum – peaks that can be masked due to large scale trends in the time series.

The wavelet transform of the time series is computed in the second step using the SDG wavelet family. The convolution in the wavelet transform (Eq. 3.5) is implemented as a multiplication in the Fourier domain using Fast Fourier

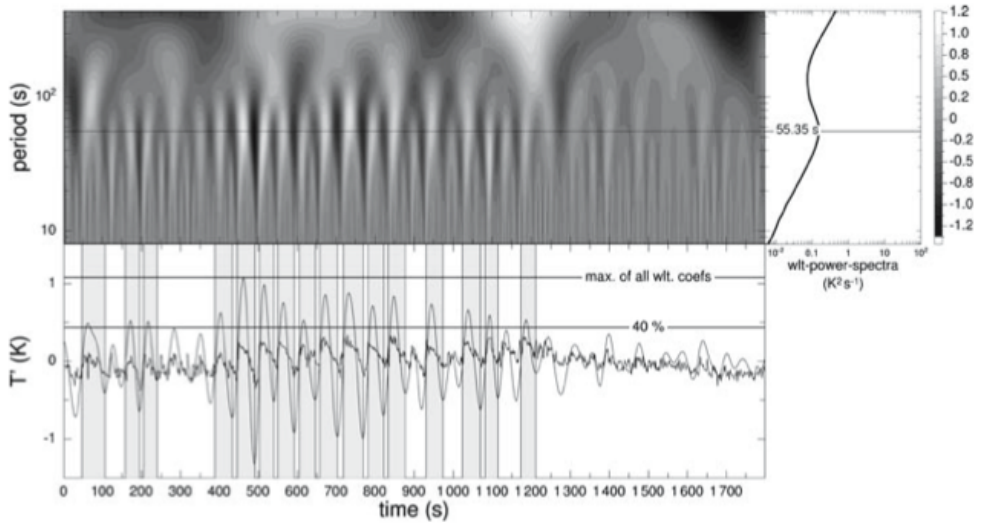

Figure 3.7: *Extraction of coherent structures (shaded periods, bottom) in stable conditions from the time series of turbulent fluctuations in temperature (dark, high frequency line, bottom) through the use of the zero crossings of the time series of wavelet coefficients (dark, smooth line, bottom) along the period associated with the peak in the wavelet power spectrum, which is shown in the top right of the figure (Barthlott et al. 2007).*

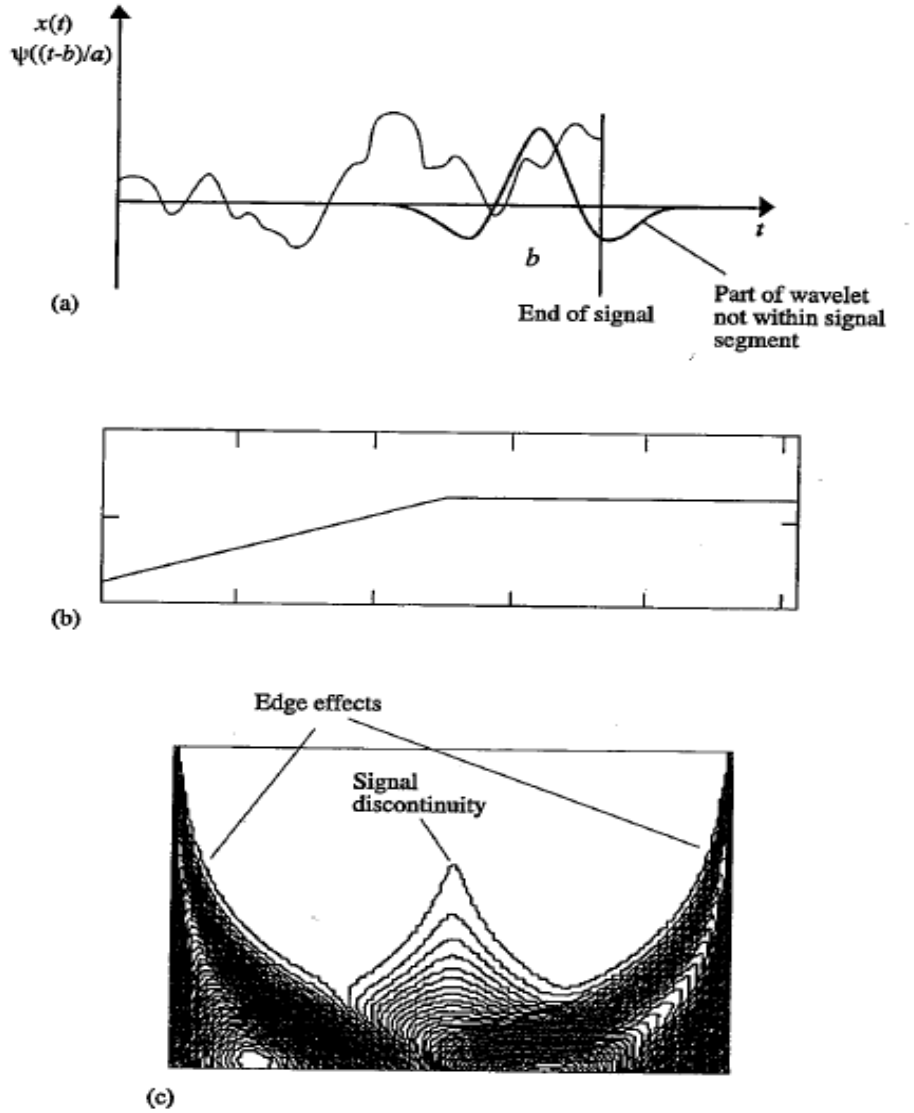

Figure 3.8: *Demonstration of the COI. The wavelet begins to extend past the signal as scale increases (a). This is handled by wrapping in the Fourier spectrum during the FFT. The sharp change in the signal at the ends of the time series can cause so call edge effects. An example signal with a discontinuity (b) and its wavelet scalogram (c) showing the impact of the COI. Note that although it is not explicit, the scalogram in (c) is plotted using a log scale on the y-axis, so the COI shows up as a curve. (Addison 2002)*

Transforms (FFTs) of the detrended time series and the SDG wavelet (Eq. 3.8). However, edge effects due to the use of a finite time series begin to play a role at larger scales, as the size of the wavelet can easily extend past the length of the time series and therefore pose an issue for estimating the peak in the global wavelet spectrum. This negative effect is known as the cone of influence (COI) and can be seen in Fig. 3.8. Although the edge effects are the same as those encountered in traditional Fourier Analysis (which can be countered by windowing the time series), the scales at which they become a problem are typically larger than those associated with coherent structures.

The third step is the calculation of the global wavelet spectrum (Eq. 3.10). The peaks in the global wavelet spectrum are then identified. If multiple peaks are detected, the peak at the smallest scale is used. The time series of the wavelet coefficients at the scale that coincides with the peak in the global wavelet spectrum is then used to determine the locations in time where coherent structures are dominant. If the temperature time series is analyzed, as is the case in the Barthlott et al. (2007) study, characteristics of the wavelet coefficient time series (which determine the present of coherent structures) change depending on stability. For stable conditions, each zero crossing in the wavelet coefficient time series indicates the beginning of a ramp-like structure (see Fig. 3.6 for details on why the zero crossing is significant for the SDG mother wavelet). If the magnitude of the next local minimia is greater than 40% (Barthlott et al. 2007) of the global maxima, the event is deemed a significant coherent structure event. The local minima in the wavelet coefficient time series following the zero crossing for

a significant coherent structure event marks the end of the ramp-like structure The markers for the beginning and end of a significant coherent structure event are reversed in unstable conditions (i.e. the zero crossing represents the end of a ramp-like structure, and the preceding local maxima marks the beginning). In a general sense, ramps in stable conditions can be called "ramp down events", and ramps in stable conditions can be called "ramp up" events.

The DNS used in this study did not include thermal effects and stability effects are not considered. However, based on the conditional cross sections in Chapter 2, it is expected that the transition from non-interactive periods to periods of CS-UCL periods would be marked by a change in $w\prime$ from negative values to positive values; values would generally be positive throughout the presence of the CS, before switching back to negative values once the CS move away from the observation point. Therefore, the life cycle of a CS from the point of view of a stationary observation location would be classified as a "ramp down" event, and the ramp-down characteristics are used to delineate the beginning and end of CS-CSL interaction periods.

3.1.2.2 Wavelet analysis of simulated time series

In this section, the wavelet analysis technique is assessed in a similar manor as the quadrant-hole method in the previous section. Again, simulated time series of w are obtained from grid points at the same height ($z = 1.5h$). Perturbation values of w are calculated by removing the mean value w; the mean value is computed over the entire length of the simulated time series. Next, a wavelet transform

using the Mexican Hat mother wavelet is applied to the w' time series. Following the method employed by Barthlott et al. (2007), the peak in the wavelet power spectrum is found and the wavelet coefficient time series at the peak period is examined. The maximum wavelet coefficient computed from the wavelet coefficient time series is found, and CS-UCL periods are found using the wavelet coefficient time series zero-crossings and three "coherent structure thresholds": 20%, 40%, and 60%. See Fig. 3.7 for a visual depiction of this process. If a ramp-like structure, as identified by the wavelet method, is found overlapping with a window for which the LMR_i based method detected CS-UCL interactions, the window is marked as a method detected CS-UCL interaction period. The wavelet detected CS-UCL periods are compared to the actual CS-UCL interaction periods (based on LMR_i), similar to comparisons used in the previous section.

Conditional cross sections created using wavelet detected interaction periods are compared to the conditional cross sections created by using the LMR_i based classification scheme of Chapter 2. As shown in Fig. 3.9, the conditional cross section computed using actual LMR periods (Fig. 3.9a) appears much different than all of conditional cross section created using the wavelet analysis method with coherent structure thresholds (CSTs) of 0.2 (Fig. 3.9b), 0.4 (Fig. 3.9c), and 0.6 (Fig. 3.9d). For all CST values presented in Fig. 3.2, the perturbation flow above the buildings does not represent a clear case of a low momentum region, and for CST values of 0.2 and 0.6, the flow in the canyon between $x = 3h$ and $x = 3.5h$ is completely opposite of that which is found in the actual LMR cross section. This is opposite of that which is found in the actual LMR cross section.

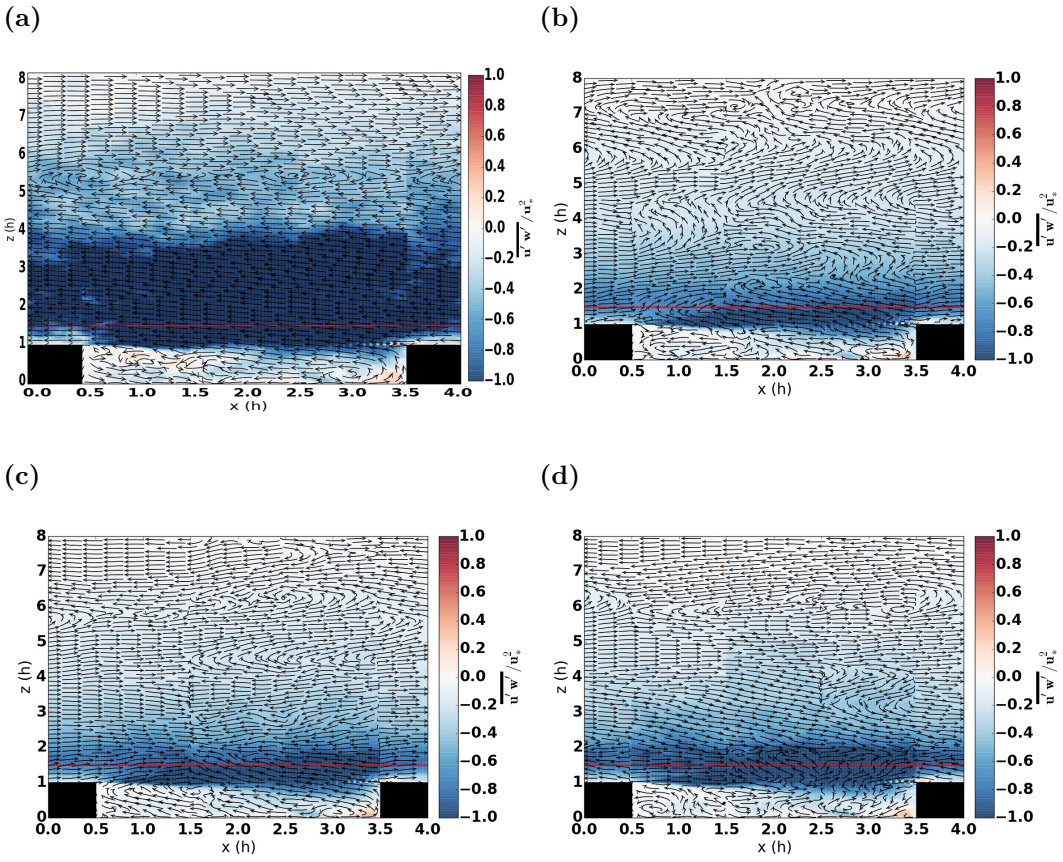

Figure 3.9: *CS-UCL interaction conditional cross section (a) compared to the conditional cross sections using wavelet analysis with a wavelet threshold value of 0.2 (b), 0.4 (c), and 0.6 (d).*

Table 3.5 breaks down the detection ability of the wavelet analysis method. Clearly the total number of detected periods is too large - an order of magnitude larger than the actual number of CS-UCL Interaction Periods. However, the wavelet analysis successfully detects most of the CS-UCL interaction periods. It is clear that the lower CST values do better at maximizing the number of successful detection periods, but unfortunately the lower CST values result in a larger number of false positives.

As was the case with the quadrant analysis method, the wavelet analysis method over estimates the fractional flux due to CS-UCL interactions, which is attributed to the false positive periods (Table 3.6). Without modification, the wavelet analysis method does a poor job of assessing the impact of CS-UCL interactions.

As with the quadrant analysis detection method, imposing the restriction that detected periods are only considered if they are made up of predominantly ejection motions improves the wavelet analysis detection method. The quadrant number used to determine if a detected period is predominantly an ejection event is computed by finding which quadrant contains the center of the joint pdf of $u\prime w\prime$ using samples of u' and w' during the detected period. The improvement is due to a substantial reduction in the number of false positives by an order of magnitude ($\approx$ 20 to $\approx$ 2) (Table 3.7), with only a very small increase in the number of undetected interactions (limited to the $h \times h$ block directly over a roughness element, and the $h \times h$ block directly downstream from a roughness element).

Table 3.5: The average total number of wavelet analysis detected interaction periods (by CS threshold values - 0.2, 0.4, and 0.6), and a break down by, on average, how many periods were successfully detected, how many were false positives, and how many interaction periods were missed by the wavelet analysis detection method, as a function of spatial proximity to a roughness element. Also included is the number of actual CS-UCL interaction periods as determined using the $\overline{LMR_i}$ classification scheme from Chapter 2.

	Midpoint	Upstream	Building	Downstream
Average Number of CS-UCL Interaction Periods				
CS-UCL Interaction Periods	6.0	5.5	4.2	3.8
Total Number of Detected Periods	(23.5, 14.8, 6.8)	(21.0, 13.5, 8.2)	(23.5, 15.8, 8.5)	(21.8, 14.0, 8.0)
Successfully Detected	(5.0, 3.8, 1.5)	(4.8, 3.8, 2.2)	(3.2, 2.0, 1.5)	(3.5, 2.2, 1.2)
Missed CS-UCL Interactions	(1.0, 2.2, 4.5)	(0.8, 1.8, 3.2)	(1.0, 2.2, 2.8)	(0.2, 1.5, 2.5)
False Positives	(18.5, 11.0, 5.2)	(16.2, 9.8, 6.0)	(20.2, 13.8, 7.0)	(18.2, 11.8, 6.8)

Table 3.6: Percentages of detection, fractional flux values, and transport efficiencies, broken down by successful, missed, and false positive detections as determined by using the wavelet analysis method with CS threshold values of 0.2, 0.4, and 0.6.

	Midpoint	Upstream	Building	Downstream
Percentages of Detection (%)				
Successfully Detected	(83.0, 64.6, 28.0)	(77.1, 56.2, 35.7)	(72.5, 47.5, 37.5)	(93.8, 55.4, 30.8)
Not Detected	(17.0, 35.4, 72.0)	(22.9, 43.8, 64.3)	(27.5, 52.5, 62.5)	(6.2, 44.6, 69.2)
Method False Detection	(78.8, 73.0, 75.4)	(79.6, 77.4, 74.3)	(86.2, 87.8, 82.6)	(82.9, 80.5, 83.3)
Fraction of total kinematic momentum flux				
CS-UCL Interaction	0.25	0.31	0.16	0.17
Method Detected	(0.77, 0.54, 0.31)	(0.86, 0.65, 0.45)	(0.87, 0.63, 0.37)	(0.86, 0.56, 0.43)
Method Missed	(0.03, 0.05, 0.14)	(0.09, 0.12, 0.16)	(0.03, 0.05, 0.08)	(0.07, 0.05, 0.09)
Method False Detection	(0.54, 0.33, 0.2)	(0.6, 0.43, 0.31)	(0.73, 0.53, 0.29)	(0.71, 0.45, 0.35)
Transport Efficiency				
CS-UCL Interaction	1.41	1.49	1.14	1.16
Method Detected	(1.06, 1.19, 1.5)	(1.09, 1.3, 1.46)	(1.08, 1.18, 1.27)	(1.05, 1.07, 1.4)
Method Missed	(0.67, 0.8, 1.09)	(1.15, 1.07, 1.26)	(0.73, 0.76, 0.71)	(1.66, 1.02, 0.97)
Method False Detection	(0.94, 1.0, 1.23)	(0.96, 1.16, 1.29)	(1.06, 1.12, 1.2)	(1.06, 1.09, 1.48)

Table 3.7: Same as Table 3.5, but for the modified wavelet analysis detection method.

	Midpoint	Upstream	Building	Downstream
Average Number of CS-UCL Detection Periods				
CS-UCL Interaction Periods	6.0	5.5	4.2	3.8
Total Number of Detected Periods	(7.5, 5.8, 2.5)	(6.8, 5.0, 2.8)	(4.8, 3.5, 2.2)	(5.8, 3.2, 2.0)
Successfully Detected	(5.0, 3.8, 1.5)	(4.8, 3.8, 2.2)	(3.0, 2.0, 1.5)	(3.0, 1.8, 1.0)
Missed CS-UCL Interactions	(1.0, 2.2, 4.5)	(0.8, 1.8, 3.2)	(1.2, 2.2, 2.8)	(0.8, 2.0, 2.8)
False Positives	(2.5, 2.0, 1.0)	(2.0, 1.2, 0.5)	(1.8, 1.5, 0.8)	(2.8, 1.5, 1.0)

The reduction in the number of false positives has remarkable impact on the fractional flux attributed to detected interactions (which are very close to the actual CS-UCL fractional flux). As the case with the modified quadrant-hole method, the ability of the modified wavelet method to capture the fractional flux attributed to CS-UCL interactions is best for the $h \times h$ block immediately upstream from the roughness element. However, the method also performs well for the $h \times h$ block in the middle of the canyon, where the percentage of successfully detected CS-UCL interaction periods is the highest, and the Transport Efficiency closely matches the actual TE of CS-UCL interaction periods.

An improvement is also seen if the conditional cross section of the modified wavelet analysis method is considered (Fig. 3.10). A clear LMR flow pattern in the perturbation vectors can now be seen in the conditional cross sections, the in-canyon flow pattern is a much better match. As is the case with the modified quadrant-hole method, the thickness of the normalized kinematic momentum flux layer is not well represented in the cross section, potentially due to the number of false positives still attributed to the modified wavelet analysis detection method.

Unlike the quadrant hole detection method, the fractional fluxes associated with Q4 (sweep) motions do not make up the difference between the fractional fluxes associated with Q2 (ejection) events and the fractional fluxes determined using the unmodified wavelet analysis technique.

Overall, the modified wavelet analysis method shows a dramatic improvement over the standard wavelet analysis method, and is tested at full-scale in Chapter 4. Again, as was the case with the modified quadrant-hole method, special care

Table 3.8: Same as Table 3.6, but for the modified wavelet analysis detection method.

	Midpoint	Upstream	Building	Downstream
Percentages of Detection				
Successfully Detected	(83.0, 64.6, 28.0)	(77.1, 56.2, 35.7)	(67.5, 47.5, 37.5)	(81.2, 42.9, 24.6)
Not Detected	(17.0, 35.4, 72.0)	(22.9, 43.8, 64.3)	(32.5, 52.5, 62.5)	(18.8, 57.1, 75.4)
Method False Detection	(26.1, 25.8, 33.3)	(27.9, 36.1, 11.2)	(32.1, 35.0, 22.9)	(49.4, 50.8, 37.5)
Fraction of total kinematic momentum flux				
CS-UCL Interaction	0.25	0.31	0.16	0.17
Method Detected	(0.3, 0.25, 0.14)	(0.3, 0.24, 0.21)	(0.2, 0.17, 0.12)	(0.26, 0.18, 0.18)
Method Missed	(0.03, 0.05, 0.14)	(0.09, 0.12, 0.16)	(0.03, 0.05, 0.08)	(0.0, 0.04, 0.07)
Method False Detection	(0.09, 0.06, 0.06)	(0.06, 0.04, 0.02)	(0.09, 0.08, 0.07)	(0.09, 0.05, 0.06)
Transport Efficiency				
CS-UCL Interaction	1.41	1.49	1.14	1.16
Method Detected	(1.5, 1.58, 1.93)	(1.27, 1.29, 1.7)	(1.35, 1.6, 1.58)	(1.26, 1.47, 1.66)
Method Missed	(0.67, 0.8, 1.09)	(1.15, 1.07, 1.26)	(0.69, 0.76, 0.71)	(0.03, 0.6, 0.75)
Method False Detection	(1.01, 0.89, 1.15)	(0.4, 0.45, 0.72)	(1.17, 1.25, 1.44)	(1.02, 0.88, 0.98)

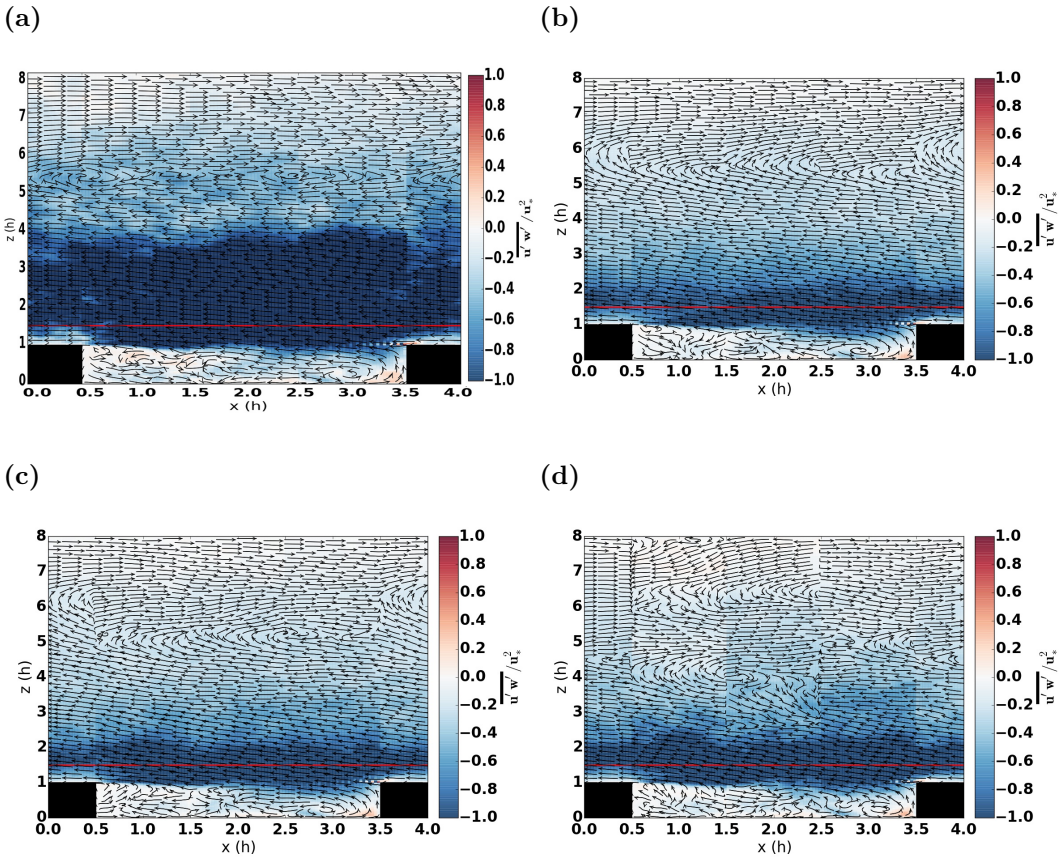

Figure 3.10: *CS-UCL interaction conditional cross section (a) compared to the conditional cross sections using wavelet analysis limited to ejection events with a wavelet threshold value of 0.2 (b), 0.4 (c), and 0.6 (d).*

should be taken that the wavelet detection method is not applied in locations directly downstream from roughness elements, as these results suggest that these regions are dominated by wake effects.

3.1.3 Summary and expectations at full-scale

In summary, use of the quadrant hole and wavelet analysis methods in the simulated time series dataset reveals that these techniques, when unmodified, poorly capture the impact of LMR-driven CS-UCL interactions. There is a remarkable improvement in both methods' ability to capture these impacts when the conceptual model of Coceal et al. (2007a) is taken into account and a restriction is placed on the methods such that only time periods where ejections are dominant are used. The fraction flux associated with the unmodified quadrant analysis method appears to be be the summation of the sweep and ejection events detected by the technique, although only the ejection (Q2) events appear to represent CS-UCL interactions; this is not the case with the wavelet analysis method. This would suggest that identification of the CS-UCL events is better represented in "strong" events (large $u'w'$ values) rather than ramp-like shapes in the time series. The modified quadrant-hole method with a small hole size (0.25) and the modified wavelet analysis method with a small CST (0.2) appear to be the best at capturing the impact of CS-UCL interaction periods.

Both modified methods perform decently directly over the roughness elements, although they perform best over the $h \times h$ block directly upstream of a roughness element, and over the $h \times h$ block directly in-between roughness elements. Both

modified methods perform poorly one $h \times h$ block downstream of a roughness element, and similar locations in the full-scale analysis should be avoided.

When applied to full-scale data obtained in favorable locations with respect to proximity to roughness elements (Chapter 4), it is expected that the modified methods will have smaller fractional flux values and larger transport Efficiency values when compared to the standard techniques. It is also expected that the characteristic profiles from Chapter 2 will be evident in the average profiles from the full-scale dataset using the periods detected by the modified methods.

Chapter 4

Coherent structure / canopy shear layer interactions at full-scale

4.1 Introduction

In Chapter 2, a framework for identifying CS-UCL interaction types in the DNS dataset was created and is summarized in Table 2.1. The framework was then used to study LMR-driven CS-UCL interactions within the DNS dataset, and very distinguished flow patterns emerged based on whether or not CS-UCL interactions were occurring. In addition, characteristic profiles were created for the two CS-UCL interaction types.

In Chapter 3, time series analysis techniques often applied in observations studies were applied to DNS time series data from individual grid points within the model. It was found that the time series analysis techniques poorly captured LMR-driven CS-UCL interactions. However, the ability of these techniques to capture CS-UCL interactions greatly increased when an additional criterion (limit to ejection dominated interactions only) was applied. Fractional fluxes and transport efficiencies (TEs) for the techniques, as well as the corresponding modified techniques, were computed and notable differences resulted (see Chapter 3.1.3 for a summary).

Based on the results of Chapters 2 and 3, the ability to study LMR-driven CS-UCL interactions at full-scale is now investigated. The techniques (including modified versions) from Chapter 3 are applied to observational data. This section focuses on conditional cross sections to identify flow patterns, fractional fluxes and TE values, and profiles of turbulence quantities. Each of these focus areas have been explored in the DNS dataset (specifically in Chapter 3), and expectations are set based on those results.

4.2 Cross Center site description

The Cross Center site is located on south side of the campus of the University of Oklahoma in Norman, Oklahoma (Fig. 4.1). The site is located 4.5 km to the SSE of the Norman Oklahoma Mesonet Site, NRMN (which is also used in this study). The site is generally situated on the south side of the City of Norman. Because of this location, northerly flows should be fully developed urban boundary layer flows, while southerly flows, with their shorter urban fetch, may not be fully developed.

A closer examination of the site reveals that it is primary made up of four east-west oriented (although one north-south oriented building exists on the far east side), three story dormitory building that are now used as office space. The area to the north of the site is a mix of campus building and residential areas. The area to the south of the site is a mix of open fields, parking lots, and less densely packed buildings (Fig. 4.2).

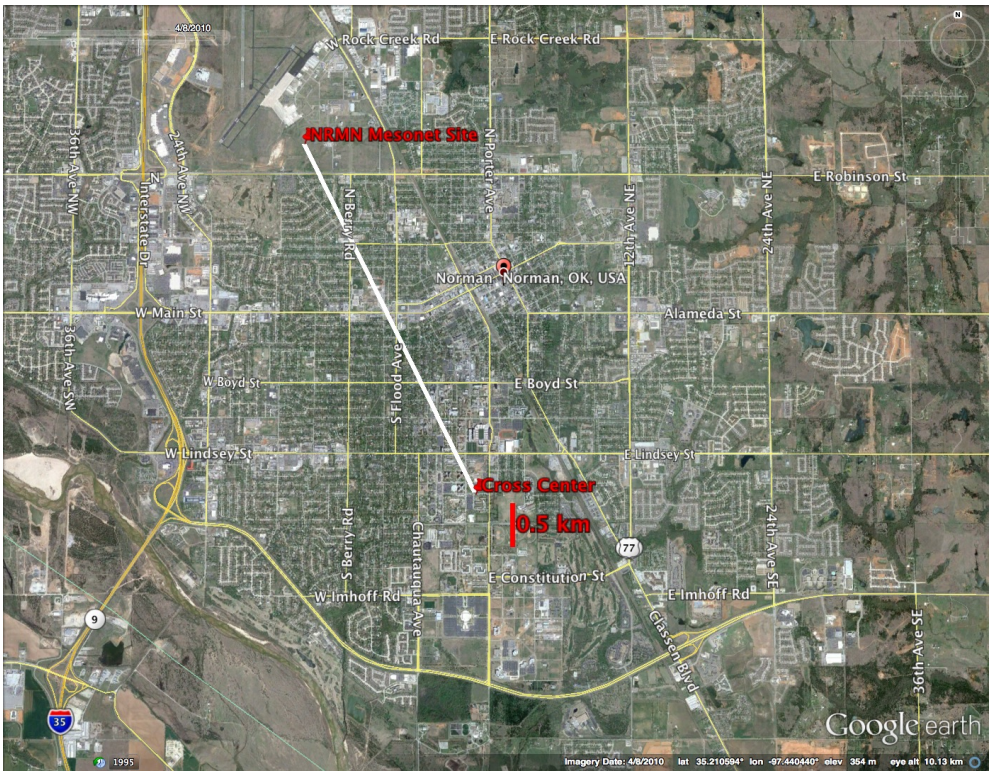

Figure 4.1: *Google map showing location of cross center and, 4.5 km to the NNW (white line), the NRMN mesonet site.*

Figure 4.2: *Google map showing location of cross center with 0.5 km scale.*

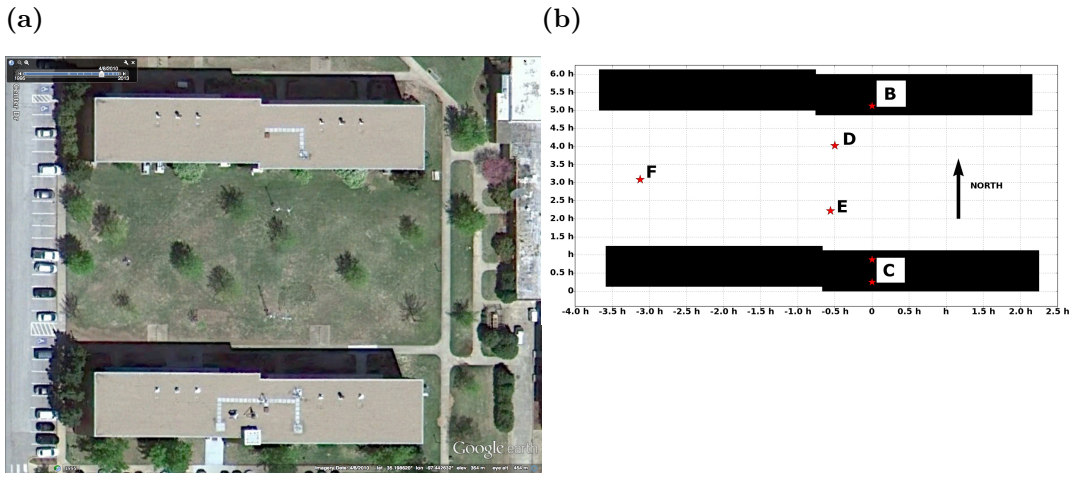

Figure 4.3: *Google Map zoomed in over the cross center (a) with a side-by-side horizontal layout map of the Cross Center observation site locations (b).*

Five observational towers (B - F) were placed on site as part of the Innovative Laboratory for Research and Education in Urban Meteorology (ILREUM) project (NSF Grant #ATM054788) (see Fig. 4.3). An aerial photograph and horizontal site layout are shown in Fig. 4.3. The site was in operation from July 2009 through August 2010.

Each tower, with the exception of tower F, was equipped with multiple three-axis ultrasonic anemometers. Tower F only had one ultrasonic anemometer. A total of 13 sonic anemometers were deployed at the Cross Center site.

Each sonic anemometer output samples with a frequency of 10Hz. Figs. 4.3 and 4.4 show the vertical and horizontal (north/south) distribution of sonic anemometers at the cross center site. Sonics D2, D3, E3, and E4 were Campbell Scientific CSAT-3 anemometers; the remaining sonics were R.M. Young 81000 sonic anemometers. The CSAT-3 sonics have a manufacturer specified accuracy

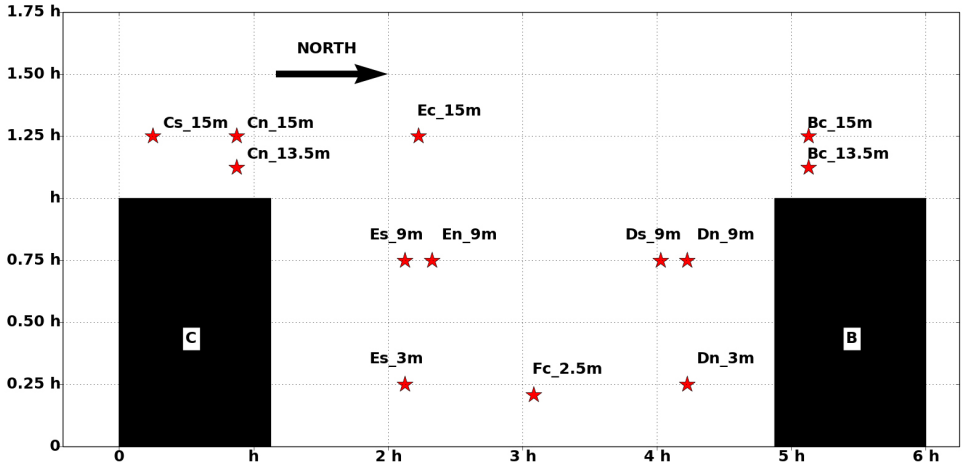

Figure 4.4: *Distribution of the sonic anemometers along a north-south oriented vertical cross section.*

of +/- 0.08 m/s for the horizontal components of wind, and +/- 0.04 m/s for the vertical, each component with a 0.001 m/s resolution. The 81000 sonics have a manufacturer specified accuracy of +/- 3% +/- 0.05 m/s for all three component, each with a 0.01 m/s resolution. Both sonic anemometer types have an accuracy of around 2 ^oC when sampling the sonic temperature.

Further information regarding the site layout and instrumentation can be found in Klein and Galvez (2014).

4.3 General data processing

Data are selected in two passes. First, data are selected based on hourly averaged conditions at the Norman Mesonet Site (NRMN), located 4.5 km to the NNW of the Cross Center site. North cases were chosen based on hourly averages of wind direction between +/- 5^0 north; southerly cases were chosen similarly based on

+/- 5^0 of south. Both north and south cases were further subjected to a screening based on stability at the NRMN mesonet using the Gradient Richardson Number,

$$Ri = \frac{g\Delta z_u^2 \left[\frac{T_{9m} - T_{1.5m}}{\Delta z_T} + \Gamma_d\right]}{T_{1.5}\left(u_{10m} - u_{2m}\right)^2}, \tag{4.1}$$

where g is the acceleration due to gravity, Γ_d is the dry adiabatic lapse rate ($\approx 10K/km$), u is the wind speed at 10m or 2m, T is the temperature at 9m or 1.5m, and Δz_u / Δz_T is the distance between the wind speed or temperature sample levels; only cases with near neutral conditions were used ($-0.1 \leq Ri < 0.1$). Further, Cross Center data, which were stored in 1 hour blocks, are only used in cases where complete data files existed for all five towers. Finally, only cases where the horizontal wind speed at the Cross Center is greater than 1 m/s are used; for northerly cases, this is tested using the 15m sonic on Cross Center B, and for southerly cases the northern most 15m sonic on Cross Center C is used.

From the criteria above, twenty seven (27) one-hour cases were used for northerly flow and thirty two (32) one-hour cases were used for southerly flow. Northerly flow cases range in date from February 22nd through March 20th with a majority of times occurring between 10 am and 4 pm local time; southerly flow cases were range in date from March 7th through July 9th with times occurring at nearly all hours throughout the day.

Sonic data were transformed from instrument coordinates, where u_i, v_i, and w_i are east-west, north-south, up-down (parallel to gravity) velocity components, into canyon relative coordinates, where u_c, v_c, and w_c are cross canyon, along

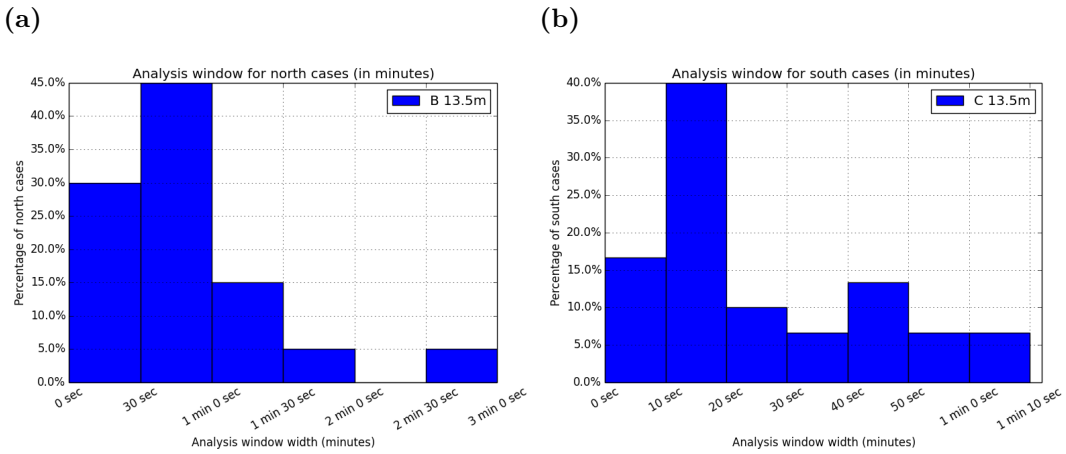

Figure 4.5: *Distribution of analysis window times for north (a) and south (b) cases.*

canyon, and perpendicular to the canyon components of velocity. For this transformation, w_i and w_c are the same, as the sonic anemometers were leveled upon installation and should be essentially perpendicular to the canyon.The horizontal velocity components are rotated according to the general 2D rotation transformation,

$$\begin{bmatrix} u_c \\ v_c \end{bmatrix} = \begin{bmatrix} \cos\theta & -\sin\theta \\ \sin\theta & \cos\theta \end{bmatrix} \begin{bmatrix} u_i \\ v_i \end{bmatrix}, \tag{4.2}$$

where θ is $\pi/2$ for south cases, and $3\pi/2$ for north cases. For simplicity, the subscript on the canyon components is dropped, and it is assumed that the analysis is done in the canyon coordinate system.

When analyzing the DNS output, a time window of 10τ was chosen based on the expected statistical behavior of the skewness and kurtosis of $\overline{LMR_i}$ (see Chapter 2.3); τ, the eddy turnover time, is defined as

$$\tau = \frac{h}{u_\tau}, \tag{4.3}$$

where h is the height of the roughness element, and u_τ is the friction velocity at building height. To estimate an appropriate value of τ for the cross center site, a value of 12 m was used for h (i.e. the building height) and the hourly value of u_* at 13.5 m AGL (1.5 m above the roof) of tower C (south cases) and B (north cases) was used to estimate u_τ. A distribution of 10τ values for north and south cases at the Cross Center is shown in Figs. 4.5a and 4.5b, respectively. The analysis window, 10τ for north cases ranges from values between 0 - 30 seconds through values between 2.5 minutes - 3 minutes; for south cases, the analysis window ranges from values between 0 and 30 seconds through values between 1 and 1.5 minutes. It is clear from Fig. 4.5 that a single analysis window cannot be used for the cross center site. It would also be inappropriate for a single value to be used for either north or south cases. Therefore, each hourly case was analyzed by dividing the time series into N windows,

$$N = \left\lfloor \frac{t_{TS}}{10\tau} \right\rfloor, \tag{4.4}$$

where t_{TS} is the length of the time series being analyzed (in this case, one-hour), with each window having a time width of $\Delta t_w = 10\tau$. Note that reference values

from towers B or C (based on wind direction) that are used to normalize various statistical quantities (which are computed over the Δt_w windows) are obtained using the entire 1 hour window for a given case. This is based on the work of Klein and Galvez (2014), who utilized the same dataset.

As an example, suppose a single southerly flow case with $\Delta t_w = 5\ minutes$ is analyzed. As part of the analysis, normalized TKE (TKE/u_*^2) is computed. First, perturbation velocities are computed over the hour long record. Second, TKE is computed for each Δt_w window. Third, each TKE value is normalized by u, which is computed using the entire hour record from the 15m sonic anemometer on Tower C (north).

4.4 Basic north / south flows

Average flow cross sections for both north and south cases are created to assess general flow patterns (Fig. 4.6). For both north and south cases, the mean flow pattern is characterized by two features: slightly descending flow on the rooftop the upstream building (Cross B for north cases, Cross C for south cases), and a rotor between the two buildings (prograde in the sense of the above canyon flow). This flow pattern is similar to the wake interference or skimming regimes described by Oke (1989), although the dimensions of the cross center site would predict the flow to be in the isolated roughness flow regime ($\frac{L}{H} \approx 5.5$, $\frac{H}{W} \approx 0.2$, where L is the length of the building, H is the height of the building, and W is the width between two building) (see Fig. 1.6). These cross sections are very

(a)

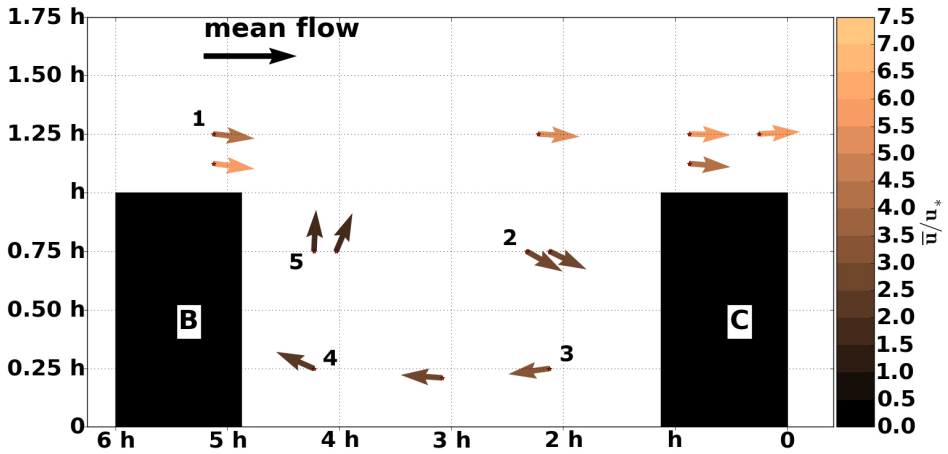

(b)

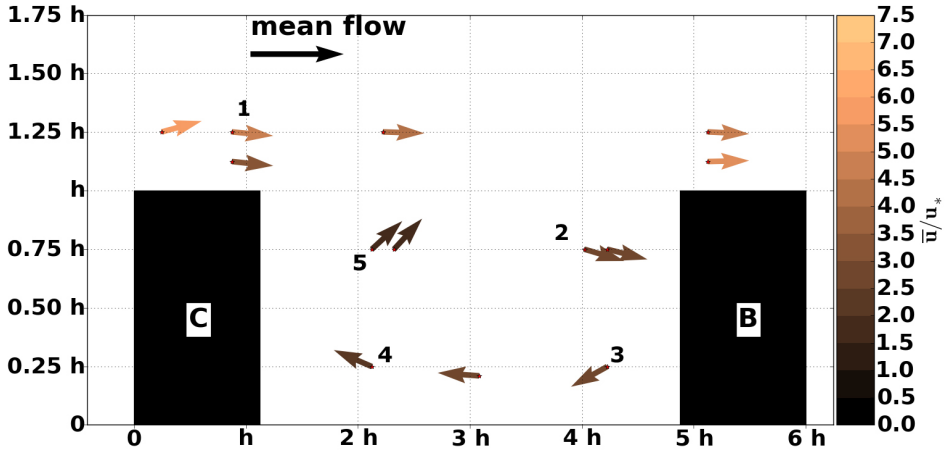

Figure 4.6: *Mean flow cross sections for north (a) and south (b) cases. The numbers represent position along the in-canyon circulation. Note these change based on wind direction in an attempt to minimize tower structure influence.*

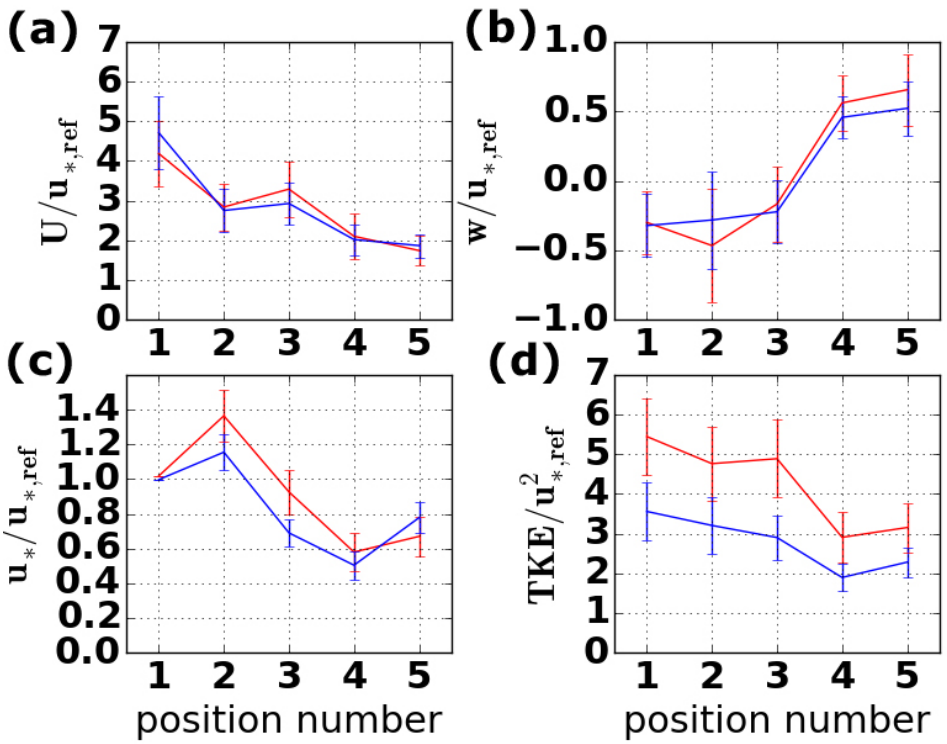

Figure 4.7: *Analysis of normalized mean: horizontal wind speed (a), vertical component of velocity (b), friction velocity (c), and turbulence kinetic energy (d) for north (blue) and south (red) cases. Error bars indicate the spread of the data, using the value of one standard deviation.*

similar to those found by Klein and Galvez (2014), even though the criteria used in this study are slightly different.

Figure 4.7 shows how basic turbulence quantities change following the flow from outside the canyon along the rotor inside the street canyon (see Fig. 4.6 for the location of the positions used). These results are similar to those found in Klein and Galvez (2014), and slight differences can be attributed to 1) a difference in coordinate system used, and 2) a difference in the way u_* is defined

(in this study, both along-canyon and cross-canyon components of the kinematic momentum flux are used to define u_*).

4.5 North cases

The quadrant analysis method and the wavelet analysis method (including the modified methods), as described in Chapter 3, are now applied to north flow cases. Each method is applied to the sonic anemometer at 15 m AGL (3.0 m above roof level) on building B; Based on the results from the DNS analysis (summarized in 3.1.3), a quadrant hole size of 0.25 and a coherent structure threshold of 0.2 are used used. Conditional cross sections, analysis of fractional flux and TE values, and characteristic profiles for north cases are presented in the following sections.

4.5.1 Quadrant analysis of full-scale data - north cases

Fig. 4.8 shows a comparison of conditionally averaged perturbation vectors (u', w') for four conditions (north cases): all north cases (Fig 4.8a), Quadrant Analysis detected cases (4.8b), Modified Quadrant Analysis (Q2, ejection) detected cases (4.8c), and Modified Quadrant Analysis (Q4, sweep) detected cases (4.8d).

The conditional cross sections for all north cases (Fig 4.8a) and Quadrant Analysis detected cases (4.8b) do not present easily identifiable flow patterns, and look nothing like the LMR-driven CS-UCL interaction periods or non-interaction periods from Chapter 2. However, the Modified Quadrant Analysis (Q2, ejection) detected cases (4.8c), and Modified Quadrant Analysis (Q4, sweep) detected cases (4.8d) clearly match the CS-UCL interaction (Fig. 2.9) and non-interaction (Fig. 2.8) periods, respectively.

The conditionally averaged cross section of the Modified Quadrant Analysis (Q2, ejection) detected cases (4.8c) is characterized by an in-canyon rotor, and

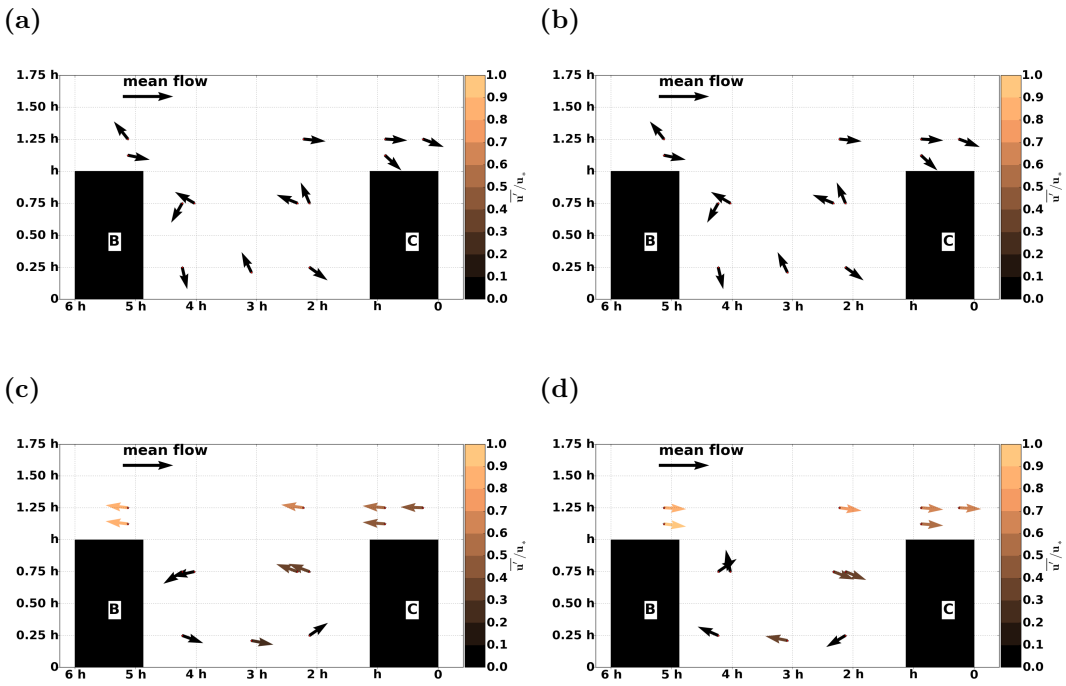

Figure 4.8: *North flow cases cross sections of mean perturbation flow for all cases (a), Quadrant Analysis detected cases (b), Quadrant Analysis detected cases restricted to Q2 events (c), and Quadrant Analysis detected cases restricted to Q4 events (d).*

above canyon perturbation vectors in the direction opposite of the mean flow. Note that the in-canyon rotor (Fig. 4.8c) is rotating opposite of that created by the mean flow (Fig. 4.6(b)).

In contrast, the conditionally averaged cross section of the Modified Quadrant Analysis (Q4, sweep) detected cases (4.8c) is characterized by an in-canyon rotor and above canyon perturbation vectors both in the same sense as the mean flow cross section (Fig. 4.6(a))

These results show that the modified quadrant method is able to separate motions consistent with what is expected by the LMR-driven interactions / non-interactions, as seen in the DNS dataset.

The average fractional fluxes and TEs for northerly cases using the Quadrant Analysis and Modified Quadrant Analysis (Q2, ejection) methods are shown in Fig. 4.9. Figs. 4.9a and 4.9c show the average fractional fluxes (top number) and TEs (bottom number) for Quadrant Analysis detected periods for $\overline{u'w'}$ and $\overline{w'T'}$, respectively. Figs. 4.9b and 4.9d show the same, except using periods detected by the Modified Quadrant Analysis (Q2, ejection) method.

In all cases, the fractional flux values are reduced when using the Modified Quadrant Analysis (Q2, ejection) method; this is consistent with the results from the DNS analysis (Table 3.4), and may be attributed to any false positives included in the analysis. For $\overline{u'w'}$, the TE values decrease, most of them below a value of 1, which is not consistent with the DNS analysis results. This would indicate that along-stream kinematic momentum transfer is less efficient than the overall transfer during the observation period. In contrast, five of the sonic

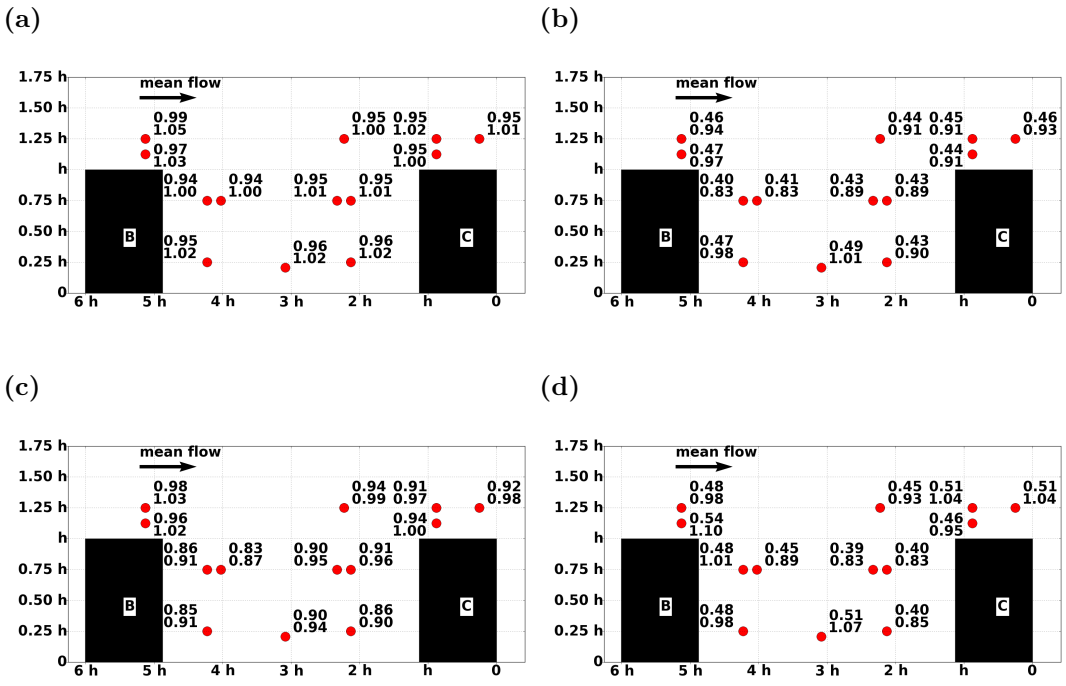

Figure 4.9: *North case cross sections of fractional fluxes (top number) and TEs (bottom number) for all quadrant detected events (a, c) and all quadrant detected events restricted to Q2 events (b, d) for* $\overline{u'w'}$ *(top row) and* $\overline{w'T'}$ *(bottom row).*

anemometers exhibit an increase in TEs for when using the modified method for $\overline{w'T'}$. Perhaps differences can be attributed to the lack of stability effects in the DNS dataset, or they might suggest that there is a difference in how heat and momentum are transported.

Profiles of $\overline{w'}$ are examined and compared with the characteristic markers from Chapter 2.4.2. It is critical to note that these characteristic markers were developed by only considering the presence/ non-presence of an LMR in the DNS dataset, that is, these markers are independent of observational detection techniques. Also note that characteristic markers for TKE and $\overline{u'w'}$ were also described in Chapter 2.4.2. However, most of the defining characteristics between the CS-UCL interaction / non-interaction periods for these turbulence parameters occur at heights above those sampled at the Cross Center site, and therefore will not be considered in this analysis.

For northerly cases, data from Tower D are compared to the markers found for one block downstream of a roughness element from the DNS analysis (Table 2.3), while Tower E is compared the markers found for one block upstream of a roughness element (Table 2.4). Data from towers B and C are compared to the markers found for the block directly over a roughness element (Table 2.6). Given that Tower F is offset horizontally from the rest of the towers, has only one vertical level, and is found near the edge of the building where corner rotor effects may dominate, it is not discussed.

A clear difference in the profiles is seen when comparing the Modified Quadrant methods; the modified quadrant-hole method (Q2, ejection) (Fig 4.10a)

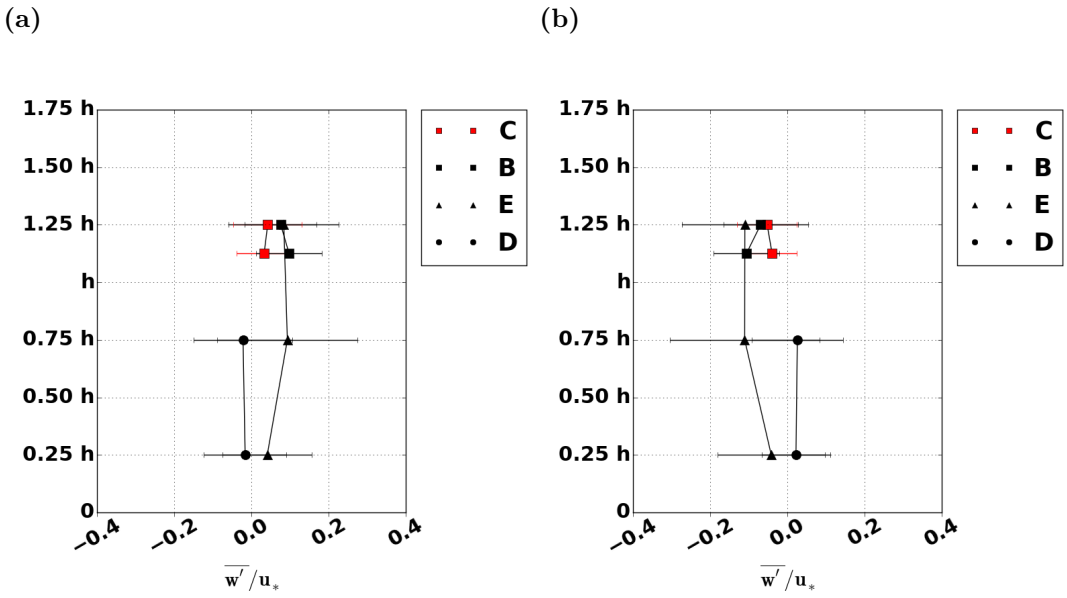

Figure 4.10: *North case profiles of $\overline{w'}$ for quadrant analysis detected cases restricted to Q2, ejection (a) and Q4, sweep (b) events.*

clearly exhibits the characteristics of CS-UCL interaction periods, whereas the modified quadrant-hole method (Q4, sweep) clearly exhibits the characteristics of non CU-UCL interaction periods.

A comparison of rotor following, normalized turbulence statistics shows that during CS-UCL interactions (Fig. 4.11) , horizontal wind speeds above the canyon are reduced (indicative of the LMR), the values of u_* are overall smaller and average vertical velocities are less negative near the downstream side of the canyon, when compared to non-interaction periods (Fig. 4.11). As was seen in Klein and Galvez (2014), reduced normalized TKE values at the rooftop level, as seen during CS-UCL interaction periods, tends to result in lower normalized TKE values inside the canyon (compare Fig. 4.11d with Fig. 4.11d), which indicates TKE is transported into the canyon by the mean flow.

While some differences are seen in the TEs when compared to the DNS analysis (which may be attributed to stability effects), all other comparisons between the full-scale analysis clearly show the flow patterns and characteristic markers found for LMR-driven CS-UCL interaction and non-interaction periods.

4.5.2 Wavelet analysis of full-scale data - north cases

Fig. 4.12 shows a comparison of conditionally averaged perturbation vectors (u', w') for four conditions (north cases): all north cases (Fig 4.12a), Wavelet Analysis detected cases (4.12b), Modified Wavelet Analysis (Q2, ejection) detected cases (4.12c), and Modified Wavelet Analysis (Q4, sweep) detected cases (4.12d).

The conditional cross sections for all north cases (Fig 4.12a) and Wavelet Analysis detected cases (4.12b) do not present clear flow patterns and look nothing like the LMR-driven CS-UCL interaction periods or non-interaction periods) from Chapter 2. However, the Modified Wavelet Analysis (Q2, ejection) detected cases (4.12c), and Modified Wavelet Analysis (Q4, sweep) detected cases (4.12d) clearly match the CS-UCL interaction (Fig. 2.9) and non-interaction (Fig. 2.8) periods, respectively. This is the same result as seen using the quadrant-hole method assessment in the previous section.

This would indicate that, in addition to the modified quadrant analysis method, the modified wavelet method is also able to capture motions consistent with what is expected by the LMR-driven interactions / non-interactions, as seen in the DNS dataset.

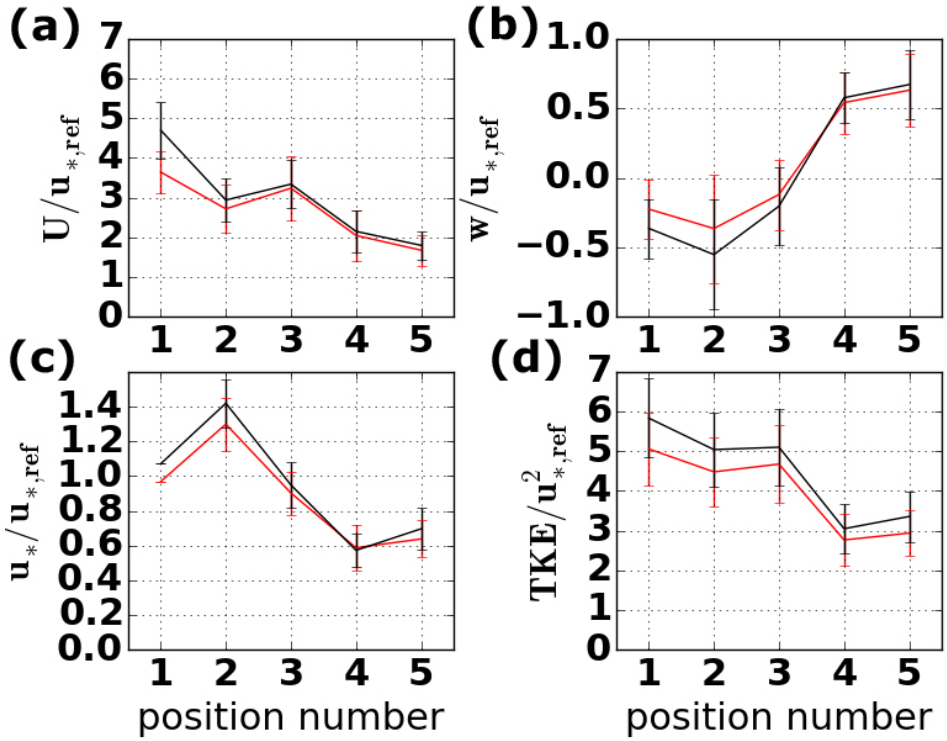

Figure 4.11: *Analysis of normalized mean horizontal wind speed (a), vertical component of velocity (b), friction velocity (c), and turbulence kinetic energy (d), along the path of the street canyon rotor for northerly flow during CS-UCL interaction periods as detected by the Modified Quadrant Analysis (Q2, ejection - Black) method and Modified Quadrant Analysis (Q4, sweep - Red). Error bars indicate the spread of the data, using the value of one standard deviation.*

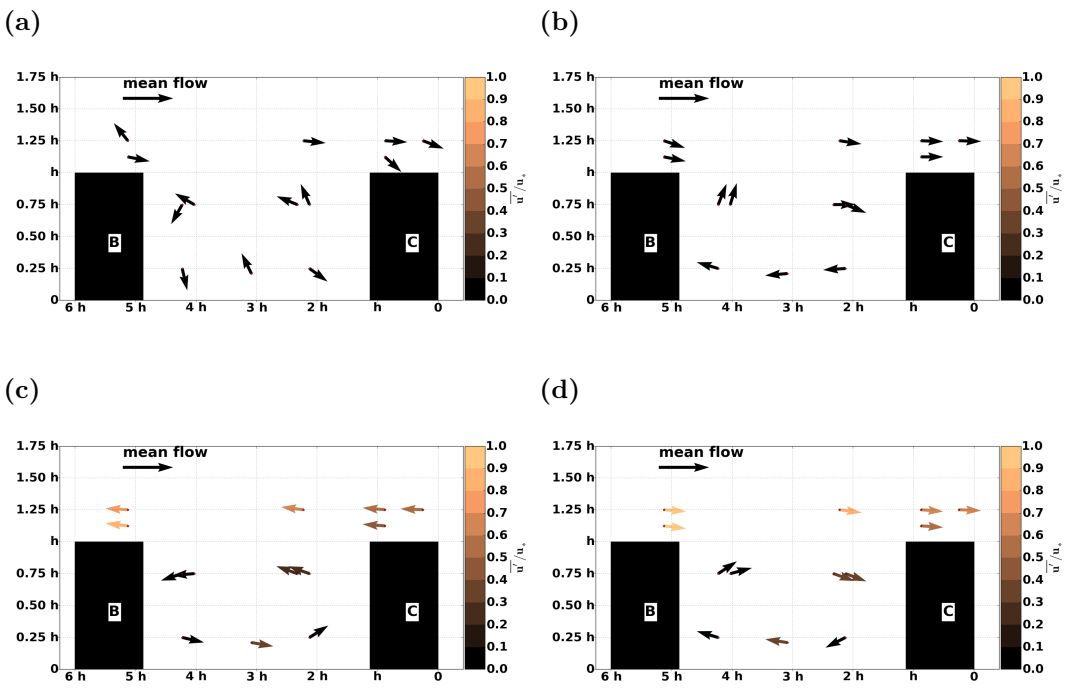

Figure 4.12: *North flow cases cross sections of mean perturbation flow for all cases (a), all ramp detected cases (b), all ramp detected cases restricted to Q2 (c), and Q4 (d) cases.*

The average fractional fluxes and TEs for northerly cases using the Wavelet Analysis and Modified Wavelet Analysis (Q2, ejection) methods are shown in Fig. 4.13. Figs. 4.13a and 4.13c show the average fractional fluxes (top number) and TEs (bottom number) for Wavelet Analysis detected periods for $\overline{u'w'}$ and $\overline{w'T'}$, respectively. Figs. 4.13b and 4.13d show the same, except using periods detected by the Modified Wavelet Analysis (Q2, ejection) method.

The results from the wavelet analysis method are similar to finding from the quadrant analysis method. All cases have lower fractional flux values when using the Modified Wavelet Analysis (Q2, ejection) method, again consistent with the results from the DNS analysis (Table 3.8). For $\overline{u'w'}$, the TEs values decrease, which is not consistent with the DNS analysis results. In contrast, four of the sonic anemometers exhibit an increase in TEs for when using the modified method $\overline{w'T'}$. These four sonics also showed an increase in TEs for northerly cases using the quadrant analysis method, which indicates consistency in the ability of the two techniques to separate CS-UCL interaction periods from non-interaction periods.

Profiles of $\overline{w'}$ are examined and compared with the characteristic markers from Chapter 2.4.2 (again, these characteristic markers were developed by only considering the presence/ non-presence of an LMR in the DNS dataset).

For northerly cases, Tower D will be assessed against the markers found for one block downstream of a roughness element from the DNS analysis (Table 2.3), while Tower E will be assessed against the markers found for one block upstream of a roughness element (Table 2.4). Towers B and C will be assessed against the

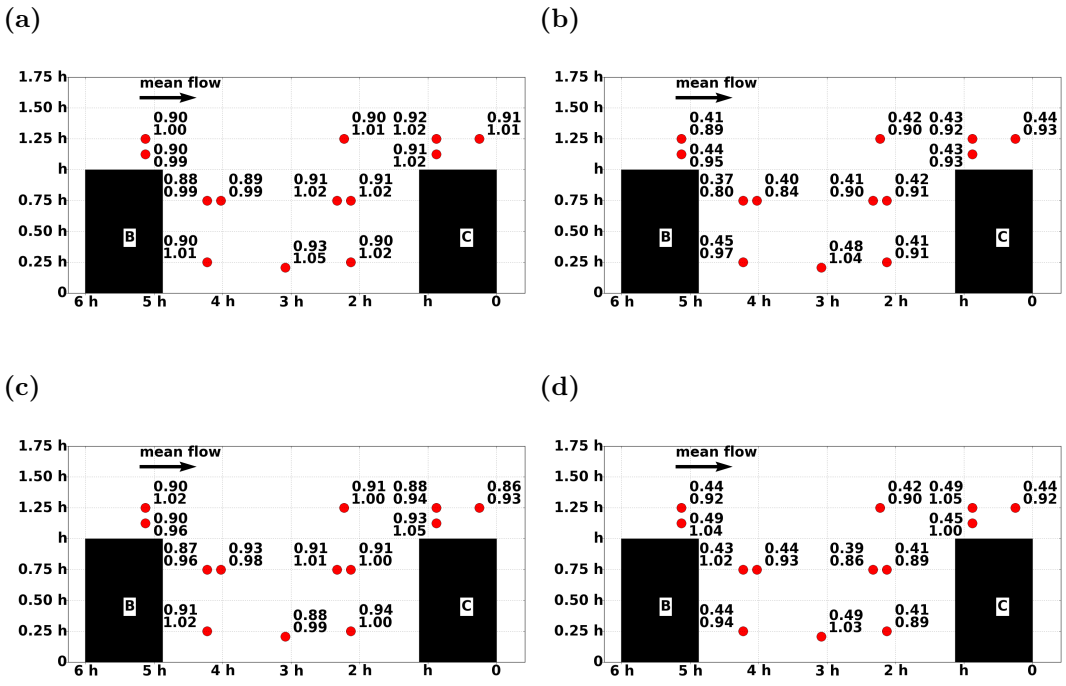

Figure 4.13: *North case cross sections of fractional fluxes (top number) and TEs (bottom number) for all wavelet detected events (a, c) and all wavelet detected events restricted to Q2 events (b, d) for* $\overline{u'w'}$ *(top row) and* $\overline{w'T'}$ *(bottom row).*

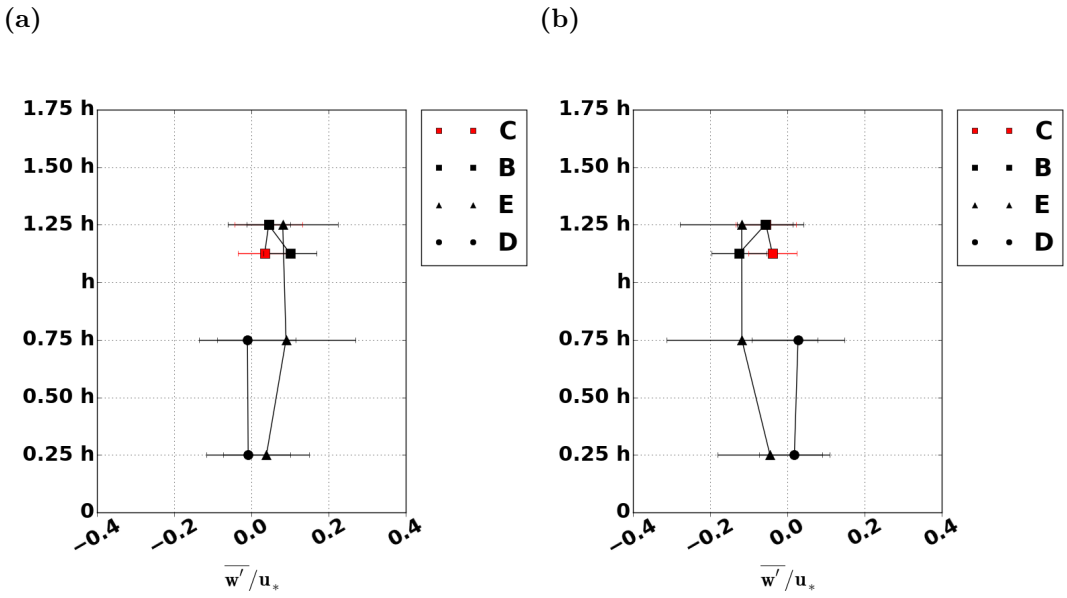

Figure 4.14: *North case $\overline{w'}$ profiles for wavelet analysis detected cases restricted to Q2, ejection (a) and Q4, sweep (b) events.*

markers found for the block directly over a roughness element (Table 2.6). As with previous analysis of the profiles of $\overline{w'}$, Tower F will not be discussed.

The profiles of $\overline{w'}$ show a clear difference when comparing the modified wavelet methods; the modified wavelet method (Q2, ejection) (Fig 4.14a) clearly exhibits the characteristics of CS-UCL interaction periods, whereas the modified wavelet method (Q4, sweep) clearly exhibits the characteristics of non CU-UCL interaction periods.

Finally, as was the case with the northerly flow analysis of turbulence quantities along the in-canyon rotor using the modified quadrant-hole method, the rotor following analysis using the modified wavelet analysis method also shows horizontal wind speeds above the canyon are reduced (indicative of the LMR), the values of u_* are overall smaller and average vertical velocities are less negative

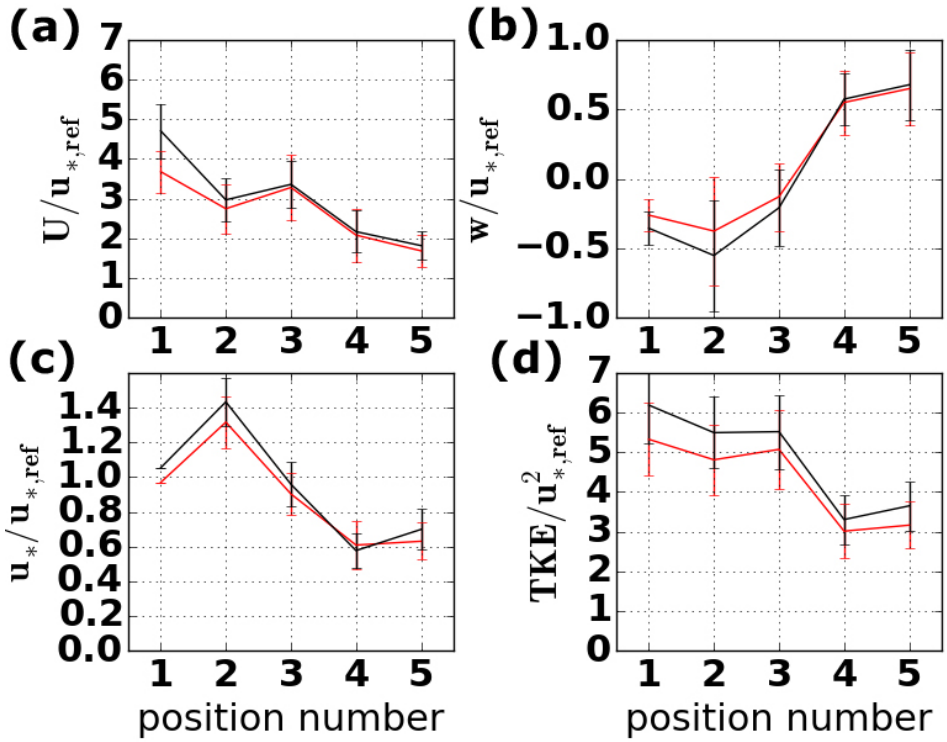

Figure 4.15: *Analysis of normalized mean horizontal wind speed (a), vertical component of velocity (b), friction velocity (c), and turbulence kinetic energy (d), along the path of the street canyon rotor for northerly flow during CS-UCL interaction periods as detected by the Modified Wavelet Analysis (Q2, ejection - Black) method and the Modified Wavelet Analysis (Q4, sweep - Red). Error bars indicate the spread of the data, using the value of one standard deviation.*

near the downstream side of the canyon (Fig. 4.15), when compared to non-interaction periods (Fig. 4.15). Again, reduced normalized TKE values at the rooftop level, as seen during CS-UCL interaction periods, tends to result in lower normalized TKE values inside the canyon, which indicates TKE is transported into the canyon by the mean flow.

4.6 South cases

The quadrant analysis method and the wavelet analysis method (including the modified methods), as described in Chapter 3, are now applied to south flow cases in a similar manner as was done for northerly cases (4.5). Each method is applied to the northern most 15 m AGL (3.0 m above roof level) sonic on building C; Based on the results from the DNS analysis (summarized in 3.1.3), a quadrant hole size of 0.25 and a coherent structure threshold of 0.2 are used used. As with the north cases described in the previous section, conditional cross sections, analysis of fractional flux and TE values, and characteristic profiles for north cases are presented in the following sections. However, given the relative "openness" of the upstream conditions for southerly cases, a consideration of the 3D effects of environmental vorticity must be given.

4.6.1 Consideration of 3D effects

In Chapter 1.2.2, the three dimensional nature of the flow around a building structure was briefly discussed. Of the features highlighted in Fig. 1.7, upstream cross-stream vorticity created by the environmental flow is shown to interact with the building, where the upstream environmental vortex lines are bent around the building creating a horseshoe vortex. It was then discussed that the horseshoe vortex could interact with the street canyon flow, potentially creating helical motion in the street canyon. For southerly flows at the cross center, this is potentially a concern, as the area south of the cross center is relatively free of obstructions, and a log-layer could form in the approach flow.

To estimate the impact of the environmental vorticity, the magnitude of estimates of cross-stream vorticity in the shear layer above Cross Center building C will be compared to an estimate of the magnitude of the cross-stream shear found in the upstream flow.

In general, vorticity is defined as

$$\vec{\omega} = \nabla \times \vec{v}, \tag{4.5}$$

which, when expanded into components, is

$$\vec{\omega} = \left(\frac{\partial w}{\partial y} - \frac{\partial v}{\partial z}\right)\hat{i} + \left(\frac{\partial u}{\partial z} - \frac{\partial w}{\partial x}\right)\hat{j} + \left(\frac{\partial v}{\partial x} - \frac{\partial u}{\partial y}\right)\hat{k}. \tag{4.6}$$

The component of vorticity of interest in this instance is the cross-stream component,

$$\vec{\omega}_y = \vec{\omega} \cdot \hat{j} = \frac{\partial u}{\partial z} - \frac{\partial w}{\partial x}, \tag{4.7}$$

which will now be estimated at the roof level of Cross Center C and the upstream flow.

4.6.1.1 Estimate of cross-stream vorticity in the shear layer

Using Eq. 4.7, the cross-stream vorticity of the shear layer can be estimated using the three sonic anemometers on Cross Center C. Based on Fig. 4.6b, the

Table 4.1: Estimates of u, w, ∂x, and ∂z based on Fig. 4.6b and a u_* value of order 1 ms^{-1}. The location of the sonic anemometers can be found in Fig. 4.4.

Velocity Component	Cs_15m (m/s)	Cn_15m	Cn_13.5m
u	6	5	3
w	1	-0.5	-0.5

values for u and w can be estimated as shown in Table 4.1. Values for ∂x and ∂z are 8 m and 1.5 m, respectively. Using these values in Eq. 4.7, the magnitude of cross-stream vorticity in the canopy shear layer above Cross Building C can be estimated as 1.5 s^{-1}.

4.6.1.2 Estimate of upstream environmental cross-stream vorticity

Without direct measurement of the flow to the south of the Cross Center observation site (i.e. upstream for southerly cases), some assumptions are made. First, it is assumed that the horizontal velocity measured using sonic anemometer Cs_15m (see Fig. 4.4) is a good estimate of the horizontal velocity upstream of the observation site. Second, it is assumed that the wind profile upstream of the observation site can be described with a log profile,

$$\frac{\partial u}{\partial z} = \frac{u_*}{kz}, \tag{4.8}$$

where u is the velocity and only a function of height, z is the height above ground, and k is the von Karman constant, assumed to have a value of 0.4. Third, it is

assumed that a constant flux layer exists in the log profile upstream (i.e. u_* is constant upstream). Using these assumptions, Eq. 4.8 can be solved for u such that

$$u(z) = \frac{u_*}{k} \ln\left(\frac{z}{z_0}\right), \tag{4.9}$$

where z_0 is defined to be the roughness length, or the height at which u is equal to zero (estimated to be $z_0 \approx 0.5$ upstream of the Cross Center). Eq. 4.9 and the values from Table 4.1 (again, assuming Cs_15m provides a good estimate of the horizontal velocity upstream of the observation site) are used to estimate of u_*, which is 0.7 m/s. Now that a value of u_* has been found, an estimate of the environmental cross-stream vorticity at half the building height can be made using Eq. 4.8, which results in a estimate of of 0.3 s^{-1}.

Given that the environmental vorticity is estimated to be an order of magnitude less that the vorticity found in the shear layer (which propagates downward into the street canyon), it will be assumed that the effects of the shear layer on turbulence transport are the dominant.

4.6.2 Quadrant and wavelet analysis of full-scale data - south cases

Given the extreme similarity of the results produced by the quadrant and wavelet analysis based method for northerly cases (section 4.5 of this chapter), both techniques will be presented side-by-side for southerly cases.

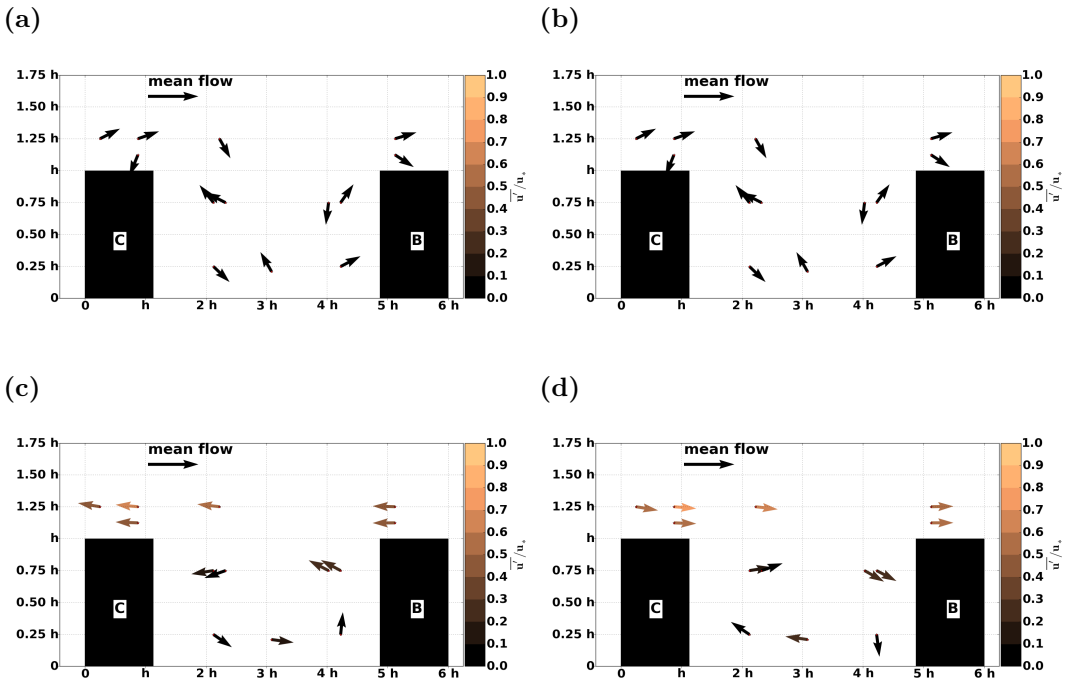

Figure 4.16: *South flow cases cross sections of mean perturbation flow for all cases (a), Quadrant Analysis detected cases (b), Quadrant Analysis detected cases restricted to Q2 events (c), and Quadrant Analysis detected cases restricted to Q4 events (d).*

Fig. 4.16 shows a comparison of conditionally averaged perturbation vectors (u', w') for four conditions (south cases): all north cases (Fig 4.16a), Quadrant Analysis detected cases (4.16b), Modified Quadrant Analysis (Q2, ejection) detected cases (4.16c), and Modified Quadrant Analysis (Q4, sweep) detected cases (4.16d). The exact same analysis is shown in Fig. 4.17, but using the wavelet analysis based detection method.

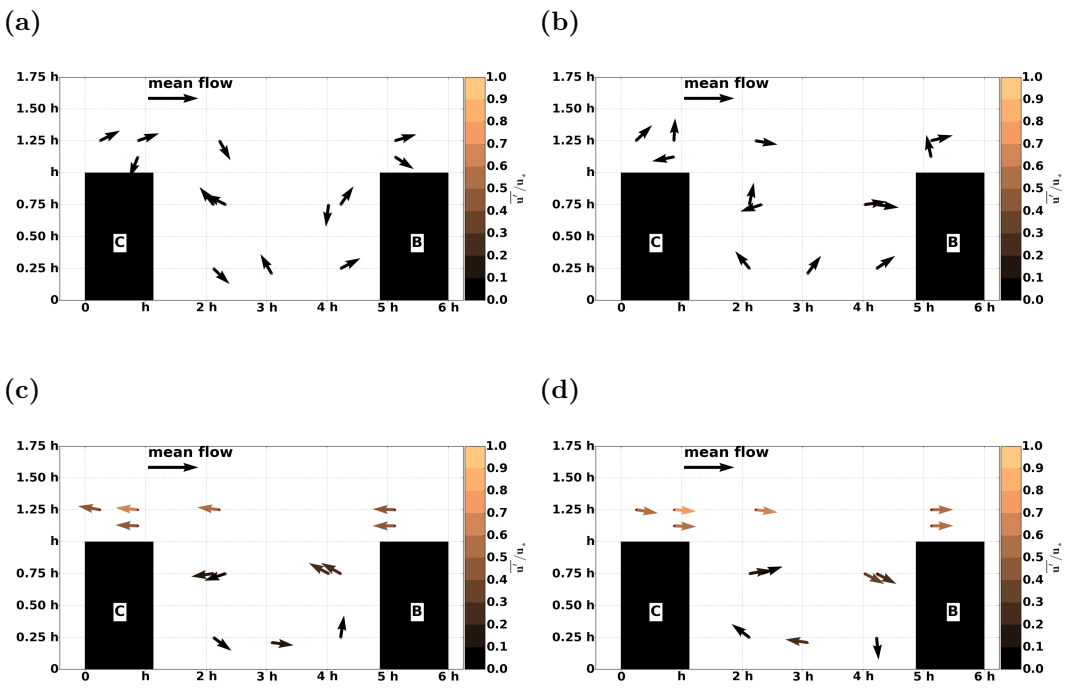

Figure 4.17: *South flow cases cross sections of mean perturbation flow for all cases (a), all ramp detected cases (b), all ramp detected cases restricted to Q2 (c), and Q4 (d) cases.*

As was the case for northerly flow, the conditional cross sections for all south cases (Fig 4.16a), Quadrant Analysis detected cases (4.16b), and Wavelet Analysis detected cases (4.17b) do not present clear flow patterns, and look nothing like the LMR-driven CS-UCL interaction periods or non-interaction periods from Chapter 2. However, the modified (Q2, ejection) detection techniques (quadrant-hole, Fig. 4.16c, wavelet analysis, Fig.4.17b), and modified (Q4, sweep) detection techniques (quadrant-hole, 4.16d, wavelet analysis,4.17d) clearly match the CS-UCL interaction (Fig. 2.9) and non-interaction (Fig. 2.8) periods, respectively. This has been the case for both flow directions and both techniques.

This would indicate that the modified wavelet method, in addition to the modified quadrant method, is able to capture motions consistent with what is expected by the LMR-driven interactions / non-interactions, independent of north/south upstream conditions.

Figs. 4.18a and 4.18c show the average fractional fluxes (top number) and TEs (bottom number) for Quadrant Analysis and Wavelet analysis detected periods, respectively, for $\overline{u'w'}$ and $\overline{w'T'}$. In all cases, the fractional flux values are reduced when using the modified (Q2, ejection) methods; this is consistent with the results from the DNS analysis (Tables 3.4 and 3.8). For $\overline{u'w'}$, the TEs values decrease, which is not consistent with the DNS analysis results. In contrast, nine of the sonic anemometers exhibit an increase in TEs for when using the modified method $\overline{w'T'}$. This is an increase from the five sonics that had an increase in TE for north cases. Given the expected stability difference between north and south flows, the

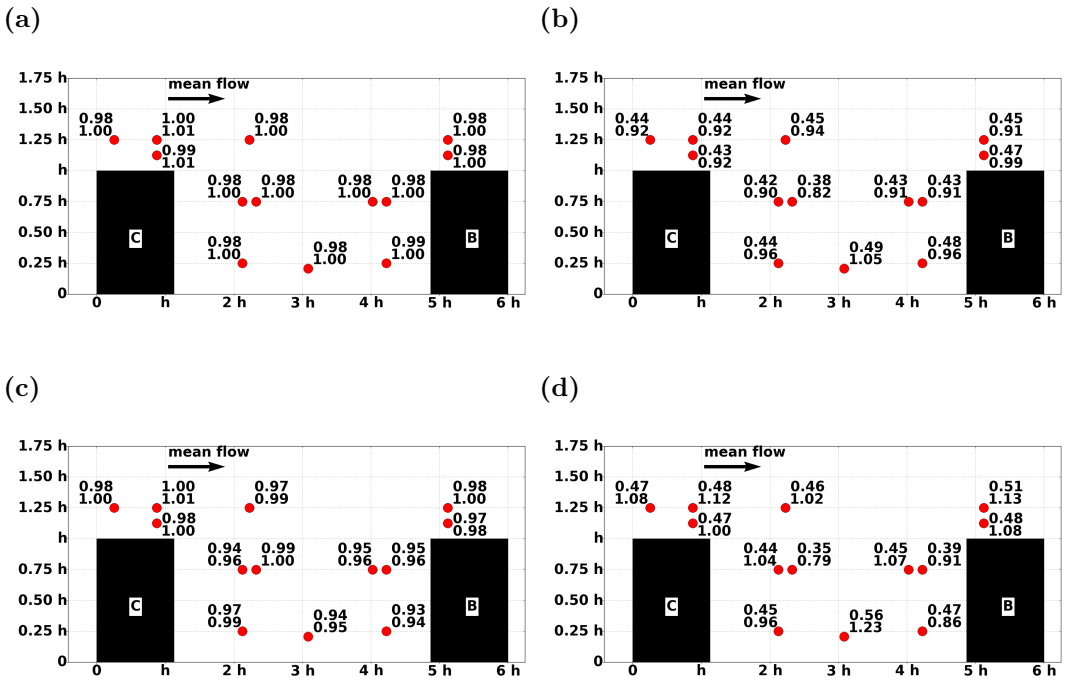

Figure 4.18: *South case cross sections of fractional fluxes (top number) and TEs (bottom number) for all quadrant detected events (a, c) and all quadrant detected events restricted to Q2 events (b, d) for* $\overline{w'w'}$ *(top row) and* $\overline{w'T'}$ *(bottom row).*

idea that these differences can be attributed to the lack of stability effects in the DNS dataset seems more plausible.

Profiles of $\overline{w'}$ are examined and compared with the characteristic markers from Chapter 2.4.2. Again, it is critical to note that these characteristic markers were developed by only considering the presence/ non-presence of an LMR in the DNS dataset.

For southerly cases, Tower E is assessed against the markers found for one block downstream of a roughness element from the DNS analysis (Table 2.3), while Tower D is assessed against the markers found for one block upstream

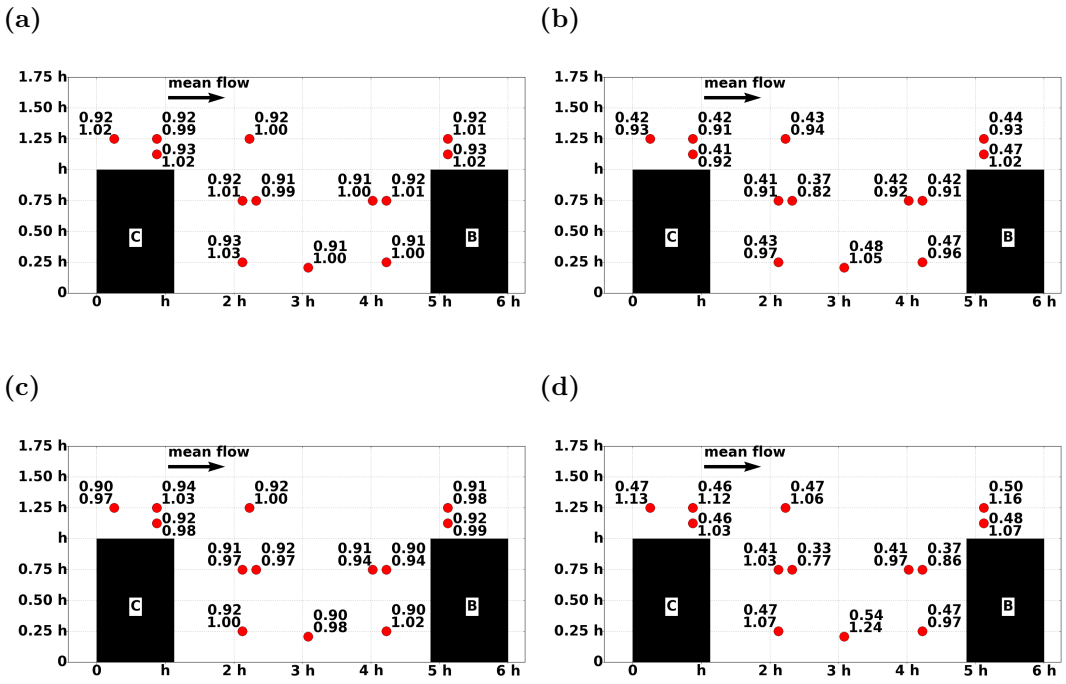

Figure 4.19: *South case cross sections of fractional fluxes (top number) and Ts (bottom number) for all wavelet detected events (a, c) and all quadrant detected events restricted to Q2 events (b, d) for* $\overline{u'w'}$ *(top row) and* $\overline{w'T'}$ *(bottom row).*

of a roughness element (Table 2.4). Towers B and C are assessed against the markers found for the block directly over a roughness element (Table 2.6). As with northerly cases, Tower F is not be discussed.

The profiles of $\overline{w'}$ show a clear difference when comparing the Modified Quadrant methods; the modified quadrant method (Q2, ejection) (Fig 4.20a) clearly exhibits the characteristics of CS-UCL interaction periods, whereas the modified quadrant-hole method (Q4, sweep) clearly exhibits the characteristics of non CU-UCL interaction periods. The same can be said of the profiles obtained using the wavelet analysis technique (Figs. 4.20c and 4.20d).

The along rotor flow analysis for southerly cases (not shown) produces the same qualitative results as the analysis for northerly flow (Figs. 4.11, 4.11, 4.15, 4.15).

While some differences are seen in the TEs when compared to the DNS analysis (which may be attributed to stability effects), all other comparisons between the full-scale analysis clearly show the flow patterns and characteristic markers found for LMR-driven CS-UCL interaction and non-interaction periods for the modified quadrant-hole and wavelet analysis based methods.

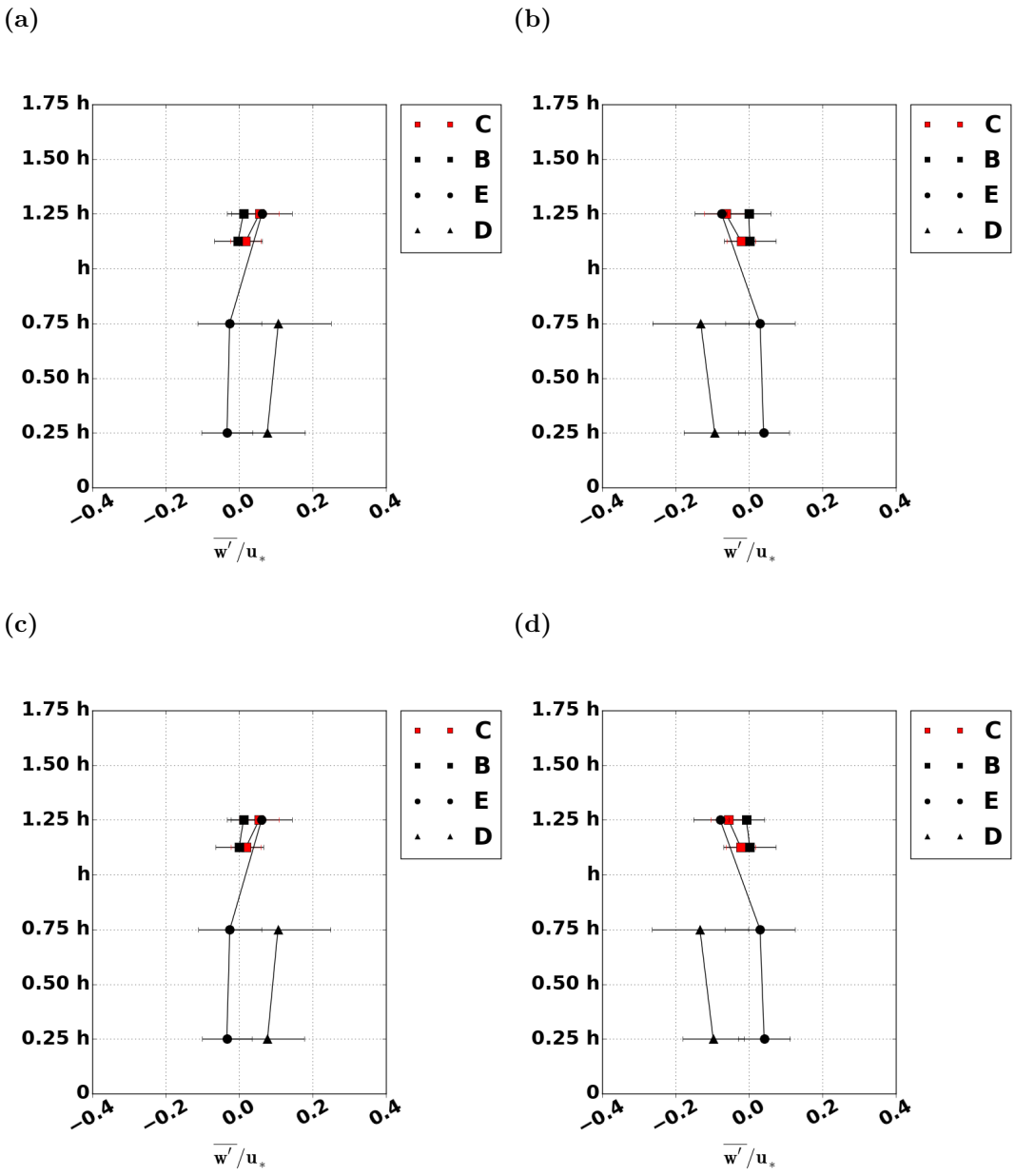

Figure 4.20: *South case $\overline{w'}$ profiles for quadrant analysis detected cases restricted to Q2, ejection (a) and Q4, sweep (b) events, and wavelet analysis cases restricted to Q2, ejection (c) and Q4, sweep (d) events*

4.7 Summary of CS-CSL interactions at full-scale

This chapter is guided based on the results of Chapter 2 and Chapter 3 which lay the groundwork for the ability to study LMR-driven CS-UCL interactions at full-scale, and the resulting techniques (including modified versions) from Chapter 3 are applied to observational data. An analysis of conditional cross sections to identify flow patterns, fractional fluxes and TE values, and profiles of turbulence quantities indicates that LMR-driven CS-UCL interactions occur in atmospheric boundary layer flows, and are detectable when modifications are made to the two most common analysis tools used in observational studies: the quadrant-hole and wavelet analysis techniques.

Both the quadrant analysis and wavelet analysis techniques paint similar pictures of the conditional flow patterns for north and south cases for both CS-UCL interaction periods, and non CS-UCL interaction periods, as driven by LMR. This suggests that both techniques are picking up on the same flow features and thus identifying the same phenomenon. The profiles of w' are in extremely good agreement with what was found in the DNS data in terms of LMR-driven CS-UCL interactions / non-interactions.

The major discrepancy between the DNS analysis and the full-scale analysis is in the examination of TE values. According to the DNS analysis, the TE values were expected to increase for CS-UCL interaction periods. The full-scale results showed a decrease in TE values for $u'w'$ for both north and south cases (both

analysis methods), although there was an increase in TE observed by several sonics for $w'T'$. This could be attributed to slight stability effects in the observational dataset that are not present in the DNS output, and could also point to a difference in the turbulence transport of heat and momentum.

Chapter 5

Summary and discussion: CS and UCL interactions

The goal of this work was to gain further insight into CS-UCL interactions. Chapter 1 presented a growing body of evidence that suggests larger scale coherent structures, particularly low speed streaks or low momentum regions, are associated with periods of strong turbulence transport across the UCL. As identified in the literature review, strong evidence for these interactions has been lacking in full-scale observational studies. One suggestion is that this is perhaps a reflection of the fact that traditional methods of analysis found in the engineering literature for simplified flows (like PCA or POD) are not readily applicable to full-scale studies. Further, the techniques used to study strong ventilation events, often attributed to CS-UCL interactions, are based on techniques developed in vegetation canopy studies and may not, on their own, be directly transferable to UCL studies.

A framework for the analysis of CS-UCL interaction had to be constructed using DNS output, in which the full temporal and spatial information regarding the flow is available. A new classification scheme, based on a new parameter LMR_i, was developed which can identify three types of periods of interaction:

CS-UCL interaction, transitional, and non-interaction periods (for a summary, see Table A.2).

Based on the new CS-UCL interaction classification scheme, depictions of flow behavior and properties (TKE, $\overline{u'w'}$, and $\overline{w'}$) were analyzed for each of the three interaction period types using conditional analysis. These conditional views improve upon the conceptual model of Coceal et al. (2007a) by including the flow inside the canyon, as well as directly analyzing the interactions between the canyon and canopy layer flows.

It is clear from the conditional views presented in Figs. 2.8, 2.9, and 2.10, that TKE, $\overline{u'w'}$ and $\overline{w'}$ change drastically both inside and outside of the canyon, between periods with and without CS-UCL interactions associated with LMRs. In fact, these quantities change so drastically that they resulted in characteristic markers in the vertical profiles of those quantities (Figs. 2.4.2.1, 2.4.2.2, and 2.4.2.3). A summary of these characteristic markers is found in Tables 2.2, 2.3, 2.4, 2.5. and 2.6. The consistency of these differences with previous studies and hypotheses from the literature indicate that LMR_i, and the statistical properties thereof, are capable of classifying CS-UCL interactions and non-interaction periods. The DNS analysis portion of study also demonstrates that it is only when LMRs are present that large upward motions occur between roughness elements (i.e. cubes), as previously only suggested by Takimoto et al. (2011). Not only that, the analysis presented in Chapter 2 suggests that the presence of the characteristic markers in the vertical profiles of the turbulence quantities should be expected in full-scale studies during LMR-driven CS-UCL interactions.

The results in chapter 2 clarify the conceptual models of both McNaughton (2004) (TEA-L structures, Fig. 1.4) and Coceal et al. (2007a) (Fig. 1.5). Specifically, this study found that the role of sweep motions generated by vortical motions in the conceptual TEA-L model, or near the edge of LMRs as the case with the conceptual model of Coceal et al. (2007a), do not play a role in the transport of momentum into the canyon. This is evident by the fact that sweep motions only appear in cases without CS-UCL interactions (Fig. 2.8), while ejections motions dominate the transitional periods (Fig. 2.10), which are most likely to capture events spatially located on the edge of LMRs. The shear layer thickening observed by Savory and Abdelqari (2000) was observed, but was directly linked to the structure of the LMR above the shear layer, and not the shear layer itself. While the results in Chapter 2 clarified the conceptual model of Coceal et al. (2007a) and provided insight as to how LMR-driven CS-UCL interactions would manifest in vertical profiles of various turbulence quantities, there was a lack in the ability to detect when CS-UCL interactions were occurring without using the spatially based parameter LMR_i; unfortunately, application of LMR_i at full scale was deemed impractical due to the need for spatially dense observations. In light of this lack of detection ability, Chapter 3 focused on the use of the quadrant-hole and wavelet analysis methods on the simulated time series datasets to assess their ability to detect CS-UCL interactions (particularly those driven by LMRs). This analysis revealed that these techniques, when unmodified, poorly capture the impact of LMR-driven CS-UCL interactions. As a result of this finding, it was shown that the full scale analysis techniques as currently used

in the literature seriously overestimate the impact of CS-UCL interactions. That said, there is a remarkable improvement in both methods' ability to capture these impacts when the conceptual model of Coceal et al. (2007a) is taken into account and a restriction is placed on the methods such that only time periods where ejections are dominant are used. The overestimation of the unmodified techniques was shown to be attributed to the detection of both ejection and sweep events (Q2 and Q4), when clearly only the Q2 events were related to the CS-UCL interactions. The modified quadrant-hole method with a small hole size (0.25) and the modified wavelet analysis method with a small CST (0.2) appear to be the best at capturing the impact of LMR-driven CS-UCL interaction periods, and it is suggested that these values be used in practice.

Both modified methods perform decently directly over the roughness elements, although they perform best over the $h \times h$ block directly upstream of a roughness element, and over the $h \times h$ block directly in-between roughness elements. Both modified methods perform poorly one $h \times h$ block downstream of a roughness element, likely due to direct wake effects, and similar locations in full-scale studies should be avoided.

When applied to full scale data at the Cross Center site, both the quadrant analysis and wavelet analysis techniques paint similar pictures of the conditional flow patterns, for north and south flows, for both LMR-driven CS-UCL interaction periods and non CS-UCL interaction periods. This indicates that both techniques are picking up on the same flow features and thus identifying the same phenomenon. This also confirms the suggestion by Roth (2000) that the

techniques used in studies over vegetative canopies are applicable in urban studies, although it is important to note the slight modifications used in this study. There now exists an open question as to whether these modified techniques are applicable in vegetative canopy studies. It is recommended that the existing datasets from the Canopy Horizontal Array Turbulence Study (CHATS) field experiment (Patton et al. 2011) be explored to address this question, given the fine spatial and temporal resolution available via the sonic anemometer datasets.

The profiles of w' are in extremely good agreement with what was found in the DNS data in terms of LMR-driven CS-UCL interactions / non-interactions. For the case of southerly flows, an estimation of background environmental cross-stream vorticity was shown to be an order of magnitude less than the cross-stream vorticity associated with the shear layer. While only an estimation, this suggests that vertical transport associated with vorticity associated with the shear layer dominates the transport related to 3D effects of upstream vorticity wrapping around the building.

One limitation of this study is that roughness elements in the DNS as well as the buildings at the Cross Center had (relativly) flat top surfaces. Kastner-Klein and Plate (1999) show details such as roof shape affect in canyon flow and can even suppress formation of street-canyon vorticies all together. The results from this work, such as the perturbation flow signatures, should be tested under non-flat roof situations, especially where the street-canyon vorticies are suppressed.

The major discrepancy between the DNS analysis and the full-scale analysis is in the examination of TE values. According to the DNS analysis, the TE

values were expected to increase for CS-UCL interaction periods. The full-scale results showed a decrease in TE values for the kinematic along-stream momentum flux for both north and south cases (both analysis methods), although there was an increase in TE observed by several sonics for $w'T'$. This shows that coherent structures in full-scale atmospheric surface layer flows are not as efficient as previously thought when it comes to momentum transport. This could be attributed to slight stability effects in the observational dataset that are not present in the DNS output. The full scale results also indicate that heat and momentum are transported differently by CS-UCL interactions.

Finally, while (Christen et al. 2007) speculated on the role of larger scale CS above urban street canyons in turbulence transport, this study has shown for the first time that there is a direct link between CS, specifically LMRs, and the turbulence transport across the UCL.

References

Addison, P. S., 2002: *The Illustrated Wavelet Transform Handbook*. Taylor & Francis.

Adrian, R. J., K. T. Christensen, and Z.-C. Liu, 2000a: Analysis and interpertation of instantaneous turbulent velocity fields. *Experiments in Fluids*, **29**, 275–290.

Adrian, R. J., C. D. Meinhart, and C. D. Tomkins, 2000b: Vortex orginazation in the outer region of the turbulent boundary layer. *Journal of Fluid Mechanics*, **422**, 1–54.

Allee, W. C., 1926: Measurements of envrionmental factors in the tropical rainforest of Panama. *Ecology*, **7**, 273–302.

Allwine, J. K., J. H. Shinn, G. E. Streit, K. L. Clawson, and M. Brown, 2002: Overview of URBAN 2000. *Bulletin of the American Meteorological Society*, **83**, 521–536.

Allwine, K. J., M. J. Leach, L. W. Stockham, J. S. Shinn, R. P. Hosker, J. F. Bowers, and J. C. Pace, 2004: Overview of Joint Urban 2003 - an atmospheric dispersion study in oklahoma city. *Preprints, Symposium on Planning, Nowcasting, and Forecasting in the Urban Zone*, Seattle, Washington, J7.1.

Arya, S. P., 2001: *Introduction to micrometeorology*. 2d ed., Academic Press, 420 pp.

Bake, S., G. W. Meyer, and U. Rist, 2002: Turbulence mechanism in Klebanoff transition: A quantatitive comparison of experiment and direct numerical simulation. *Journal of Fluid Mechanics*, **459**, 217–243.

Barlow, J. F. and S. E. Belcher, 2004: A wind tunnel model for quantifying fluxes in the urban boundary layer. *Boundary-Layer Meteorology*, **104**, 131–150.

Barlow, J. F., I. N. Harman, and S. E. Belcher, 2004: Scalar fluxes from urban street canyons. part i: laboratory simulation. *Boundary-Layer Meteorology*, **113**, 369–385.

Barthlott, C., P. Drobinski, C. Fesquet, T. Bubos, and C. Pietras, 2007: Long-term study of coherent structures in the atmospheric surface layer. *Boundary-Layer Meteorology*, **125**, 1–24.

Castro, I. P., H. Cheng, and R. Reynolds, 2006: Turbulence over urban-type roughness: deduction from wind tunnel measurments. *Boundary-Layer Meteorology*, **118**, 109–131.

Christen, A., E. von Gorsel, and R. Vogt, 2007: Coherent structures in urban roughness sublayer turbulence. *International Journal of Climatology*, **27**, 1955–1968.

Christensen, K. T. and R. J. Adrian, 2001: Statistical evidence of hairpin vortex packets in wall turbulence. *Journal of Fluid Mechanics*, **431**, 433–443.

Coceal, O., A. Dobre, and T. G. Thomas, 2007a: Unsteady dynamics and organized structures from DNS over an idealized building canopy. *International Journal of Climatology*, **27**, 1943–1953.

Coceal, O., A. Dobre, T. G. Thomas, and S. E. Belcher, 2007b: Structure of turbulent flows over regular arrays of cubical roughness. *Journal of Fluid Mechanics*, **589**, 375–409.

Coceal, O., T. G. Thomas, and S. E. Belcher, 2007c: Spatial variability of flow statistics within regular building arrays. *Boundary-Layer Meteorology*, **125**, 537–552.

Coceal, O., T. G. Thomas, I. P. Castro, and S. Belcher, 2006: Mean flow and turbulence statistics over groups of urban-like cubical obstacles. *Boundary-Layer Meteogology*, **121**, 491–519.

Collineau, S. and Y. Brunet, 1993: Detection of turbulent coherent motions in a forest canopy. part I: Wavelet analysis. *Boundary-Layer Meteorology*, **65**, 357–379.

Doran, J. C., J. D. Fast, and J. Horel, 2002: The VTMX 2000 campaign. *Bulletin of the American Meteorological Society Meteorology*, **83**, 537–551.

Eliasson, I., B. Offierle, C. S. B. Grimmond, and S. Lindqvist, 2006: Wind fields and turbulence statistics in an urban street canyon. *Atmospheric Environment*, **40**, 1–16.

Farge, M., 1992: Wavelet transforms and their applications to turbulence. *Annual Review of Fluid Mechanics*, **24**, 395–458.

Feigenwinter, C. and R. Vogt, 2005: Detection and analysis of coherent structures in urban turbulence. *Theoretical and applied climatology*, **81**, 219–230.

Finnigan, J. J., 1979: Turbulence in waving wheat. II: Structure of momentum transfer. *Boundary-Layer Meteorology*, **16**, 213–236.

Finnigan, J. J., 2000: Turbulence in plant canopies. *Annual Review of Fluid Mechanics*, **32**, 519–571.

Gao, W., R. Shaw, and K. Paw U, 1989: Observation of organized structure in turbulent flow within and above a forest canopy. *Boundary-Layer Meteorology*, **47**, 349–377.

Glickman, T. and A. M. Society, 2000: *Glossary of meteorology*. American Meteorological Society.

Head, M. R. and P. Bandyopadhyay, 1981: New aspects of turbulent boundary-layer structure. *Journal of Fluid Mechanics*, **107**, 297–338.

Idczak, M., P. Mestayer, J.-M. Rosant, J.-F. Sini, and M. Violleau, 2007: Micrometeorological measurements in a stree canyon during the joint ATREUS-PICADA experiment. *Boundary-Layer Meteorology*, **124**, 25–41.

Jeong, J. and F. Hussain, 1995: On the identification of a vortex. *Journal of Fluid Mechanics*, **285**, 69–94.

Johnson, G. T. and L. J. Hunter, 1999: Some insights into typical urban canyon airflows. *Atmospheric Environment*, **33**, 3991–3999.

Kanda, M., T. Kawai, K. Narita, A. Hagishima, and R. Moriwaki, 2006: A comprehensive outdoor scale model experiment for urban climate. *Proceedings of the International Conference on Urban Climate.*, Göteborg, Sweden, International Association for Urban Climate, 270–273.

Kastner-Klein, P., R. Berkowicz, and R. Britter, 2004: The influence of street architecture on flow and dispersion in street canyons. *Meteorology and Atmospheric Physics*, **87**, 121–131.

Kastner-Klein, P. and E. J. Plate, 1999: Wind-tunnel study of concentration fileds in street canyons. *Atmospheric Environment*, **33**, 3979–3979.

Klein, P. and J. Galvez, 2014: Flow and turbulence characteristics in a suburban street canyon. *Environmental Fluid Mechanics*, 1–20.

Kundu, P. and I. Cohen, 2004: *Fluid Mechanics*. 3d ed., Elsevier Science, 759 pp.

Li, X.-X., Y. C. L. Dennis, and C.-H. Liu, 2008: Physical modeling of flow field inside urban street canyons. *Journal of Applied Meteorology and Climatology*, **47**, 2058–2067.

Louka, P., S. E. Belcher, and R. G. Harrison, 2000: Coupling between air flow in streets and the well-developed boundary layer aloft. *Atmospheric Environment*, **34**, 2613–2621.

Mahrt, L., 1991: Eddy asymmetry in the sheared heated boundary layer. *Journal of the Atmospheric Sciences*, **48**, 472–492.

Mahrt, L. and W. Gibson, 1992: Flux decomposition into coherent structures. *Boundary-Layer Meteorology*, **60**, 143–168.

Mason, R. A., H. N. Shirer, R. Wells, and G. S. Young, 2002: Vertical transport by plumes within the moderately convertive marine atmospheric surface layer. *Journal of the Atmospheric Sciences*, **59**, 1337–1355.

McNaughton, K. G., 2004: Turbulence structure of the unstable atmospheric surface layer and transition to the outter layer. *Boundary-Layer Meteorology*, **112**, 199–221.

McNaughton, K. G. and R. E. Blundell, 2002: A model for the large-scale ramp structures observed in the atmospheric surface layer. *Preprints: 15th Conference on Boundary Layers and Turbulence*, Wageningen, Netherlands, P9.10.

Mestayer, P. G., et al., 2005: The urban boundary layer field experiment over Marseille UBL/CLU-ESCOMPTE: Experimental set-up and first results. *Boundary-Layer Meteorology*, **114**, 315–365.

Natrajan, V. K., Y. Wu, and K. T. Christensen, 2007: Spatial signatures of retrograde spanwise vorticies in wall turbulence. *Journal of Fluid Mechanics*, **574**, 155–167.

Nelson, M. A., E. R. Pardyjak, M. J. Brown, and J. C. Klewicki, 2007: Properties of the wind field within the oklahoma city park avenue street canyon part II: Spectra, cospectra, and quadrant analysis. *Journal of Applied Meteorology and Climatology*, **46**, 2055–2073.

Newsom, R., R. Calhoun, D. Ligon, and J. Allwine, 2008: Linearly organized turbulence structures observed over a suburban area by dual-doppler LIDAR. *Boundary-layer Meteorology*, **127**, 111–130.

Oke, T. R., 1988: Street design and urban canopy layer climate. *Energy and Buildings*, **11**, 103–113.

Oke, T. R., 1989: The micrometeorology of the urban forest. *Philosophical Transactions of the Royal Society of London B*, **324**, 335–349.

Patton, E. G., et al., 2011: The canopy horizontal array turbulence study. *Bulletin of the American Meteorological Society*, **92**, 593–611.

Raupach, M. R., P. Coppin, and B. Legg, 1986: Experiments on scalar dispersion within a model plan canopy part 1: the turbulence structure. *Boundary-Layer Meteorology*, **35**, 167–191.

Rinker, D. K. and G. S. Young, 1996: Use of obliquely rotated principal component analysis to identify coherent structures. *Boundary-layer Meteorology*, **80**, 19–47.

Robinson, S. K., 1991: Coherent motions in the turbulent boundary layer. *Annual Review of Fluid Mechanics*, **23**, 601–639.

Rotach, M. W., et al., 2005: BUBBLE - an urban boundary layer meteorology project. *Theoretical Applied Climatology*, **81**, 231–261.

Roth, M., 2000: Review of atmospheric turbulence over cities. *Q.J.R. Meteorol. Soc.*, **126**, 941–990.

Rowntree, R. A., 1984: Ecology of the urban forest. *Urban Ecology*, **8**, 1–11.

Salmond, J. A., T. R. Oke, C. S. B. Grimmond, S. Roberts, and B. Offerle, 2005: Venting of heat and carbon dioxide from urban canyons at night. *Journal of Applied Meteorology*, **44**, 1180–1194.

Savory, E. and A. Abdelqari, 2000: The effect of large-scale turbulent structures on a simple 2-D canyon-type flow. *Environmental Monitoring and Assessment*, **65**, 397–405.

Shaw, R. H., J. Tavangar, and D. Ward, 1983: Structure of the reynolds stress in a canopy layer. *Journal of Climate and Applied Meteorology*, **22**, 1922–1931.

Sheng, J., E. Malkiel, and J. Katz, 2008: Using digital holographic microscopy for simultaneous measurements of 3D near wall shear stress in a turbulent boundary layer. *Experimental Fluids*, **45**, 1023–1035.

Shiotani, M. and G. Yamamoto, 1950: Atmospheric turbulence over the large city - turbulence in the free atmosphere (2^{nd} report). *Geophysics Magazine*, **21**, 134–147.

Smith, C. R., J. D. A. Walker, A. H. Haidari, and U. Sobrun, 1991: On the dynamics of near-wall turbulence. *Philosophical Transactions of the Royal Society of London A*, **336**, 131–175.

Stull, R. B., 1988: *An introduction to boundary layer meteorology*. Academic Publishers, 666 pp.

Subramanian, C. S., S. Rajagopalan, R. A. Antonia, and A. J. Chambers, 1982: Comparison of conditional sampling and averaging techniques in a turbulent boundary layer. *Journal of Fluid Mechanics*, **123**, 335–362.

Takimoto, H., A. Sato, J. F. Barlow, R. Moriwaki, A. Inagaki, S. Onomura, and M. Kanda, 2011: Particle image velocimetry measurements of turbulent flow within outdoor and indoor urban scale models and flushing motions in urban canopy layers. *Boundary-Layer Meteorology*, **140**, 295–314.

Theodorsen, T., 1952: Mechanism of turbulence. *Proceedings of the 2^{nd} Midwestern converence on fluid mechanics*, Columbus, Ohio, 1–19.

Thomas, C. and T. Foken, 2005: Detection of long-term coherent exchange over spruce forest using wavelet analysis. *Theoretical and Applied Climatology*, **80**, 91–104.

Thomas, C. and T. Foken, 2007a: Organised motion in a tall spruce canopy: Temporal scales, structure spacing and terrain effects. *Boundary-Layer Meteorology*, **122**, 123–147.

Thomas, C. and T. Foken, 2007b: Flux contribution of coherent structures and its implications for the exchange of energy and matter in a tall spruce canopy. *Boundary-Layer Meteorology*, **123**, 317–337.

Tomkins, C. D. and R. J. Adrian, 2003: Spanwise structure and scale groth in turbulent boundary layers. *Journal of Fluid Mechanics*, **490**, 37–74.

Torrence, C. and G. P. Compo, 1998: A practical guide to wavelet analysis. *Bulletin of the American Meteorological Society*, **79**, 61–78.

United Nations, D. o. E. and P. D. Social Affairs, 2011: World urbanization prospects, the 2011 revision.

Weijers, E. P., A. van Delden, H. F. Vugts, and G. C. A. Meesters, 1995: Characteristics of convective turbulence in the surface layer investigated by principal component analysis. *Journal of Applied Meteorology*, **34**, 528–541.

Wu, Y. and K. T. Christensen, 2006: Population trends of spanwise vortices in wall turbulence. *Journal of Fluid Mechanics*, **568**, 55–76.

Yao, Y. F., T. G. Thomas, N. D. Sandham, and J. J. R. Williams, 2001: Direct numerical simulation of turbulent flow over a rectangular trailing edge. *Theoretical and Computational Fluid Dynamics*, **14**, 337–358.

Zhou, J., R. J. Adrian, S. Balachandar, and T. M. Kendall, 1999: Mechanisms for generating coherent packets of hairpin vortices in channel flow. *Journal of Fluid Mechanics*, **387**, 353–396.

Appendix A: extended chapter 2 tables

A.1 DNS output description

Table A.1: Description of data output from DNS.

Terminology Used in Text	Data Type	Description
Block time series	Time series	Data from the center grid point from each $h \times h$ block (192 blocks), output at each model integration step, $\delta t = 1/400\tau$. These data are available at a vertical resolution of $\delta z = 1/4h$, starting at $z = 1/32h$
Slice data	Slice (spatial snapshot in time)	Data taken from a horizontal (XY) or vertical (XZ) slice through the DNS domain with the native grid resolution ($\Delta = 1/32h$). These data are available at a temporal resolution of $\delta t = 1/10\tau$. 974 snapshots exist for each type of slice (XY or XZ)
Slice time series data	Time series	Time series data at the native spatial grid resolution created using the slice data. These are created using slice data; they have a time resolution $40\times$ less that the block time series data.

A.2 LMR_i statistic sample sizes

Table A.2: Description of sample size for LMR_i statistics.

Window Size (Δt_w)	Samples used to compute statics (N_s)	Number of windows (N_w)	Number of each static type (N_{stats})
97.4 τ	974	1	192
10 τ	100	9	1728
τ	10	97	18,624
Δt_w	$N_s = \frac{10 * \Delta t_w}{\tau}$	$N_w = \lfloor \frac{97.4 * \tau}{\Delta t_w} \rfloor$	$N_{stats} = 192 * N_w$